

ACKNOWLEDGEMENT

This material is based upon work supported by the Department of Energy under Award Number DE-FE00006821.

DISCLAIMER

This report was prepared as an account of work sponsored by an agency of the United States Government. Neither the United States Government nor any agency thereof, nor any of their employees, makes any warranty, express or implied, or assumes any legal liability or responsibility for the accuracy, completeness, or usefulness of any information, apparatus, product, or process disclosed, or represents that its use would not infringe privately owned rights. Reference herein to any specific commercial product, process, or service by trade name, trademark, manufacturer, or otherwise does not necessarily constitute or imply its endorsement, recommendation, or favoring by the United States Government or any agency thereof. The views and opinions of authors expressed herein do not necessarily state or reflect those of the United States Government or any agency thereof.

**SMALL SCALE FIELD TEST DEMONSTRATING CO₂ SEQUESTRATION IN
ARBUCKLE SALINE AQUIFER AND BY CO₂-EOR AT WELLINGTON FIELD,
SUMNER COUNTY, KANSAS**

Project Director/Principal Investigator:

**W. Lynn Watney
Senior Scientific Fellow
Kansas Geological Survey
Ph: 785-864-2184, Fax: 785-864-5317
lwatney@kgs.ku.edu**

Joint Principal Investigator:

**Yevhen “Eugene” Holubnyak
eugene@kgs.ku.edu
Ph: 785-864-2070**

Final Report

By

**Prepared by Yevhen Holubnyak, Lynn Watney, Jennifer Hollenbach, Tiraz Birdie, Mina
Fazelalavi, Tandis Bidgoli, Drew Schwab, Alex Nolte, George Tsoflias, John Victorine,
Brandon Graham, John Doveton, Jason Bruns, Brett Blazer, Dana Wreath**

Date of Report: December 31, 2017

DUNS Number: 076248616

Recipient: University of Kansas Center for Research &

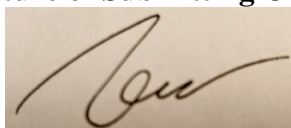
Kansas Geological Survey

1930 Constant Avenue

Lawrence, KS 66047

Project/Grant Period: 10/1/2011 through 9/30/2017

Signature of Submitting Official:

A handwritten signature in black ink on a light-colored background. The signature is stylized and appears to be 'Yevhen' or 'Eugene'.

Yevhen “Eugene” Holubnyak

Executive Summary

The objectives of this project are to understand the processes that occur when a maximum of 70,000 metric tonnes of CO₂ are injected into two different formations to evaluate the response in different lithofacies and depositional environments. The evaluation will be accomplished through the use of both in situ and indirect MVA (monitoring, verification, and accounting) technologies. The project will optimize for carbon storage accounting for 99% of the CO₂ using lab and field testing and comprehensive characterization and modeling techniques.

Site characterization and CO₂ injection should demonstrate state-of-the-art MVA tools and techniques to monitor and visualize the injected CO₂ plume and to refine geomodels developed using nearly continuous core, exhaustive wireline logs, and well tests and a multi-component 3-D seismic survey. Reservoir simulation studies will map the injected CO₂ plume and estimate tonnage of CO₂ stored in solution, as residual gas, and by mineralization and integrate MVA results and reservoir models shall be used to evaluate CO₂ leakage. A rapid-response mitigation plan was developed to minimize CO₂ leakage and provide a comprehensive risk management strategy. The CO₂ was intended to be supplied from a reliable facility and have an adequate delivery and quality of CO₂. However, several unforeseen circumstances complicated this plan: (1) the initially negotiated CO₂ supply facility went offline and contracts associated with CO₂ supply had to be renegotiated, (2) a UIC Class VI permit proved to be difficult to obtain due to the experimental nature of the project. Both subjects are detailed in separate deliverables attached to this report.

The CO₂ enhanced oil recovery (EOR) and geologic storage in Mississippian carbonate reservoir was successfully deployed. Approximately 20,000 metric tons of CO₂ was injected in the upper part of the Mississippian reservoir to verify CO₂ EOR viability in carbonate reservoirs and evaluate a potential of transitioning to geologic CO₂ storage through EOR. A total of 1,101 truckloads, 19,803 metric tons—an average of 120 tonnes per day—were delivered over the course of injection that lasted from January 9 to June 21, 2016. After cessation of CO₂ injection, the KGS 2-32 well was converted to water injector and continues to operate. CO₂ EOR progression in the field was monitored weekly with fluid level, temperature, and production recording and formation fluid composition sampling.

It is important to note that normally, CO₂ EOR pilots are less efficient than commercial operations due to lack of directional and precise well control, lack of surface facilities for CO₂ recycling, and other factors. As a result of this pilot CO₂ injection, the observed incremental average oil production increase was ~68% with only ~18% of injected CO₂ produced back. Decline curve analysis forecasts of additional cumulative oil produced were 32.44M STB to the end of 2027. Wellington Mississippian pilot efficiency by the end of forecast calculations is 11 MCF per barrel of produced oil. Using 32M STB oil production and \$1,964,063 cost of CO₂, CO₂ EOR cost per barrel of oil production is ~\$60.

Simple but robust monitoring technologies proved to be very efficient in detecting and locating CO₂. High CO₂ reservoir retentions with low yields within an actively producing field could help to estimate real-world risks of CO₂ geological storage for future projects. The Wellington Field CO₂ EOR was executed in a controlled environment with high efficiency. This case study proves

that CO₂ EOR could be successfully applied in Kansas carbonate reservoirs if CO₂ sources and associated infrastructure are available.

Recent developments in unconventional resources development in Mid-Continent USA and associated large volume disposal of backflow water and the resulting seismic activity have brought more focus and attention to the Arbuckle Group in southern Kansas. Despite the commercial interest, limited essential information about reservoir properties and structural elements has impeded the management and regulation of disposal, an issue brought to the forefront by recent seismicity in and near areas of large volumes and rates of brine disposal.

The Kansas Geological Survey (KGS) collected, compiled, and analyzed available data, including well logs, core data, step rate tests, drill stem tests, 2-D and 3-D seismic data, water level measurements, and others types of data. Several exploratory wells were drilled and core was collected and modern suites of logs were analyzed. Reservoir properties were populated into several site-specific geological models. The geological models illustrate the highly heterogeneous nature of the Arbuckle Group. Vertical and horizontal variability results in several distinct hydro-stratigraphic units that are the result of both depositional and diagenetic processes.

During the course of this project, it has been demonstrated that advanced seismic interpretation methods can be used successfully for characterization of the Mississippian reservoir and Arbuckle saline aquifer. Analysis of post-stack 3-D seismic data at the Mississippian reservoir showed the response of a gradational velocity transition. Pre-stack gather analysis showed that porosity zones of the Mississippian and Arbuckle reservoirs exhibit characteristic amplitude versus offset (AVO) response. Simultaneous AVO inversion estimated P- and S-impedances. The 3-D survey gather azimuthal anisotropy analysis (AVAZ) provided information about the fault and fracture network and showed good agreement to the regional stress field and well data. Mississippian reservoir porosity and fracture predictions agreed well with the observed mobility of injected CO₂ in KGS well 2-32. Fluid substitution modeling predicted acoustic impedance reduction in the Mississippian carbonate reservoir introduced by the presence of CO₂.

Seismicity in the United States midcontinent has increased by orders of magnitude over the past decade. Spatiotemporal correlations of seismicity to wastewater injection operations have suggested that injection-related pore fluid pressure increases are inducing the earthquakes. In this investigation, we examine earthquake occurrence in southern Kansas and northern Oklahoma and its relation to the change in pore pressure. The main source of data comes from the Wellington Array in the Wellington oil field, in Sumner County, Kansas, which has monitored for earthquakes in central Sumner County, Kansas, since early 2015. The seismometer array was established to monitor CO₂ injection operations at Wellington Field. Although no seismicity was detected in association with the spring 2016 Mississippian CO₂ injection, the array has recorded more than 2,500 earthquakes in the region and is providing valuable understanding to induced seismicity. A catalog of earthquakes was built from this data and was analyzed for spatial and temporal changes, stress information, and anisotropy information. The region of seismic concern has been shown to

be expanding through use of the Wellington earthquake catalog, which has revealed a northward progression of earthquake activity reaching the metropolitan area of Wichita. The stress orientation was also calculated from this earthquake catalog through focal mechanism inversion. The calculated stress orientation was confirmed through comparison to other stress measurements from well data and previous earthquake studies in the region. With this knowledge of the stress orientation, the anisotropy in the basement could be understood. This allowed for the anisotropy measurements to be correlated to pore pressure increases. The increase in pore pressure was monitored through time-lapse shear-wave anisotropy analysis. Since the onset of the observation period in 2010, the orientation of the fast shear wave has rotated 90°, indicating a change associated with critical pore pressure build up. The time delay between fast and slow shear wave arrivals has increased, indicating a corresponding increase in anisotropy induced by pore pressure rise. In-situ near-basement fluid pressure measurements corroborate the continuous pore pressure increase revealed by the shear-wave anisotropy analysis over the earthquake monitoring period.

This research is the first to identify a change in pore fluid pressure in the basement using seismological data and it was recently published in the AAAS journal *Science Advances* (Nolte et al., 2017). The shear-wave splitting analysis is a novel application of the technique, which can be used in other regions to identify an increase in pore pressure. This increasing pore fluid pressure has become more regionally extensive as earthquakes are occurring in southern Kansas, where they previously were absent. These monitoring techniques and analyses provide new insight into mitigating induced seismicity's impact on society.

List of Acronyms and Abbreviations

API gravity	American Petroleum Institute gravity (petroleum density measurement)
AVAZ	Azimuthal anisotropy analysis
AVO	Amplitude versus offset
BHP	Bottom hole pressure
BOE	Barrel of oil equivalent (unit of energy)
BOPD	Barrels of oil per day
C	Carbon
CCS	Carbon capture and storage
CCUS	Carbon capture utilization and storage
CMG	Computer Modeling Group
CO ₂	Carbon dioxide
CO ₂ -EOR	Carbon dioxide enhanced oil recovery
DIRB	Dissimilar iron reducing bacteria
DOE	Department of Energy
DST	Drill stem tests
EOR	Enhanced oil recovery
EPA	U.S. Environmental Protection Agency
FMI	Formation micro-imager
ft	Foot, feet
FZI	Flow zone index
GEM	Composition and unconventional oil and gas reservoir simulator (CMG software)
GEMINI	Geo-Engineering Modeling through Internet Informatics (software)
IT	Interference Test
IRIS	Incorporated Research Institutions for Seismology
KCC	Kansas Corporation Commission
KGS	Kansas Geological Survey
km	Kilometer
km ²	Square kilometer
KU	University of Kansas
LAS	Log ASCII Standard (software)
MBO	Thousand barrels of oil
mD	millidarcys (a measure of permeability)
mi	Mile
mi ²	Square mile
MMBO	Million barrels of oil
MMP	Minimum miscibility pressure
MPa	Mega Pascals
MRIL	Magnetic resonance imaging log
MSTB	Thousand stock tank barrels
MVA	Monitoring, verification, and accounting
NaCl	Sodium chloride
NETL	National Energy Technology Laboratory
NMR	Nuclear magnetic resonance
O	Oxygen
OPAS	Ozark Plateau Aquifer System
pH	Measurement of acidity or basicity of solution
psi	Pounds per square inch

PV	Pore volume
PVT	Pressure-volume-temperature
qPCR	Quantitative polymerase chain reaction
RQI	Reservoir quality index
Rs	Gas–oil ratio
SO ₄ ²⁻	Sulfate
Sr	Strontium
SRB	Sulfate reducing bacteria
UIC	Underground Injection Control
USDW	Underground sources of drinking water
WPAS	Western Interior Plains Aquifer System

INTRODUCTION

The objective of this project was to understand the processes that occur when a maximum of 70,000 metric tonnes of CO₂ are injected into two different formations to evaluate the response in different lithofacies and depositional environments. The evaluation will be accomplished through the use of both in situ and indirect MVA (monitoring, verification, and accounting) technologies. The project was optimized for carbon storage accounting for 99% of the CO₂ using lab and field testing and comprehensive characterization and modeling techniques.

CO₂ was injected under supercritical conditions to demonstrate state-of-the-art MVA tools and techniques to monitor and visualize the injected CO₂ plume and to refine geomodels developed using nearly continuous core, exhaustive wireline logs, and well tests and a multi-component 3-D seismic survey. Reservoir simulation studies mapped the injected CO₂ plume and estimated tonnage of CO₂ stored in solution, as residual gas, and by mineralization and integrated MVA results and reservoir models to evaluate CO₂ leakage. A rapid-response mitigation plan was developed to minimize CO₂ leakage and provide a comprehensive risk management strategy. The project documented best practice methodologies for MVA and completed an application for closure of the carbon storage test.

Many Mississippian-age reservoirs in Kansas are undergoing final stages of secondary recovery and are suitable for CO₂ EOR. It has been previously estimated that recoverable potential for Mississippian Formation reservoirs in Kansas with CO₂ EOR is 250–350 million barrels of oil. Wellington Field (fig. 1) is situated in south-central Kansas near the town of Wellington in Sumner County. It is a typical carbonate reservoir of Mississippian age that has produced 20 MMBO since its discovery in 1929. This field was converted to waterflood after 1957 and is delivering steady secondary production but nearing the end of a cycle with average daily production per well at ~2.6 bbls using 49 active producing wells and 15 injectors out of more than 290 total drilled wells (KGS, 2017).

The Arbuckle Group is a 600–1,000 ft thick and more than 3,500 ft deep carbonate saline aquifer and historically has been a good candidate for various waste disposal operations, such as oil field brine and chemical plant waste disposal. The Arbuckle is currently being considered for commercial scale CO₂ geological storage. It is centrally located near multiple major point sources of CO₂ emissions and a large existing pipeline system with established rights of way that may be useful for implementing commercial-scale distribution from CO₂ source to sink.

Wellington Field (Fig. 1) located in the south-central Kansas near the town of Wellington in Sumner County. It has 49 active production wells and 15 active injection wells producing 132 BOPD. Cumulative oil production is more than 20 million barrels since discovery in 1929. An extensive characterization of the Mississippian reservoir at Wellington Field has been conducted as part of a DOE-NETL funded study (DE-FE0002056) to evaluate carbon storage in southern Kansas.



Figure 1. Map showing the location of Wellington Field, key wells drilled in DE-FE0002056 (KGS 1-28 and KGS 1-32), and the Mississippian injection well drilled under DE-FE0006821 (KGS 2-32).

Part I

CO₂ EOR and Geological Storage in Mississippian Carbonate Reservoir

Many Mississippian-age reservoirs in Kansas are undergoing final stages of secondary recovery and are suitable for CO₂ EOR. It has been previously estimated that recoverable potential for Mississippian Formation reservoirs in Kansas with CO₂ EOR is 250–350 million barrels of oil (Crabtree & Christensen, 2012). Wellington Field is situated in south-central Kansas near the town of Wellington in Sumner County. It is a typical carbonate reservoir of Mississippian age that has produced 20 MMBO since discovery in 1929. This field was converted to waterflood after 1957 and is delivering steady secondary production but nearing the end of a cycle with average daily production per well at ~2.6 bbls using 49 active producing wells and 15 injectors out of more than 290 total drilled wells (KGS, 2017).

The Mississippian group of formations consists of interlayers of limestone and chert that can be divided into older, shallow marine limestone, chert, and cherty limestones, with interbeds of shale, and younger marine and nonmarine shales and sandstones with minor limestones (Newell et al., 1987; Watney et al., 2002). The Upper Mississippian sequence is a limestone and dolostone with interbedded sandstone and shale, as well as some deposits of chert (Goebel, 1968; Zeller, 1968). KGS 1-32 core from the Upper Mississippian was described as a moderately argillaceous, fine

peloidal limestone to micritic lime mudstone with massive chert (Scheffer, 2012). The Upper Mississippian is composed of the underlying Meramecian and overlying Chesterian stages (Goebel, 1968; Zeller, 1968). The unconformity bounds the Chesterian stage and hosts oil reservoirs.

Baseline geologic characterization, geologic model development, studies of oil composition and properties, miscibility pressure estimations, geochemical characterization, reservoir modelling were performed. In March of 2015 the injection well (class II) KGS 2-32 was drilled, cored, and logged through an entire anticipated injection interval. Whole core samples were obtained and tested for porosity and permeability, relative permeability, and capillary pressure. A drill-stem test (DST) was conducted to estimate injection interval permeability and pore-pressure. After the injection well KGS 2-32 was acidized, step rate (SRT) and interference (IT) tests were conducted and analyzed for permeability, well pattern communication, and fracture closing pressure. Based on geological characterization efforts, it was estimated that the average reservoir porosity around KGS 2-32 well is ~25%. And average permeability is 15–25 mD. The reservoir is located in the upper Chesterian stage and high permeability and porosity zones with oil saturations are observed in the upper ~35 m (115 ft). The perforations for the injection well were selected in the upper 16 m (50 ft) of the reservoir and ~7 m (25 ft) were perforated. The Mississippian reservoir's pore fluid pressure is estimated to be below hydrostatic (Bradley, 1975; Sorenson, 2005; Nelson and Gianoutsos, 2011). This departure from the hydrostatic pore pressure is explained by the departure between surface elevations and hydraulic head, which is the result of a major hydrodynamic adjustment associated with post-Laramide uplift, erosion, and formation water discharge (Sorenson, 2005; Nelson and Gianoutsos, 2011). Also, due to oil and gas production in the region and local Wellington Field oil production, the pore fluid pressure of a Mississippian reservoir was measured at ~7 MPa (1,015 psi). The average temperature in the reservoir is ~ 43 °C (~110 °F). The minimum miscibility pressure (MMP) was estimated at ~11.4 MPa (~1,650 psi) (Holubnyak et al., 2017).

Reservoir characterization and properties

The Mississippian reservoir at Wellington Field has been analyzed using a host of data, including continuous core, an exhaustive suite of modern wireline logs, and multi-component 3-D seismic data. These data demonstrate that the reservoir has an average thickness of 42 ft and is moderately fractured at a range of scales, typical of carbonates in general. The reservoir exhibits an upward increasing porosity trend through the midsection of the field, with effective porosity ranging from 5 to 27%. Permeability from whole core in Wellington KGS 1-32 ranges from 0.13 to 60 md.

The data set for the log analysis consisted of 16 wells with complete suites of porosity and resistivity logs drilled from 1956 to 2011. In addition, five older wells had completion dates from 1936 to 1948. These wells had one porosity log, usually neutron logs with no scale, and no resistivity logs. The neutron logs of the five older wells were normalized with the neutron logs of the new well (KGS 1-32), which was drilled and logged specifically for the purposes of the project, and then converted to the equivalent formation porosity. The 16 newer wells were quality controlled and analyzed by Techlog in terms of porosity, water, oil saturation and minerals (fig. 2). Two of these 16 wells (KGS 1-32 and KGS 1-28) had nuclear magnetic resonance (NMR) logs. The NMR logs were analyzed by Techlog to derive Coates permeability and capillary pressure curves (Appendix A-2 – A-4).

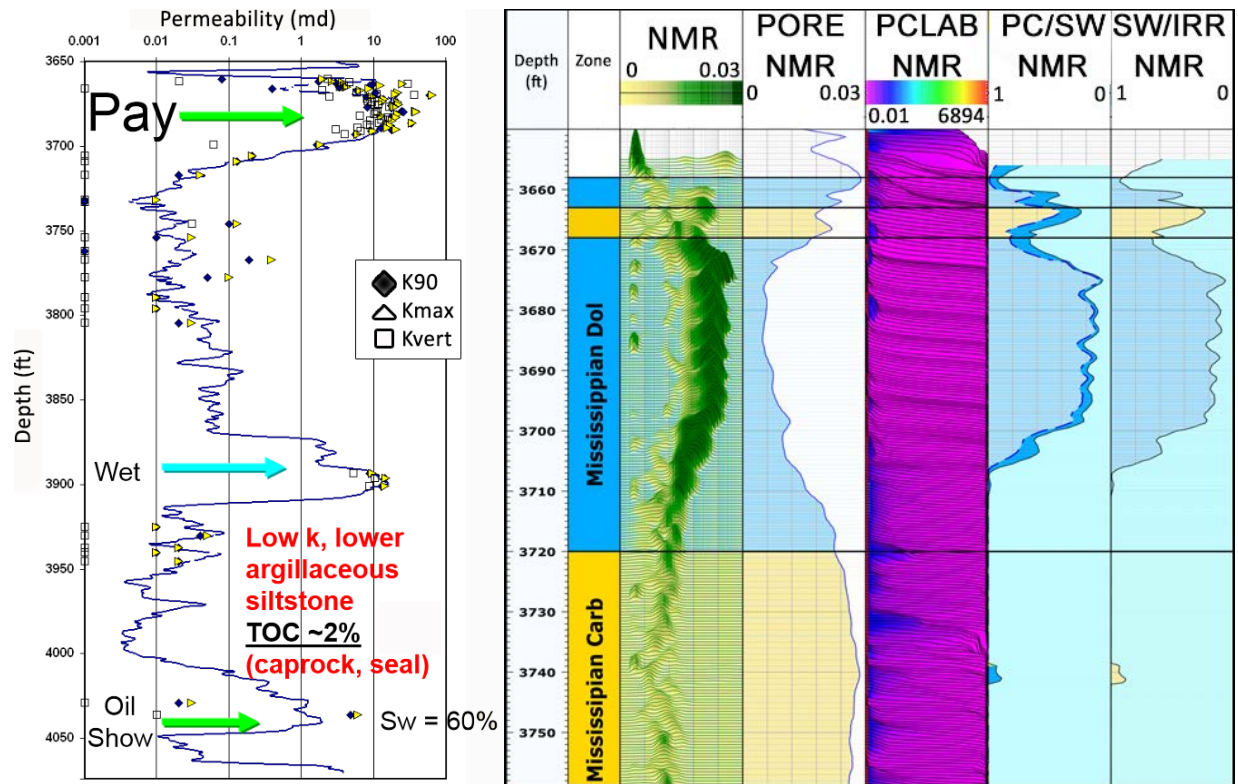


Figure 2. Well KGS 1-32 estimation of permeability based on magnetic resonance imaging (MRIL®) using porosity and T2 center of gravity versus core permeability (left) and NMR log derived porosity (PORE NMR) and water saturations (PC/SW and SW/IRR NMR).

KGS 1-32 was a new well drilled for the purposes of this project with the comprehensive set of modern logs and core; therefore, it was used as the key well. Routine core data of this well were analyzed by Flow Zone Index (FZI) method and FZI-derived values were correlated with log-derived porosity and water saturation of this well (NMR irreducible water saturation). Based on irreducible water saturation and porosity, permeability in KGS 1-32 was estimated; the estimate matched very well with core data and DST analysis (fig. 3) .

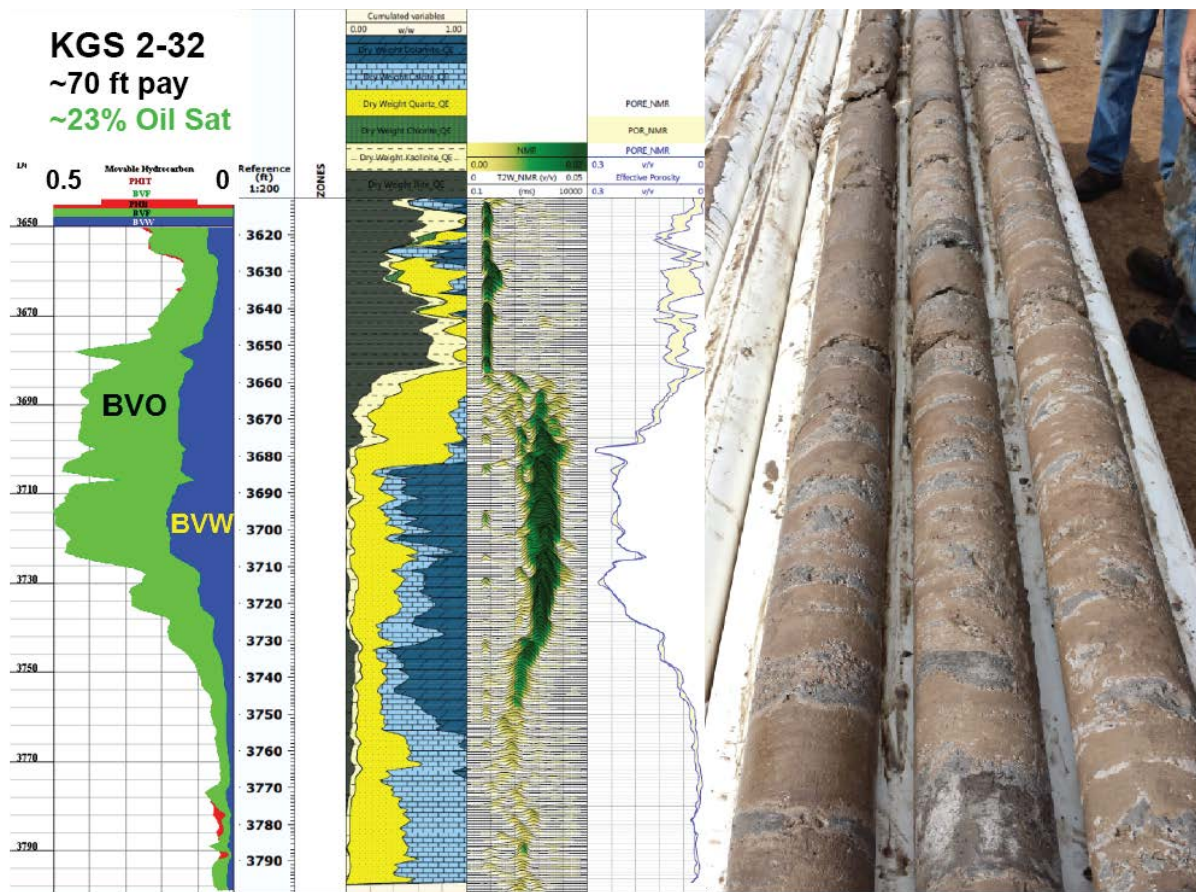


Figure 3. Well KGS 2-32 porosity and permeability estimation based on magnetic resonance imaging (MRIL®) using porosity and T2 center of gravity versus core permeability (left) and NMR log-derived porosity (PORE NMR) and water saturations (PC/SW and SW/IRR NMR).

The application for Class II EOR well KGS 2-32 was filed by Berexco LLC and permitted by the Kansas Corporation Commission (KCC). The permit was obtained to operate a CO₂ EOR well with 2,000 bbls/day of water and 225 metric tonnes of CO₂ per day with maximum allowable operational well head injection pressure of 83 bar for water injection phase and 103 bar for CO₂ injection phase.

In addition to characterization, laboratory analyses, geological and reservoir modelling activities, Kansas Geological Survey (KGS), Berexco LLC, and other team members drilled, cored, and logged new injection well KGS 2-32. Core and well logs were analyzed and interpreted. Flow units defined in a previous phase of work were confirmed and geologic models were updated. Several core plug samples were collected and relative permeability and capillary pressure curves were derived and correlated with prior estimations to be used in reservoir simulation work.

A number of well tests were performed on newly drilled KGS 2-32. DSTs were completed immediately after drilling commenced and after completion; additional well treatment SRTs and ITs were performed and analyzed. Log-derived permeabilities were correlated with values derived from well tests. Fracture gradient, operational pressures, and well communication for the pilot injection area were confirmed. Measured reservoir pressure at five well locations within the pilot area ranged from 50 psi to 70 psi, a departure from the initial 114 bar reservoir pressure.

Background geochemical water and oil sampling was deployed. Two different independent labs were used for this survey: Baker Hughes Oilfield Services and a KGS internal laboratory. Also, pH and total dissolved solids measurements were analyzed routinely in the field for a background survey and as a part of an EOR monitoring program. Inorganic and organic water component concentrations were measured.

Also, an IRIS seismic array that consists of 15 IRIS-PASCAL multi-component seismometers were installed and placed on a cellular network to record background seismic activity at Wellington Field.

The Wellington Field geomodel was updated with new data (fig. 3) and detailed volumetric analysis and oil-in-place forecast was performed. It was estimated that an area with a radius of 1 km around KGS 2-32 well potentially holds up to 1.7M bbls of potentially recoverable oil and it was estimated that ~10% of this volume would be potentially accessible for performed CO₂ EOR. Forecast reservoir simulations were also performed based on the updated geomodel.

Reservoir structural features

Based on core observations, formation micro imaging (FMI), dipole-dipole sonic logs, and regional earthquake focal mechanism analysis, the fracture intensity for a selected upper 35 m (115 ft) of Mississippian reservoir was present but estimated as low. Additional well test analysis and 3-D seismic analysis revealed at least 12 vertical faults with NNE orientation at Wellington Field reservoir and adjacent Anson Bates field (Bidgoli, Schwab, Bidgoli, & Taylor, 2017). Moreover, using the amplitude variation with azimuth (AVAZ) pre-stack method for mapping subsurface seismic anisotropy, which is linked to subsurface stress fields, helped to map fracture density and orientation in the Mississippian reservoir (Graham et al., 2017). The effect of these well-studied structural elements and fractures on fluid flow in the reservoir is discussed in this paper.

A field-wide 3-D multi-component (converted wave) seismic survey was conducted at the Wellington Field. Both well-log and seismic data exhibit high variability in porosity distribution throughout the field. Small faults with up to ~80 ft throw and systematic NE- and NW-trending fractures cut the dolomitic carbonate reservoir in Wellington Field. While effects of small faults and fractures have not been recognized by the operator of the decades-old waterflood in the Mississippian reservoir, potential concerns are raised about their effect on the dispersal, containment, and prediction of injected CO₂.

Preliminary calculations of fault and fracture geometries were performed based on the seismic data in correlation with log analysis. These fault and fractures geometries were included in the existing reservoir model and played an important role in decision making during the selection process of the suitable 5 spot injection pattern that was used in the EOR test.

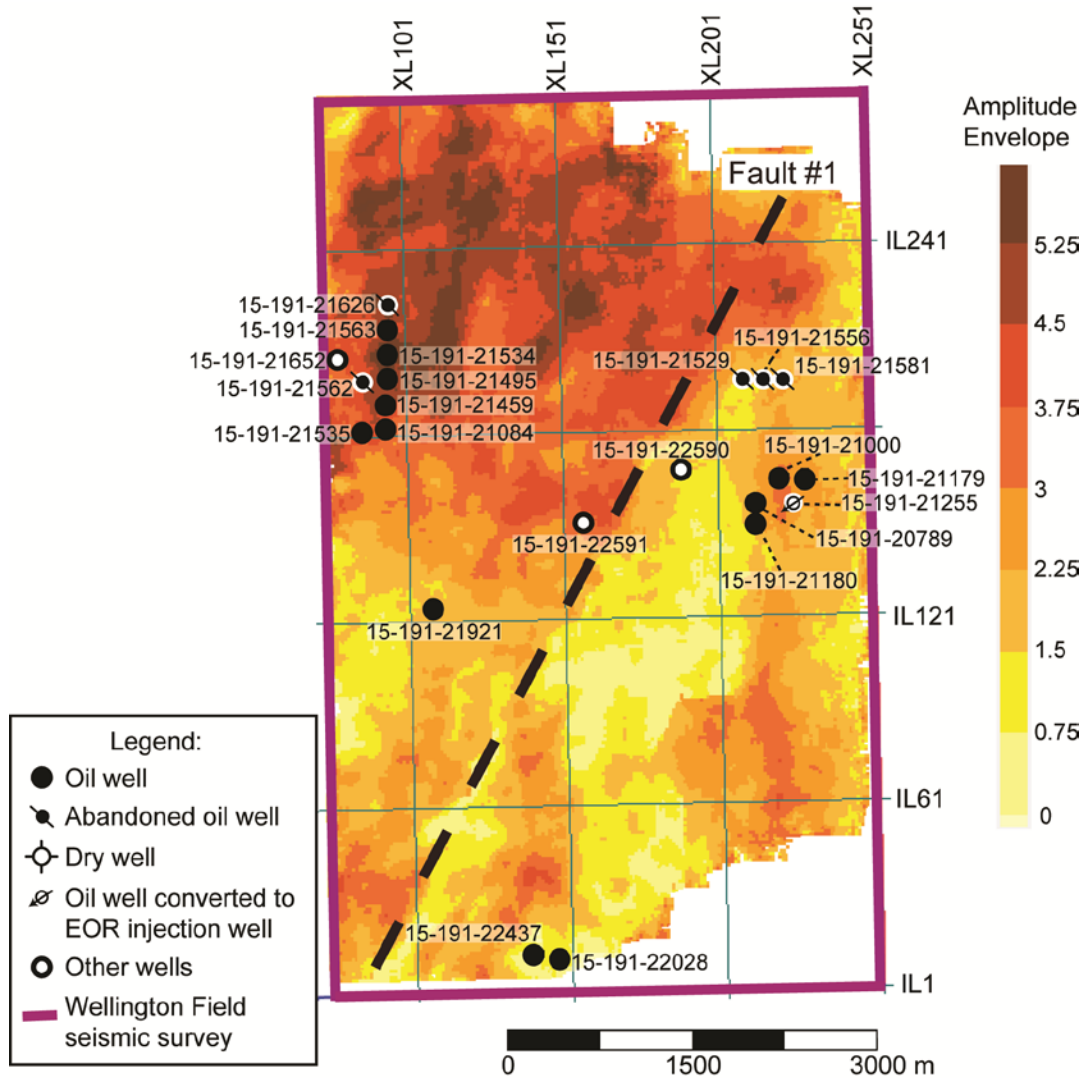


Figure 4. Amplitude envelope map of the Mississippian reflection (top).

Slices from a pre-stack depth-migrated seismic amplitude volume in Wellington Field highlighted suspected faults based on termination of seismic reflections. A five-spot well injection pattern impacted by the two faults is shown (bottom).

Reservoir model: Porosity, permeability, fluid saturations

Schlumberger Petrel's volume attribute processing (i.e., genetic inversion) was used to derive a porosity attribute from the Pre-Stack Depth Migration (PSDM) volume to generate the porosity model. The seismic volume was created by re-sampling (using the original exact amplitude values) the PSDM 50 feet above the Mississippian and 500 feet below the Mississippian formation (i.e., approximate middle of the Arbuckle Formation). The cropped PSDM volume and conditioned porosity logs were used as learning inputs during neural network processing. A correlation threshold of 0.85 was selected and 10,000 iterations were run to provide the best correlation. The resulting porosity attribute was then re-sampled, or upscaled (by averaging), into their corresponding 3-D property grid cell.

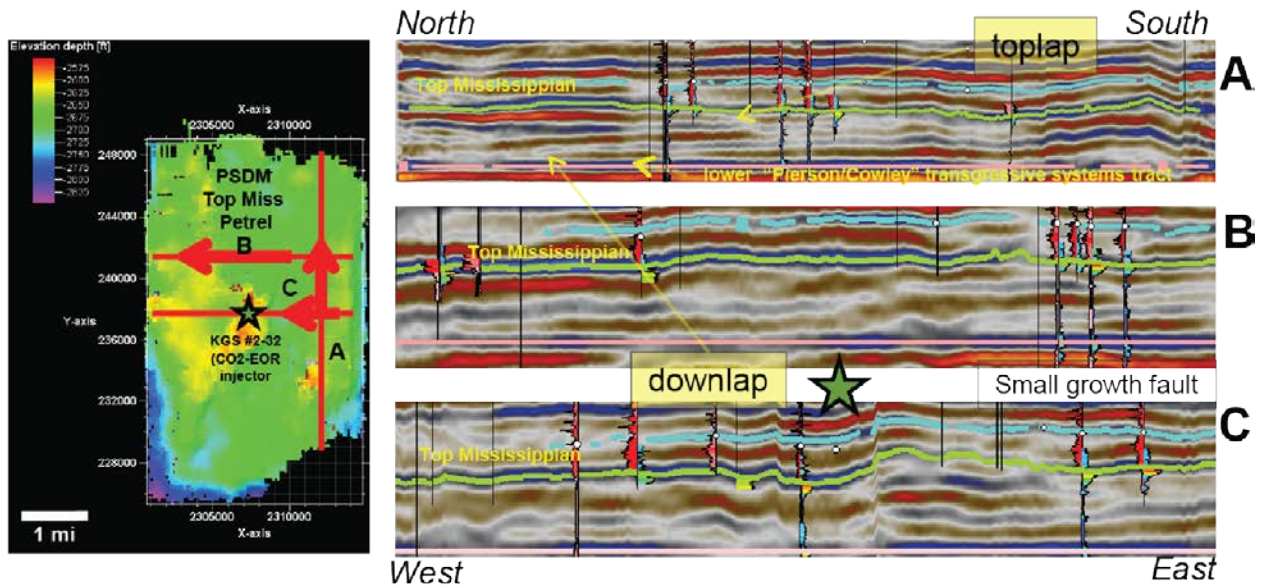


Figure 5. Seismic stratigraphy using PSDM.

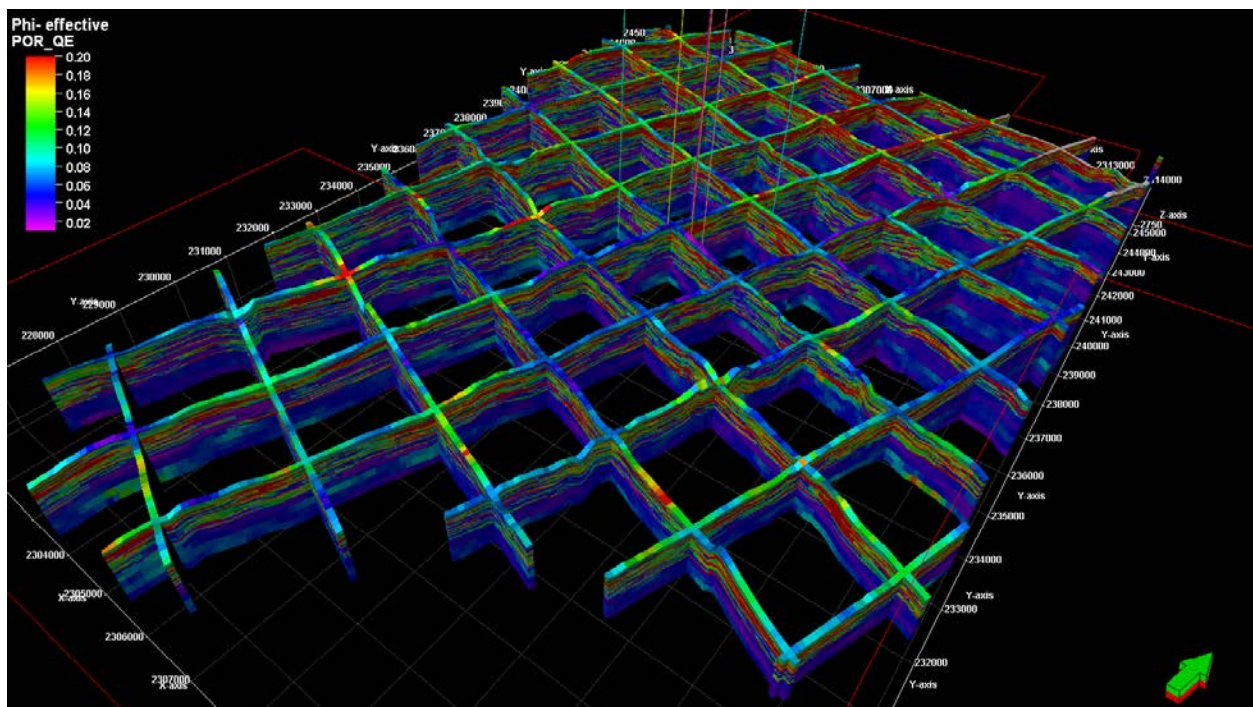


Figure 6. Porosity model.

The porosity model was constructed using Sequential Gaussian Simulation (SGS). The porosity logs were upscaled using arithmetic averaging. The raw upscaled porosity histogram was used during SGS. The final porosity model was then smoothed. The following parameters were used as inputs: 1) Variogram type: spherical with nugget: 0.001; 2) Anisotropy range and orientation: lateral range (isotropic): 5,000 ft, vertical range: 1 ft, distribution: actual histogram range (0.06–0.11) from upscaled logs; 3) Co-Kriging with secondary 3-D variable: inverted porosity attribute grid and correlation coefficient: 0.75. The porosity model is presented in fig. 6.

The upscaled permeability logs shown in were created using the following controls: geometric averaging method; logs treated as points; and method set to simple. The permeability model was constructed using SGS. Isotropic semi-variogram ranges were set to 3,000 ft horizontally and 1 ft vertically. The permeability was collocated and co-Kriged to the porosity model using the calculated correlation coefficient (~ 0.70). The resulting SGS-based horizontal and vertical permeability distribution is shown in fig. 7.

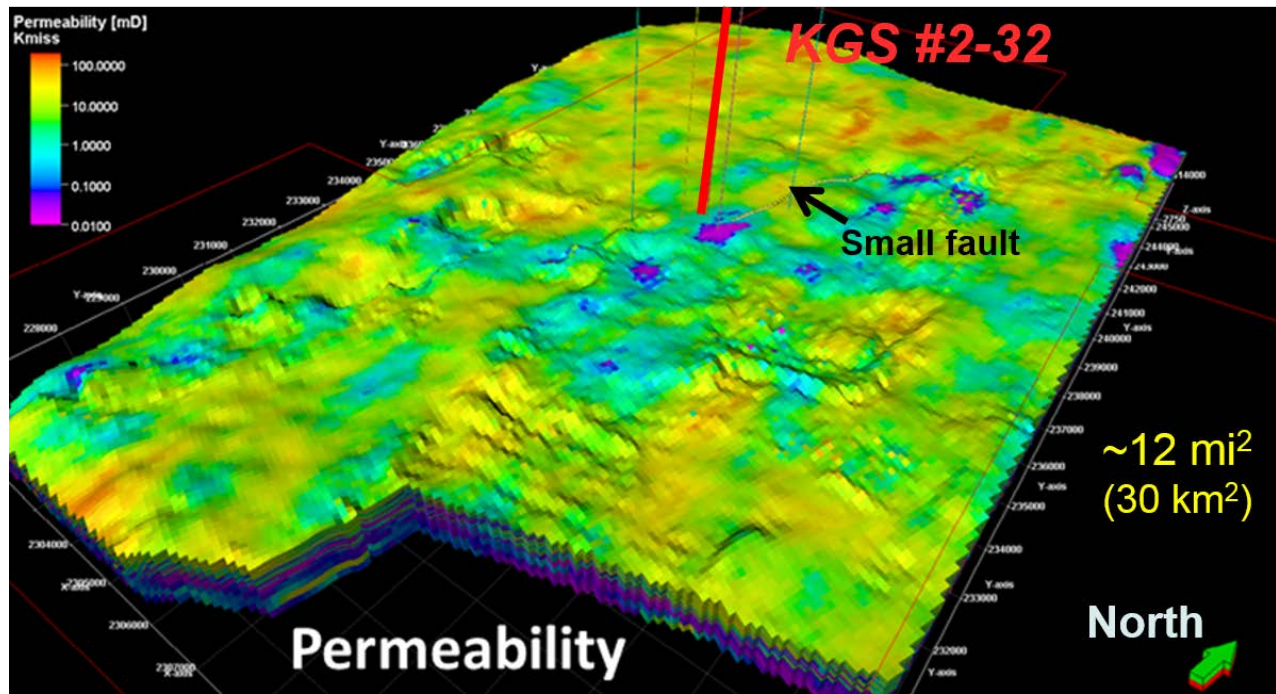


Figure 7. Permeability Model.

In the Mississippian reservoir, reliable initial water saturation from logs (which could be converted to irreducible water saturation) was not available. But NMR data were available for two of the wells and could provide irreducible water saturation in these wells. The water saturation model (fig. 8) was derived based on existing porosity and permeability models and assigned reservoir quality indicator (RQI) ranges.

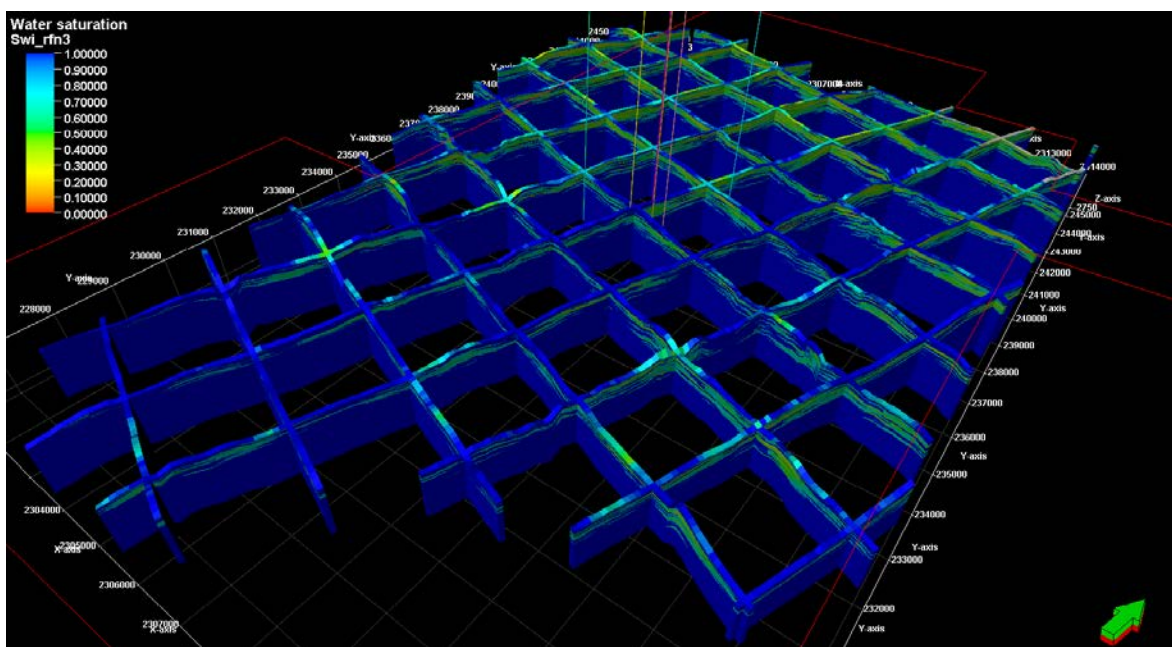


Figure 8. Updated water saturation model for Wellington Field.

Capillary pressure and relative permeability

In the absence of special core analysis data, NMR data for Well 1-32 were used to drive capillary pressure curves for different zones of the reservoir, resulting in generalized capillary pressure curves and NMR irreducible water saturations. Also, core relative permeability data were missing. Based on estimated end points from well 1-32 and generalized data from other fields, relative permeability curves were generated for all rock types. This method is explained in more detail in Appendix A.

Reservoir pressure and temperature

Based on the temperature log of KGS 1-28 and DST flowing temperature of KGS 1-32 (DST 2) and well 1-13 in nearby Wildcat field, temperature in the Mississippian reservoir at the Wellington Field was estimated as 121 degree F. To determine the initial pressure of the Mississippian reservoir, old DST data before water-flood during early production were studied. Pressures from DSTs in the Arbuckle Formation for KGS 1-32 and KGS 1-28 were extrapolated to determine the initial pressure in the Mississippian reservoir. From these calculations, it can be estimated that initial pressure in the Mississippian was 1,480 psi with a pressure gradient of 0.48 psi/ft. Current reservoir pressure at Wellington Field is 1,100 psi.

Laboratory CO₂ miscibility analysis for Wellington Field conditions

A 40 ft sand packed slim tube equipped with a high-pressure glass capillary and a dome-loaded back-pressure regulator was used for the multiple contact miscibility study. The porosity of the sand is 35% and the permeability is approximately 1.5 Darcy. The cleaned slim tube was saturated with toluene. The back-pressure was set at the Wellington Field reservoir conditions and the toluene was displaced by a minimum of 2 pore volumes of crude oil.

The CO₂ was injected at constant rate of 125 cc/min using a motorized high-pressure pump. The oil produced in the separator at the end of the test was recorded and the oil recovery as function of the original oil in place was calculated for each displacement. Six displacement test were conducted at various back pressures. Minimum Miscibility Pressure (MMP) was found to be within operational range of reservoir conditions.

Field operations

Well KGS 2-32 was perforated from 3,661 ft to 3,688 ft (1,116 m to 1,124 m) (Fig. 3) and treated for optimized performance. Several wells within the pilot area were re-entered and treated as well. Because Wellington Field is primarily an oil producing field and has no significant gas production history, gas separation units and gas flow meters had to be installed at well locations and field battery that collects fluid from pilot area.

The CO₂ injection plan assumed that 100–200 metric tons of CO₂ would be injected daily until a total projected volume of 20,000 metric tonnes was reached by mid-June, 2016. The CO₂ was transported to the site in trucks in a liquid state at a pressure of approximately 17 bar and temperature of -24°C. Each truck delivered 20 tons of CO₂. Surface facilities consisted of seven portable tanks that could hold up to 70 tonnes of cooled and pressurized CO₂ delivered by tracks; pump system; programmable logic controller (PLC) that can manipulate the control valve to not exceed the maximum specified flow rate and to ensure that the bottomhole pressure in the injection well does not exceed the maximum allowable pressure. A total of 1,101 truckloads delivered 19,803 metric tons—average of 120 tonnes per day—over the course of injection that lasted from January 9 to June 21, 2016. Total expenditures for purchasing CO₂ were \$1,964,000 with an overall price for CO₂ of \$90.16 per U.S. ton.

Reservoir pressure recordings were obtained through well testing and fluid-level measurements of inactive wells. These pressures were correlated with reservoir simulations to capture field performance dynamics and to guide re-pressurization of the field (Fig. 9). Also, post water injection sensitivity studies were performed to choose an optimal water injection scenario for post-CO₂ operations planning. To achieve estimated Minimum Miscibility Pressure (MMP) of 120 bar based on reservoir simulations, the project planned: (1) to keep current continuous injection volumes for pilot area; (2) to inject additional water through KGS 2-32 at a phased rate of 17 and 40 tonnes/day for a duration of approximately one month before the start of CO₂ injection; (3) to continue with water injection at 82 tonnes/day at KGS 2-32 after CO₂ injection commenced.

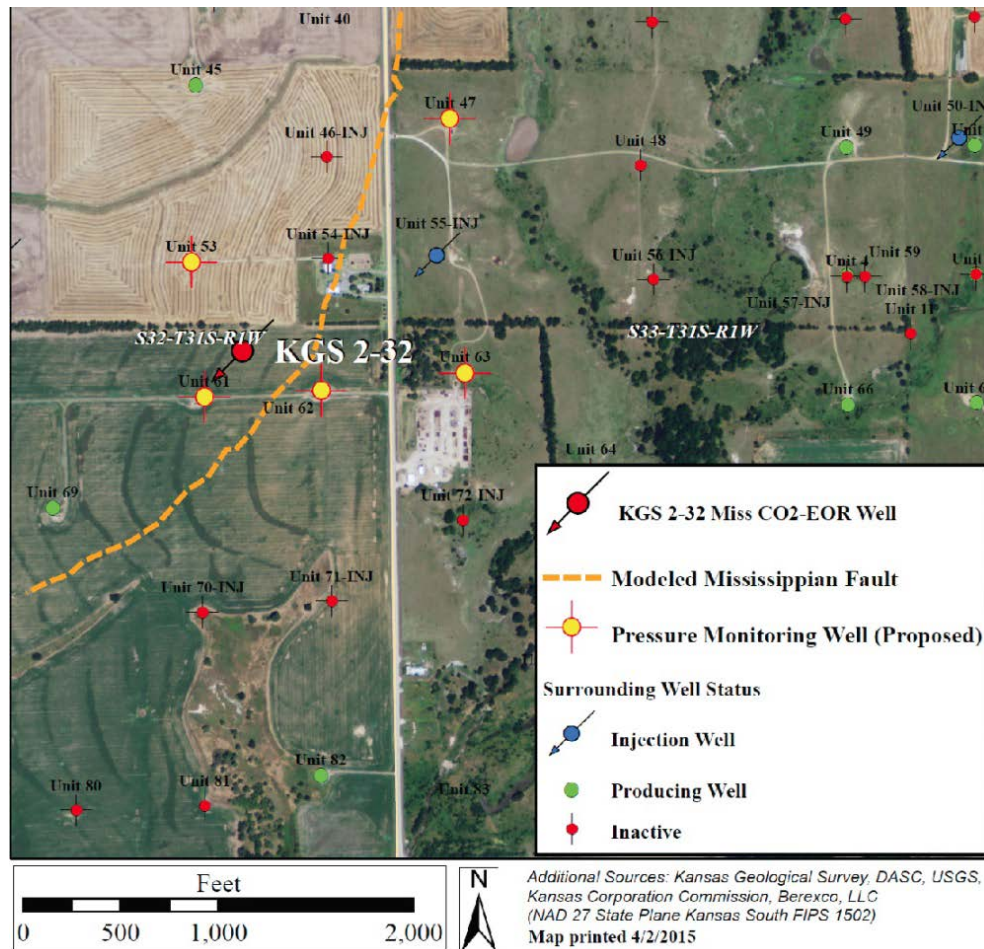


Figure 9. Pilot area aerial map with marked injection wells, sampled wells, and wells used for SRT.

Monitoring survey

A geochemical water analysis of organic and inorganic components was performed to understand whether this method could be used as an early CO₂ detection system and as a plume location and containment method. In addition, the analysis also helped to understand the degree of impact of CO₂ on mineral composition and changes in water and rock geochemistry as a result of injection. Along with a geochemical survey, pressure and production data were recorded at wells and tank batteries.

Based on reservoir simulations, wells surrounding the CO₂ injector well were grouped in three areas: two inner circles with the radiuses of 597 ft and 1,509 ft (182 m and 460 m). Wells within these radiuses were sampled weekly during the course of CO₂ injection, beginning January 9, 2016. Wells within a third radius of .62 mi (1 km) around KGS 2-32 were sampled after initial break-through at the wells of the first inner circle; however, sampling interval for these wells was chosen according to flood performance and was not strictly set from the beginning of the injection. In total, an analysis of 17 wells surrounding the injector well was performed. In addition, the project contracted Baker and Hughes Oilfield Services to conduct monthly geochemical sampling after injection began.

Total dissolved solids and pH measurements were analyzed in the field and alkalinity analysis was performed in the lab shortly after sample arrival. These results were used as an early detection for CO₂ arrival at well locations (fig. 10). On average, wells started to produce CO₂ 2–3 weeks after initial increase in alkalinity. However, some wells did observe alkalinity increase without free gas production. Collected data contains cation, anion, and organic components.

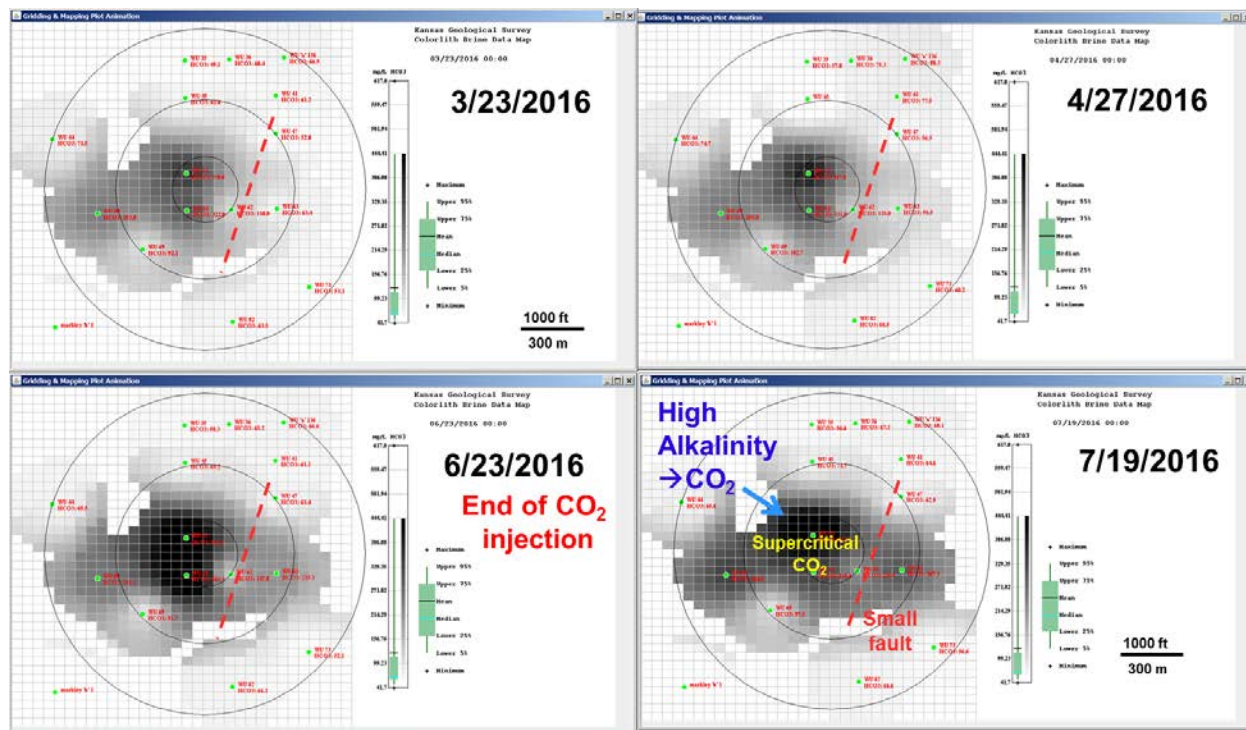


Figure 10. Alkalinity progression.

Reservoir simulations

The main goal for this task of numerical simulations was to determine the outline of the CO₂ front for optimal monitoring of the EOR performance, efficiency, and CO₂ movement through existing structural elements.

The reservoir simulations were conducted using the Computer Modeling Group (CMG) GEM simulator. GEM is a full equation of state compositional reservoir simulator with advanced features for modeling the flow of three-phase, multi-component fluids. The code can account for the thermodynamic interactions between three phases: liquid, gas, and solid (for salt precipitates). Mutual solubilities and physical properties can be dynamic variables depending on the phase composition/system state and are subject to well-established constitutive relationships, which are a function of the system state (pressures, saturation, concentrations, temperatures, etc.).

The Petrel-based geomodel mesh discussed above consists of a 130 x 114 horizontal grid and 32 vertical layers for a total of 451,887 cells. The model domain encompasses a 1.56 miles² area and the formations from the base to the top of Mississippian formation. This grid with populated reservoir parameters (permeability, porosity, and water saturation) was imported to CMG Builder, where other reservoir properties discussed above were applied. Boundary

conditions were determined as Carter-Tracy aquifer with allowed leakage. Historical matching of the field performance was performed with CMOST software from CMG.

Based on preliminary models, the CO₂ front movement is going to be affected by several factors: 1) Existing water flood created pressure gradients that would stir the CO₂ front; 2) existing faults and associated damage zones were likely to contain and redistribute the CO₂ in the reservoir, influencing and directing CO₂ movement (fig. 11); and 3) the most efficient EOR was predicted to be in the vicinity of a mapped fault; however, this hypothesis, needs further verification with field implementation. The project planned to monitor CO₂ front movement with additional seismic equipment (passive and active components) and chemical tracers for improved control and verification of the model. Based on reservoir simulations, optimization patterns for post-CO₂ water injection were selected for optimal reservoir performance (fig. 12).

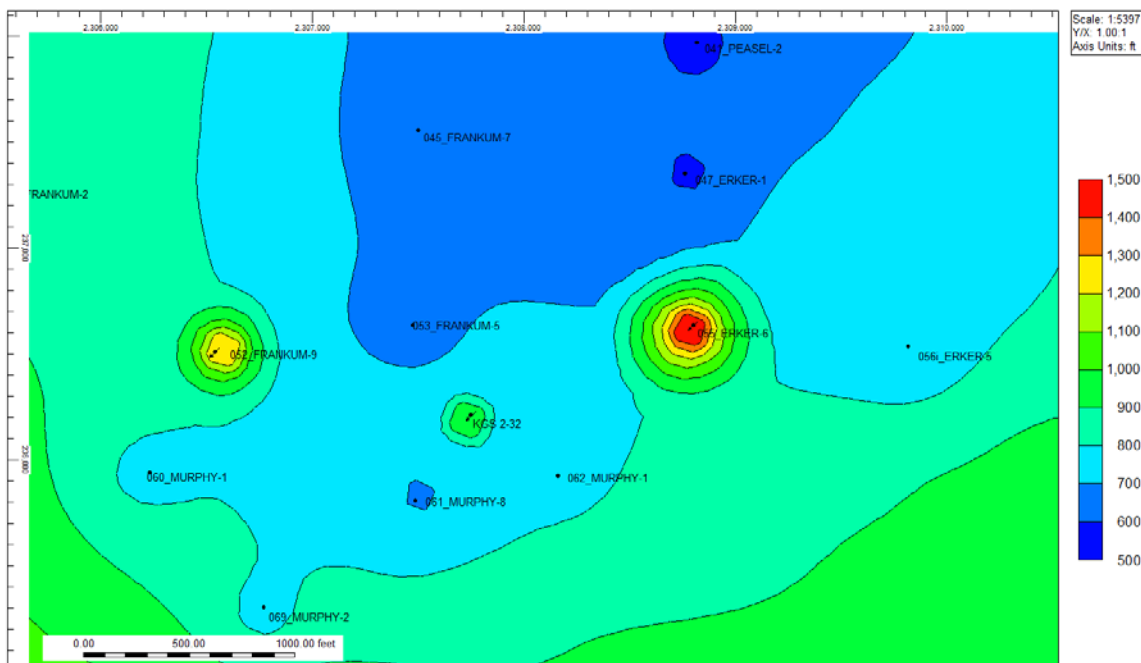


Figure 11. Modeled and history-matched reservoir pressure distribution map (delta psi).

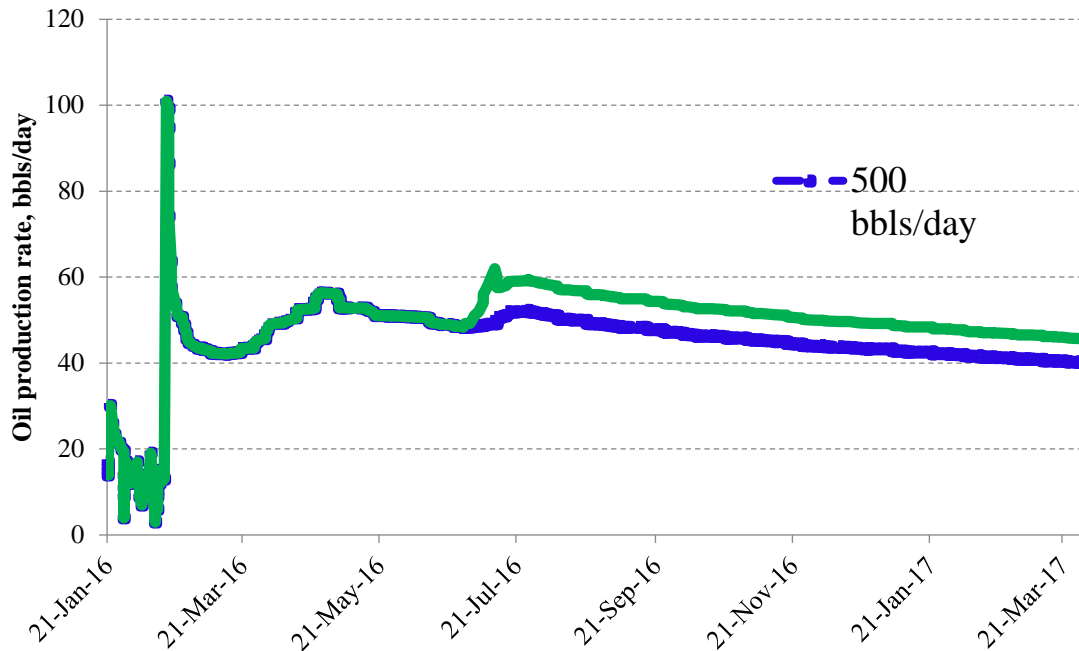


Figure 12. Modelled oil production forecast that explores sensitivity to water injection volumes at KGS 2-32

Results

The main objectives of this study were met. The CO₂ EOR flood at Wellington Field was carried out safely and efficiently. Oil production has increased with current steady performance: no decline signatures have been detected yet. Current incremental average oil production rate is 34 bbls/day and a total of incremental 6,300 bbls of oil was produced by the end of September 2017 (fig. 13).

CO₂ injection was performed in a highly controlled and monitored environment (fig. 14), which is in line with developed rapid-response detection and mitigation procedures and could be applied toward an operation and risk management plan for EPA Class VI well permits. Simple but robust monitoring technologies proved to be very efficient in detecting and locating CO₂. High CO₂ reservoir retentions with low yields within an actively producing field could help to estimate real-world risks of CO₂ geological storage. Only 18% of injected CO₂ was produced back (fig. 13).

Overall, Wellington Field is proving to be a viable field laboratory with a high degree of control and understanding of reservoir dynamic performance (fig. 15).

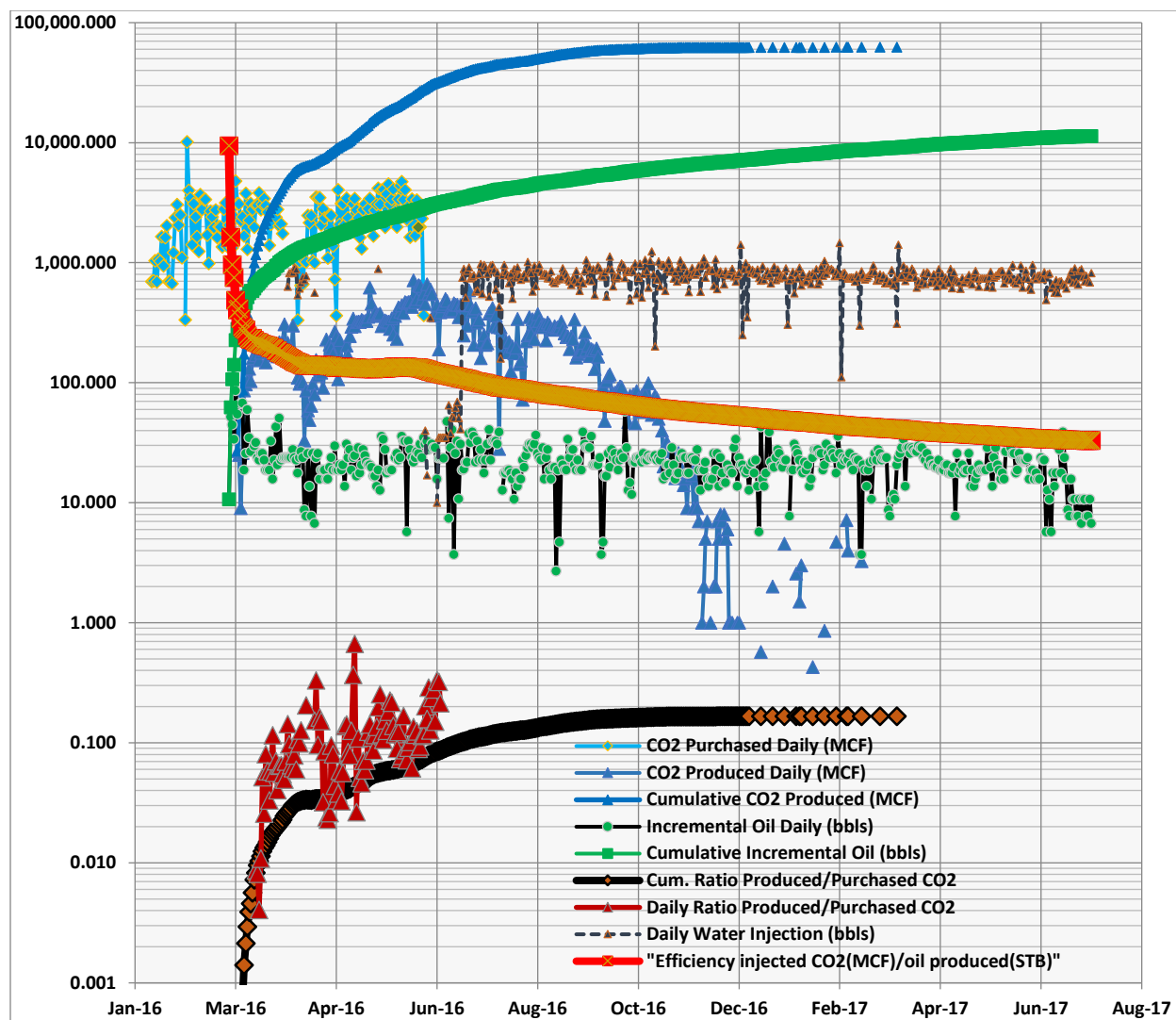


Figure 13. CO₂ injected and CO₂ and oil recovered in pilot scale injection in the Mississippian oil reservoir in Wellington Field.

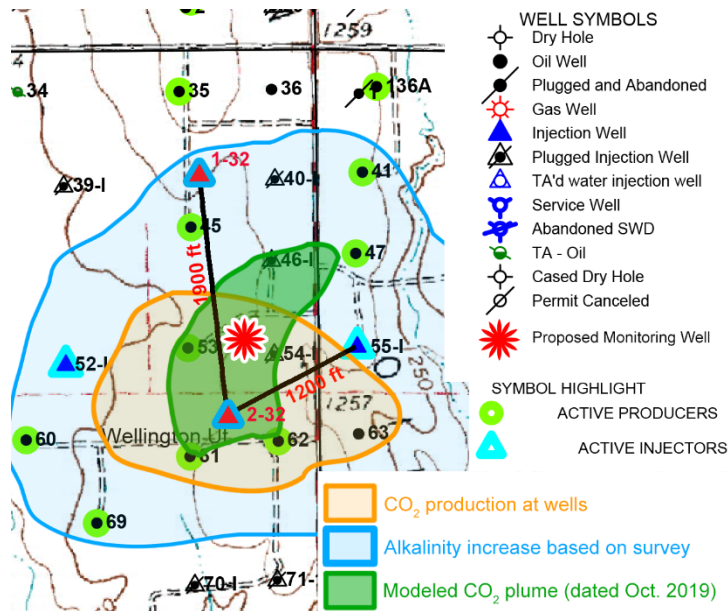


Figure 14. Wellington Field map showing well locations and the extent of the CO₂ plume (orange outline) versus observed alkalinity increase (blue outline) versus simulations CO₂ plume predicted by (green outline).

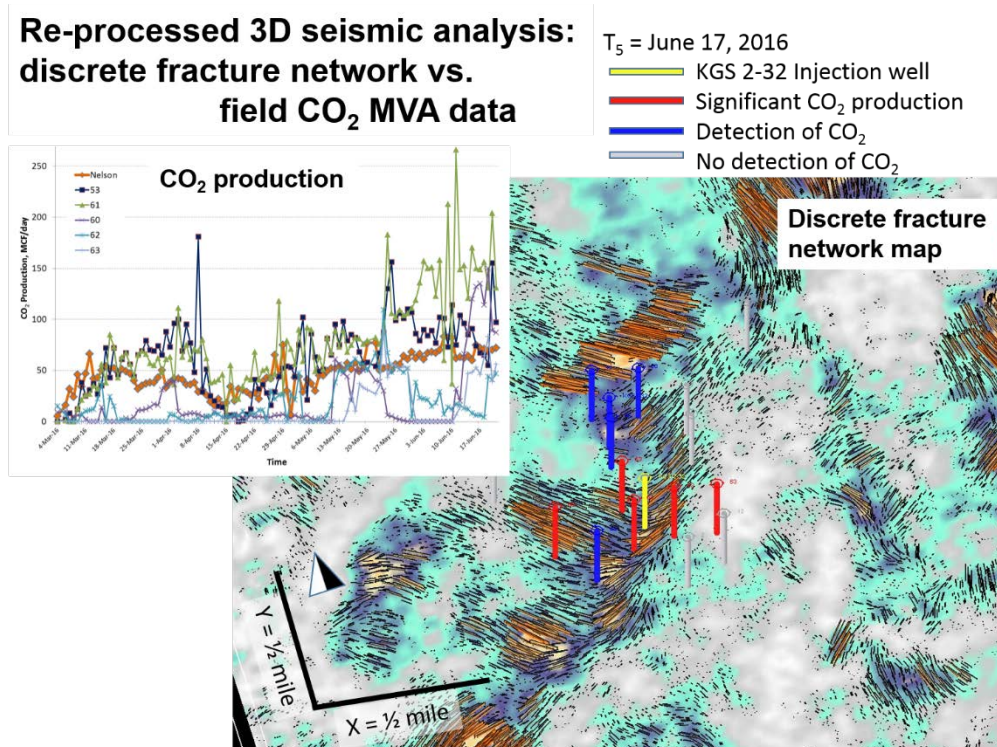


Figure 15. Re-processed 3-D seismic showing fracture network, surveyed well locations, and the extent of the CO₂ plume.

Decline curve analysis

East Nelson tank is the only tank where additional oil produced by CO₂ was observed. Additional oil production by CO₂ has not been observed in other tanks (Erker, West Nelson and Peasel). Therefore, decline curve analysis was done only for East Nelson tank using Fekete Harmony commercial software.

Abandonment rate of 200 bbl/month was considered for this analysis; where, the two curves intersect at 200 bbl/month at the end of the forecast. Harmony Fekete calculated the cumulative oil production for each curves in the table below from the start of forecast to the end. Forecast of oil production by mean of waterflood is shown in red and forecast of oil production by mean of CO₂ flood is shown in dark green. The difference between the two cumulative oil productions is the cumulative additional oil by only CO₂ flood (the area between the two curves).

The area between the curves is $68,982 - 36,542 = \mathbf{32.44 \text{ Mstb}}$ which is the cumulative additional oil production by only CO₂ flood. Cumulative oil production by CO₂+waterflood from the start of CO₂ response to the end of forecast period which is April 2027 is **68.982Mstb** (Table below). Next month history may change the slope.

Harmony software calculated the cumulative oil production for each curve in the table below from the start of the forecast to April 2027. The difference between the two cumulative oil productions is the cumulative additional oil by CO₂ flood (the area between the two curves in fig. 16). The area between the curves equals to ~32 Mstb (thousand stock tank barrels), which is the cumulative additional oil production by only CO₂ flood. Cumulative oil production by CO₂+ waterflood from initial CO₂ response to April 2027 is ~69 Mstb (Table 2). However, additional observations may change the slope.



Figure 16. Decline curve analysis for Wellington Field.

Table 1: Conversion factors

1	metric ton =	1.10231	US ton
1	US ton =	17.19	mcf
1	metric ton =	18.9487	mcf

Table 2. Cumulative oil production predictions from decline analysis results.

Performance Comparison	Start of Decline Date	Oil Production Rate, bbls/day	Forecast Start Date	Cumulative Oil Production, Mbbls	Forecast End Date	Delta Time, months	Delta Cumulative Oil Production, bbls
CO ₂ EOR + Waterflood	Feb. 2016	36	Feb. 2016	45	Apr. 2027	134	69
Waterflood	Aug. 2009	12	Feb. 2016	45	Apr. 2027	134	37

WELLINGTON CO₂ EOR EFFICIENCY

Wellington Mississippian EOR was a 10-acre pilot test. One of the objectives of Wellington pilot was to demonstrate that CO₂ EOR is a feasible option for Kansas' oil fields if the necessary infrastructure were developed. It is important to note that normally, CO₂ EOR pilots are less efficient than commercial operations due to lack of directional and precise well control, lack of surface facilities for CO₂ recycling, and other factors.

21,784 US tons of CO₂ was purchased for \$1,964,063 from Dec 2015 to June 2016 based on last invoice received from Berexco. Decline curve analysis forecast of additional cumulative oil production by only CO₂ flood (above the line of water flood on Fig. 16) is 32.44M STB for the end of 2027. Using 32M STB oil production and \$1,964,063 cost of CO₂, CO₂ EOR cost per barrel of oil production is ~\$60.

The high cost of CO₂ in the case of Wellington project is explained by two factors: (1) currently, there is no extensive CO₂ capturing and transportation infrastructure in Kansas; and (2) CO₂ was captured from an anthropogenic source.

Wellington Mississippian pilot efficiency by the end of forecast calculations is **11 MCF per barrel of produced oil**. Full field-scale CO₂ EOR report better efficiencies: ~5 MCF per barrel of produced oil (Ref: Permian basin CO₂ EOR & OK EOR

<http://www.ogj.com/articles/print/volume-92/issue-6/in-this-issue/production/co2-for-eor-is-plentiful-but-tied-to-oil-price.html>). However, if Wellington field is equipped with CO₂ recycling infrastructure and a full field flood is deployed, similar efficiencies are achievable.

Site Characterization and Modeling for Arbuckle Saline Aquifer CO₂ Injection

The Arbuckle Group is a 600–1,000 ft thick and more than 3,500 ft deep carbonate saline aquifer and historically has been a good candidate for various waste disposal operations, such as oil field brine and chemical plant waste disposal. The Arbuckle is being considered for commercial-scale CO₂ geological storage. It is centrally located near multiple major point sources of CO₂ emissions and a large existing pipeline system with established rights of way that may be useful for implementing commercial-scale distribution from CO₂ source to sink.

Class I and Class II wells for waste water and hazardous waste disposal have many decades of operation in Kansas (fig. 17) with hundreds of millions of barrels of oilfield backflow water and hazardous waste disposed over the years in various geologic formations across the state. In recent years, with development of the Mississippian Lime Play (MLP) and its high water cuts ranging up to 95%, concerns have been raised due to increase in seismic activity associated with the injection of many tens of millions of barrels of back-flow brine in the Arbuckle Group interval. In the area of high-volume brine disposal, the Arbuckle overlies a portion of the late Proterozoic Midcontinent Rift System consisting of a kilometer-thick succession of low porosity arkosic sediment, volcanics,

and igneous intrusives that are cut by a complex fault network. Some of these older faults were reactivated during the Paleozoic, offering the potential to permit wastewater to enter the basement.

Prior to MLP development, the Arbuckle was extensively used as a disposal target; however, injection volumes rarely exceeded 2,000 bbls (325 tonnes) of brine per day, according to KCC-reported injection volumes. In the early days of MLP development, the allowed daily brine injection rates were set to 20,000 bbls per day. With rapid developments of MLP, some companies started to operate permitted disposal wells at full capacity, a rate that had not been observed before. Some locations even had twin wells, drilled within a few tens of meters from each other, permitted to inject at the same rate. However, the KCC issued two consecutive orders that downscaled the allowed injection rates within specified areas. Since August 2016, injection rates have been reduced from 16,000 to 8,000 bbls/day in areas of concern spanning 1,500 sections of Harper, Sumner, Kingman, and Sedgwick counties.

To compare these developments with potential CO₂ geological storage scenario: previously allowed rate of injection of 3,250 tonnes of brine a day is roughly equivalent to 1,700 tonnes of CO₂ per day and injected mass of brine of 17.2M tonnes for 2014 in Harper County, Kansas, is roughly equivalent to 9M tonnes of CO₂ per year. This means that some brine disposal wells operated at a rate comparable to a commercial-scale CO₂ storage project, and the brine disposed in Harper County is equivalent to the simultaneous operation of nine commercial-scale CO₂ geological storage projects. It should be noted that brine disposal volumes in adjoining counties across the Kansas-Oklahoma border were even larger, and we believe this combined volume of brine has contributed to induced seismicity in the region.

There is evidence from independent pressure monitoring gages, UIC Class I well monitoring records, and other sources of regional fluid level and pore pressure increases in the Arbuckle reservoir in Kansas and Oklahoma. Competing interests of various industrial groups that include oil and gas, chemical complex, and potentially CO₂ geological storage could collide in the future if a regulatory framework is not outlined and expanded.

depositional alteration of Arbuckle limestone to dolomite occurred when freshwaters rich in magnesium and calcium mixed with the local marine waters (Jorgensen et al., 1993). The Arbuckle consists mainly of white, buff, light-gray, cream, and brown crystalline dolomite (Zeller, 1968). Chert is possible in the upper portion of the Arbuckle Group. The top of the Arbuckle in the central portion of Sumner County is at a depth of approximately 4,000 ft below land surface. The Arbuckle Group is regionally extensive throughout Kansas with the exception of some structurally high areas on the Central Kansas uplift and the Nemaha anticline where the Arbuckle has been removed by erosion (Carr, 1986). The elevation to the top of the underlying Precambrian basement in Sumner County varies from 0 ft mean sea level (MSL) in the northeast to -6,000 ft MSL in the southwest (Fig. 19). The Arbuckle generally thickens as a whole from north to south and is thickest (up to 1,100 feet) in south-central Kansas. The east-west and north-south cross sections in Figure 20 highlight the lateral continuity of this group at the Wellington site and in Kansas of the Ozark Plateaus aquifer system and the adjoining Pennsylvanian and Precambrian systems (from Carr et al., 2005).

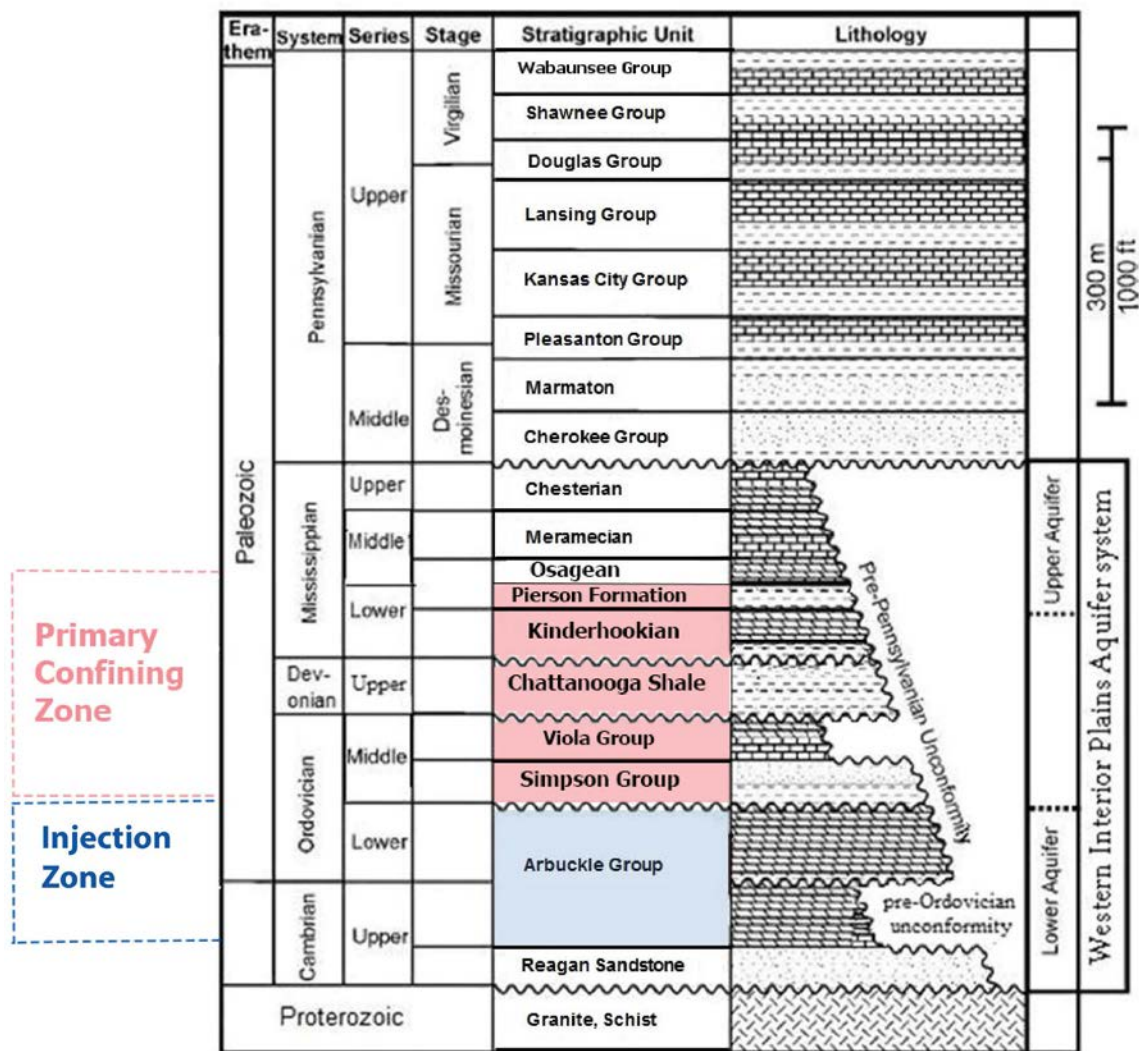


Figure 18. Generalized stratigraphy of Kansas showing the relative position of the lower and upper aquifers.

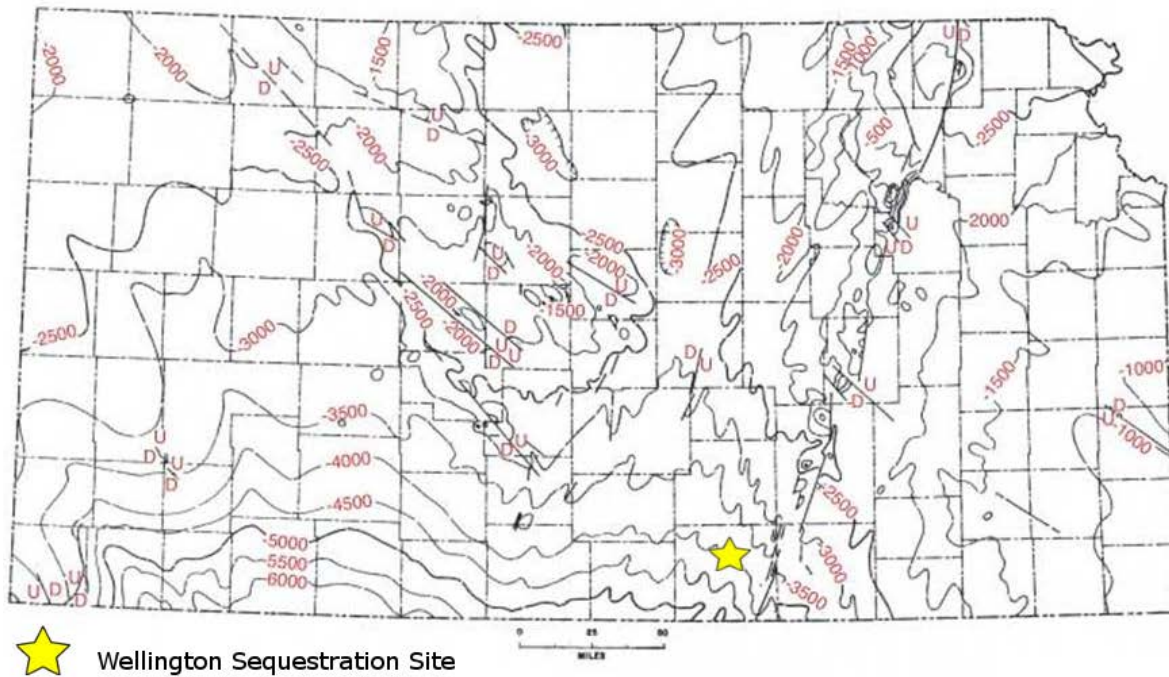
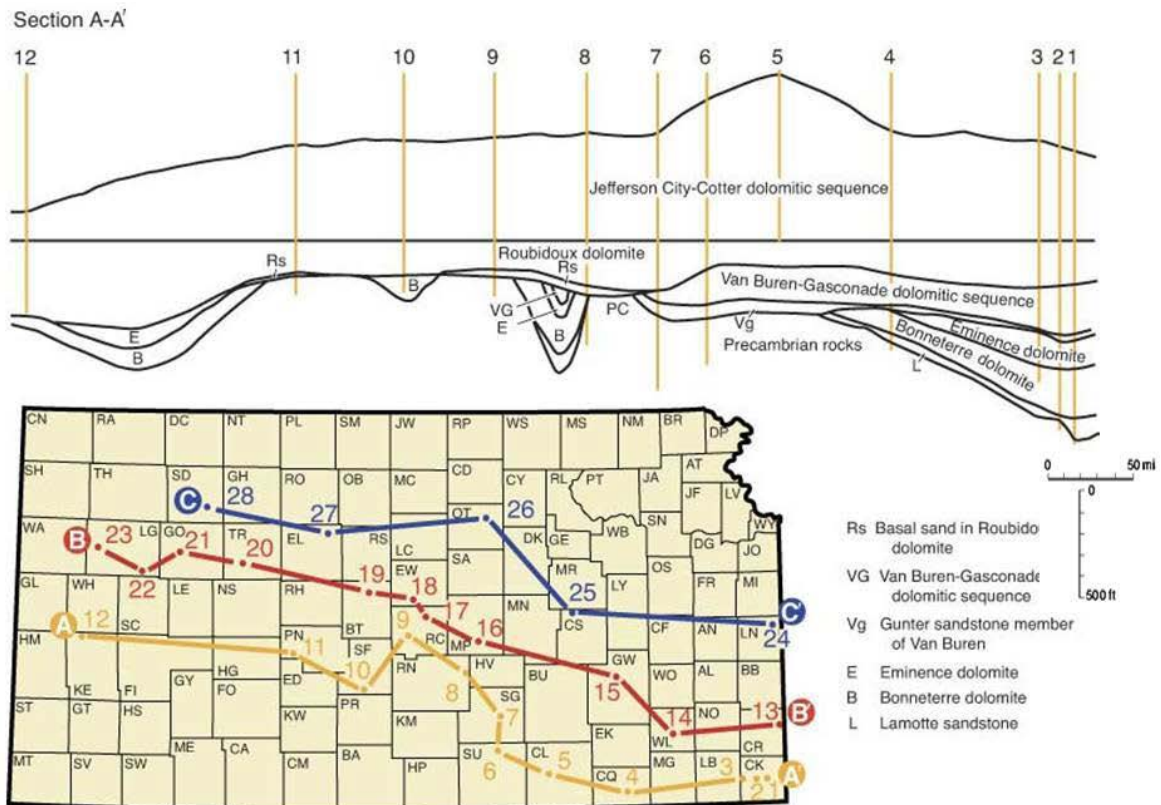


Figure 19. Elevation (ft MSL) to top of Precambrian basement complex in Kansas (from Franseen, 2004).



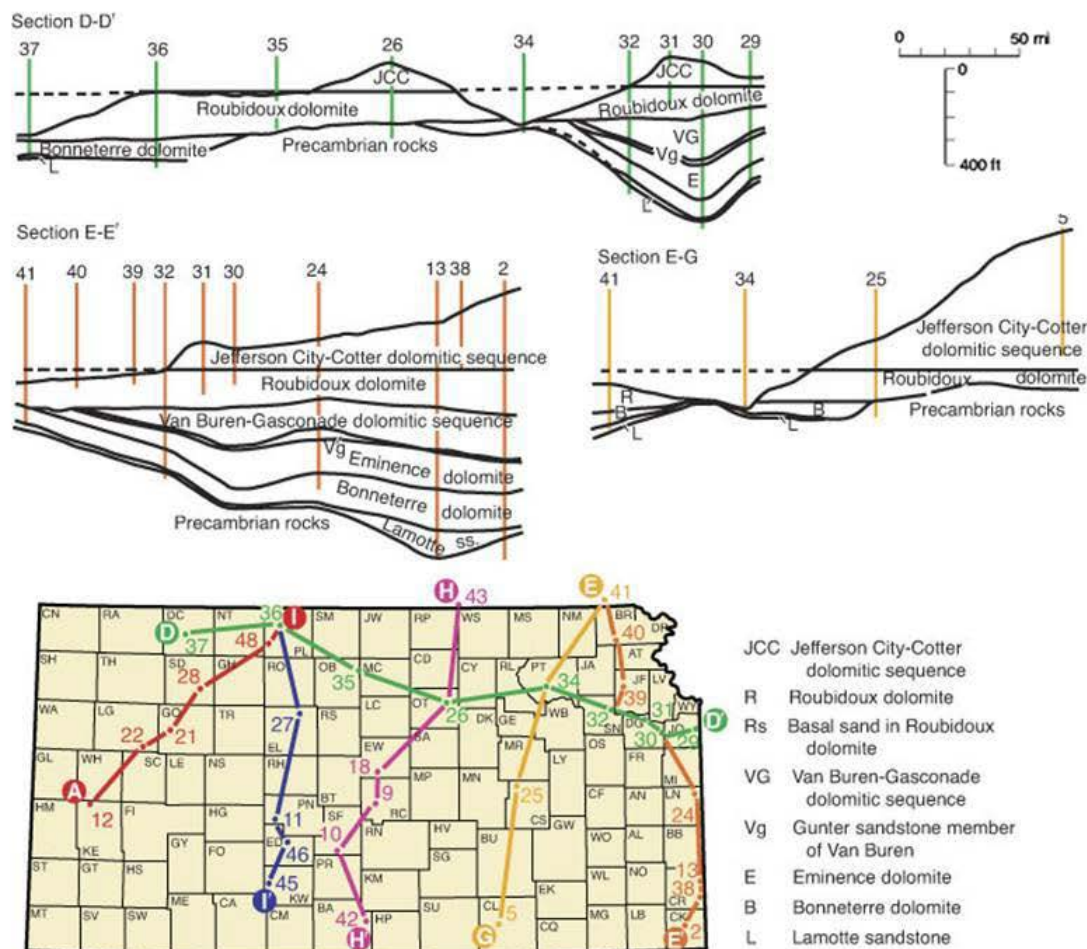


Figure 20. Diagrammatic east-west cross section of Cambrian-Ordovician (Arbuckle Group) strata across Kansas (top) and diagrammatic north-south cross section of Cambrian-Ordovician (Arbuckle Group) strata across Kansas (bottom) (from Franseen et al., 2004).

Hydrogeology

The Arbuckle aquifer system in Kansas, Missouri, and Oklahoma make up one of the largest regional-scale saline aquifer systems in North America and are present in both the Western Interior Plains aquifer system (WIPAS) and the Ozark Plateaus aquifer system (OPAS). The WIPAS underlies almost all of Kansas. Table 3.1 lists the stratigraphic units along with the associated geohydrologic units that make up the WIPAS and the geologic units overlying it. The WIPAS is similar to the OPAS, which lies to the east in parts of Missouri and southeastern Kansas. Unlike the OPAS, the WIPAS is naturally saline and yields no freshwater (TDS <1,000 ppm) (Faber, 2010). Sumner County lies in the WIPAS, and Arbuckle brine concentrations within the county are significantly in excess of 10,000 mg/l salinity. The salinity decreases significantly in the eastern part of the state, where the WIPAS merges with the OPAS. Another key feature of the Arbuckle salinity distribution in Kansas is the general increase in Arbuckle TDS from north to south (fig. 21).

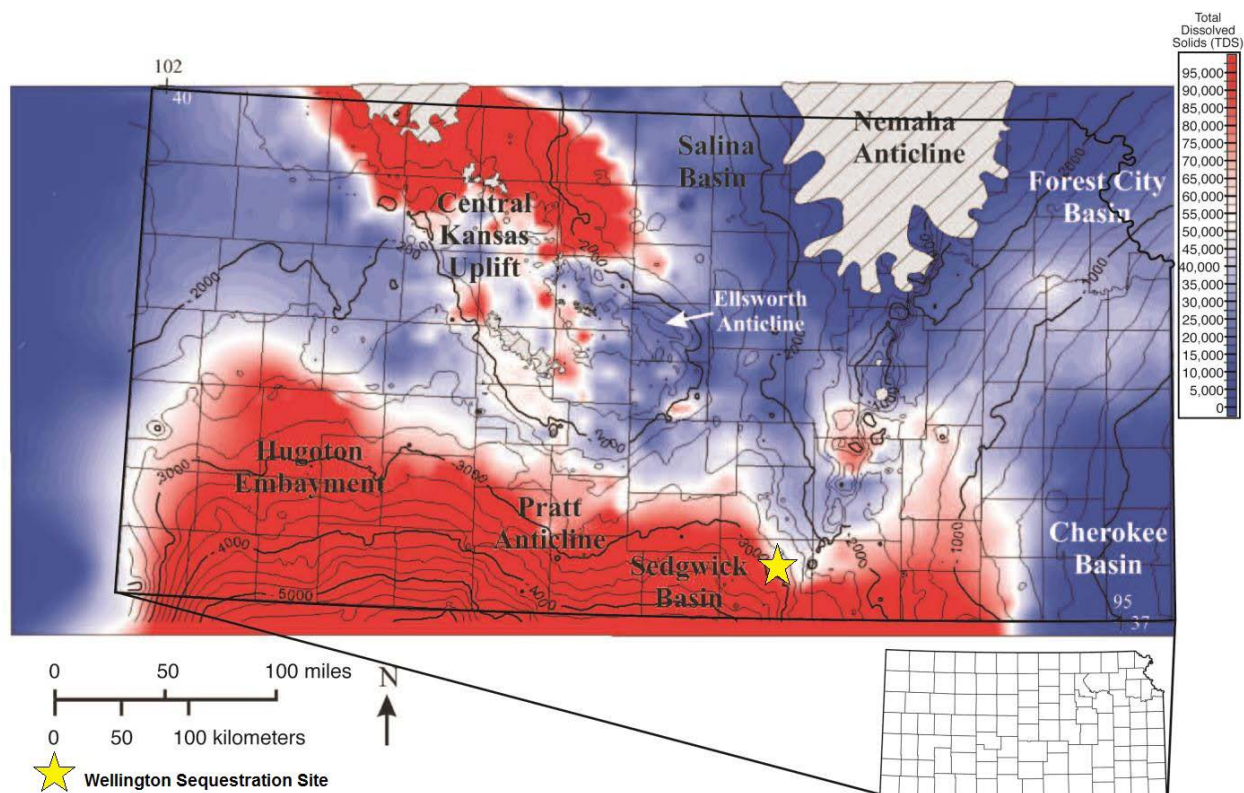


Figure 21. Total dissolved solids (ppm) in Arbuckle brines. Overlay is the structure (ft, msl) on top of Arbuckle (from Carr et al., 2005).

Brine salinity distribution in the Arbuckle is also associated with structural features. Dense brines along the Kansas-Oklahoma border are concentrated in Arbuckle structural lows, particularly in southwestern Oklahoma. Arbuckle brine salinity slowly decreases northward and along the eastern side of the Nemaha anticline. An area of relatively dense brine surrounds the Cambridge Arch (northern part of the Central Kansas uplift) and extends southward along the east side of the Central Kansas uplift. On the Central Kansas uplift, small areas of increased TDS concentrations are associated with areas where the Arbuckle has been removed by erosion, or the high tops may be partly due to brine injection from oil field operations (Jorgensen et al., 1993). Relatively low-salinity WIPAS brines (TDS 5,000–20,000 ppm) are located along the Colorado-Kansas border and in north-central Kansas where the Arbuckle has been removed by erosion. At the Wellington test well sites (KGS 1-28 and KGS 1-32), Arbuckle brines from DSTs and swab tests had TDS values ranging from 48,000 mg/L in the Upper Arbuckle (4,182 ft) to 180,000 mg/L in the lower Arbuckle (5,005 ft).

The ambient pore pressure, temperature, and salinity vary nearly linearly with depth in the Arbuckle Group. By linear extrapolation, the relationship between depth and these three parameters can be expressed by the following equations:

$$\text{Temperature (}^{\circ}\text{F)} = (0.011 * \text{Depth} + 73.25) \quad \text{Pressure (psi)} = (0.487 * \text{Depth} - 324.8)$$

$$\text{Chloride (mg/l)} = (100.9 * \text{Depth} - 394.786)$$

Where, depth is in feet below kelly bushing (KB)

Using the above relationships, table 2 presents the temperature, pressure, and salinity at the top and bottom of the Arbuckle Group at the injection well site (KGS 1-28).

Table 2. Temperature, pressure, and salinity at the top and bottom of the Arbuckle Group at the injection well site (KGS 1-28).

	Top of Arbuckle (4,168 ft)	Bottom of Arbuckle (5,160 ft)
Temperature (°F)	115	130
Pressure (psi)	1,705	2,188
Chloride (mg/l)	25,765	125,858

Data Acquisition

An extensive suite of geophysical logs were obtained from two 5,000+ ft wells drilled to understand the geology/hydrogeology and to derive petrophysical properties. The purpose of each log and how the data were used to characterize the formation is presented below.

Array Compensated True Resistivity (ACTR)

CTR involves obtaining multiple measurements of resistivity, which reflect conditions at different distances beyond the borehole wall so that the effects of drilling-mud invasion can be factored out for a reading of the true resistivity of the formation. The log data are used for evaluation of (1) formation water salinity variations and (2) the subdivision of pore volume between electrically connected and unconnected porosity, which has important implications regarding permeability, particularly in the injection zone.

Temperature

Temperature logs from surface to injection zone are used to specify temperature-dependent formation properties (formation brine resistivity, solubility, and phase behavior of CO₂) in the numerical model.

Compensated Spectral Natural Gamma Ray

The Compensated Spectral Natural Gamma Ray (CSNGR) log provides insight into the mineral composition of the formations. Measurement of natural gamma-radiation of formations, partitioned among the three most common components of naturally occurring radiation in sandstones and shales (potassium, thorium, and uranium), is used for (1) correlation between wells, so that laterally continuous zones can be identified; (2) shale evaluation, which is particularly important in the evaluation of sealing intervals and baffles; and (3) the recognition of “hot” uranium zones, generally resulting from diagenesis and sometimes indicative of fractures.

Microlog

The microlog records normal and lateral microresistivity at a much higher vertical resolution than standard resistivity logs but has less depth of investigation. The data are used to (1) characterize resistivity of thin zones and (2) provide an indication of mudcake buildup as a good diagnostic of permeable zones.

Spectral Density Dual Spaced Neutron Log

This porosity logging suite can be integrated with magnetic resonance imaging (MRI) and neutron-density crossplot (PHND) porosity logs for high-grade interpretation of porosity. The photoelectric index (Pe) accompanies modern density logging tools and records the absorption of low-energy gamma rays by the formation in units of barns per electron. Logged value is a direct function of the aggregate atomic number (Z) of the elements in the formation and so is a sensitive indicator of mineralogy. Pe is combined with neutron porosity and bulk density information to conduct a Rhomaa-Umma analysis.

Extended Range Micro Imager Correlation (ERMIC) Plot

The high resolution electrical image of borehole wall provided by the ERMIC plot is used for recognition and orientation analysis of (1) fractures, both natural and drilling-induced; (2) vuggy porosity; and (3) shaley zones. A consistency is typically noted between the observations from ERMIC, core, and MRI. This correlation can be used to extend the delineation of major pore types in the intervals that are not cored.

Magnetic Resonance Image (MRI)

The MRI log measures the relaxation time of hydrogen within the pores exposed to a magnetic field whose spectrum reflects the distribution of pore sizes. The MRI data can be used to obtain a distribution of the pore size and an estimate permeability and porosity values by calibrating to core measurements. The MRI log is also used to determine the sealing potential of caprock by deriving CO₂ entry pressure estimates in the confining zone.

Radial Cement Bond Log (RCBL)

The RCBL tool captures downhole data to ensure reliable cement bond evaluation. The tool is equipped with one omni-directional transmitter and two omni-directional receivers, as well as eight radial receivers for comprehensive borehole coverage. An inspection of the log will assist in ensuring that there is a competent cement bond in the well and the absence of any vertical channels through which pressurized fluids could migrate upward into USDWs.

Helical Computerized Tomography (CT) Scan

CT scans are used to evaluate the texture of the rocks and to inspect for the presence of very minute fractures in the confining zone.

Sonic Log

The acoustic measurement of porosity records the first arrival of ultrasonic compressional waves and is primarily sensitive to interparticle porosity—often referred to as “primary” or “matrix porosity”—that occurs between grains or crystals within carbonates. In contrast, the MRI, neutron, and density measurements respond to pore spaces at all scales and so provide a measure of total porosity. The difference between acoustic porosity and total porosity is termed “secondary porosity,” which can be interpreted to be vuggy porosity, where vugs can range in size anywhere from a dissolved grain to large cavities. The overlay of the MRI porosity with the acoustic (sonic)

porosity will typically suggest “vuggy facies” in the carbonate injection zone and tighter (less complex) “matrix facies” in the baffle zones (if present) within the carbonate injection zone.

Geochemical Logs

Geochemical logs are used to characterize elemental composition and mineralogy and assist in evaluating reaction rates in the presence of free phase CO₂. The geochemical data also can be used in conjunction with Schlumberger’s Techlog software to estimate hydrogeologic properties such as porosity.

Core Samples

Core samples were obtained at KGS 1-32 within a 1,600 feet interval spanning from the bottom of the Arbuckle into the Cherokee Shale above the Mississippian System. The samples were used for thin-section spectroscopy, geochemical analyses, lab-based derivation of permeability and porosity estimates, and fracture investigations.

Drill Stem Test (DST) and Other Well Tests

The purpose of conducting DSTs is to obtain the ambient pressures, obtain geochemical samples, and derive estimates of formation permeability. These tests assist in obtaining permeability estimates in the injection zone and can be used to supplement the permeability estimates derived from DSTs. The analysis is discussed in Appendix B.

Geochemical Data

Formation waters were collected during DSTs and swab sampling. The samples were analyzed to establish baseline geochemical conditions and salinity distribution throughout the Arbuckle injection zone. Various geochemical studies were conducted to validate the geologic characterization derived from core and log studies.

The ion composition analyses indicate that the Arbuckle Group is indeed highly stratified with high permeability zones in the top and bottom of this system. The data also indicate that there is sharp hydraulic separation between the Arbuckle Group and the Mississippian system, suggesting the presence of a competent caprock. The biomass concentrations and microbial counts also indicate the presence of a highly stratified Arbuckle reservoir.

Oxygen and hydrogen isotope analyses were conducted to obtain an understanding of the hydrodynamics of the Arbuckle system. The data suggest that the brines from the lower Arbuckle cluster tightly together and have values distinct from the upper Arbuckle. The upper Arbuckle brines have distinctly different δD and $\delta^{18}O$ values than in the lower Arbuckle. This is in conformity with observations and conclusions from core, well logs, ion composition, and biochemistry data discussed above.

Reservoir Characterization

Porosity estimations

The Arbuckle is a triple-porosity system of interparticle, fracture, and vuggy pores. Typically, fracture porosity in carbonates is small in volume (1 to 2%) and so difficult to discriminate, as

contrasted with vuggy porosity, whose evaluation shows distinctive differences between core and logs. In zones with minimal vuggy porosity, there is good agreement between core and logged porosity. In sections with significant vuggy porosity, MRI-based effective porosity is usually greater than core porosity. A good example is shown in the section between 4,900 and 5,150 ft (1494 and 1570 m) depth that contains the injection zone interval (see fig. 22). This figure demonstrates that the most reliable estimator of effective porosity that includes both interparticle and vuggy porosity is the MRI log.

In vuggy zones, core porosity measurements are biased toward low values. Further evidence of the ability of the MRI log to discriminate vugs is provided by fig. 23, where the degree of vugginess observed from core examination of the entire Arbuckle is matched with “megaporosity” from the MRI log as the summed porosities with T2 relaxation times of greater than one second. In conclusion, effective porosity from the MRI log was used as the porosity deliverable to other evaluation modules.

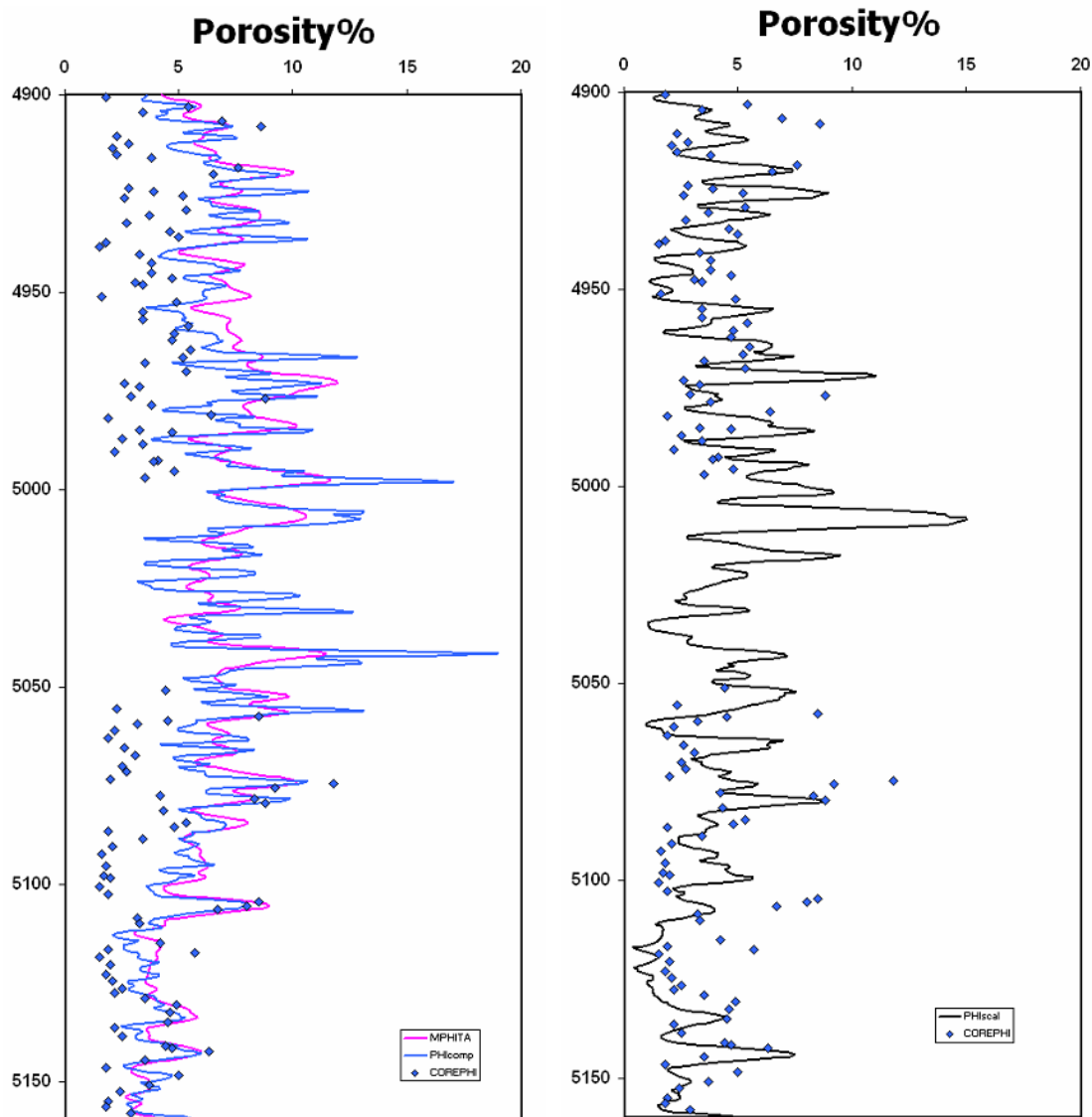


Figure 22. Wellington KGS 1-32 injection zone interval: overlay of MRI effective porosity and neutron-density porosity curves with core porosity measurements (left) and overlay of sonic (acoustic) porosity curve with core measurements (right).

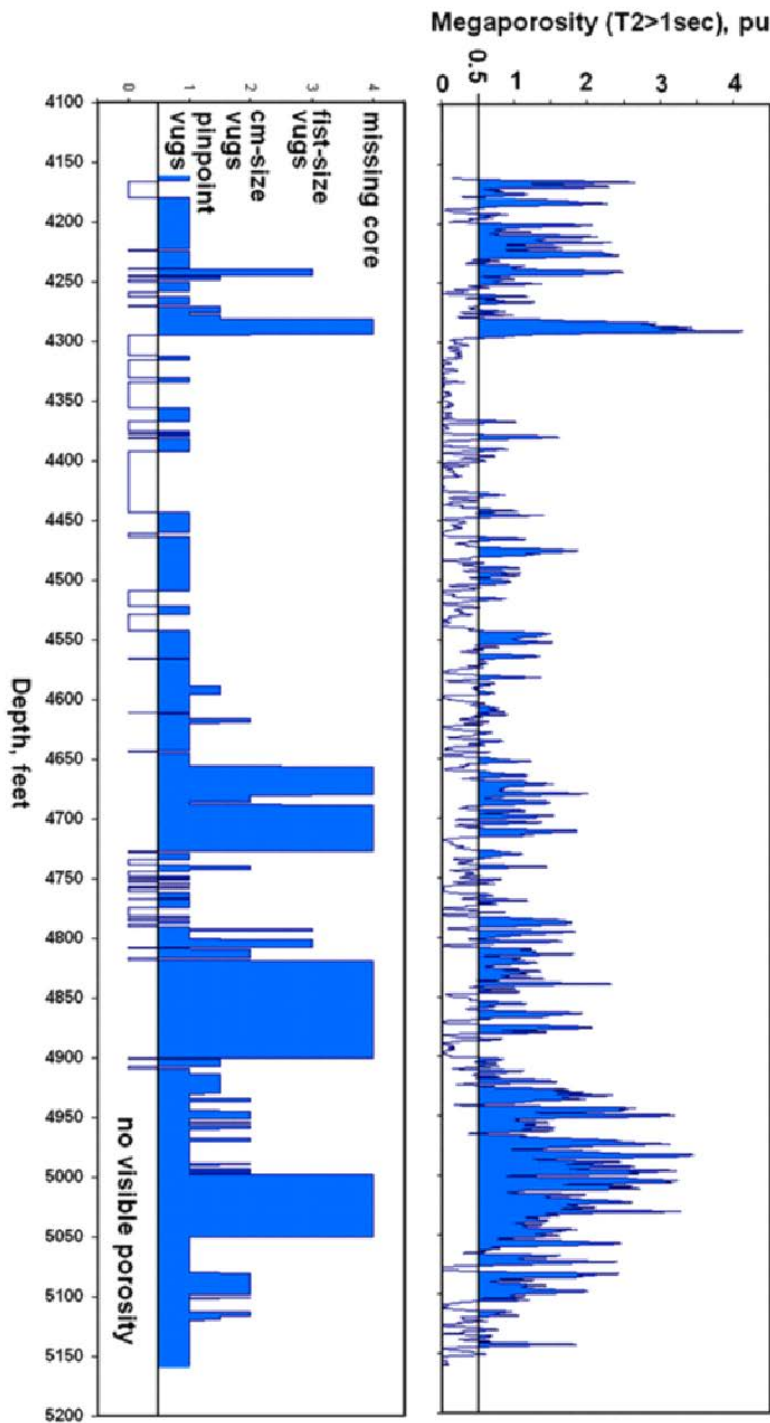


Figure 23. Visual observation of vugs from core in the Arbuckle of Wellington KGS 1-32 (left) compared with summed porosities of the MRI log with T2 relaxation times greater than one second (right).

The total porosity corresponds to the porosity measured by the MRI. This is subdivided between "fast porosity," which approximately matches the core porosity (labeled as PHI_{ip} , for interparticle or matrix porosity), and "slow porosity," considered to represent vugs (the sum of both PHI_{vugc} and $\text{PHI}_{\text{vugnc}}$). In a separate calculation, the MRI porosity was subdivided between connected and non-connected porosity in the electrical sense, based on the resistivity log. By incorporating the resistivity result, the vuggy porosity seen by the MRI is partitioned between non-connected vugs ($\text{PHI}_{\text{vugnc}}$) and connected vugs (PHI_{vugc}). It is tempting to make a hydraulic interpretation of this electrical result in thinking of the connected vugs as perhaps solution-enlarged fractures and the non-connected vugs as isolated vugs that do not contribute to flow. More detailed explanation of methods and discussion of results of log analyses and porosity estimations are presented in Appendix C.

Permeability estimations

It was decided to calculate permeability by relating core-based Flow Zone Indicator (FZI) to the function $1/(\text{Swir} \cdot \Phi)$ using the technique suggested by Fazelalavi and others (2013, attached). Swir refers to the irreducible water saturation and Φ refers to the formation porosity.

Pore structure in the Arbuckle is very complex and there are many variations in pore size distribution (unimodal, bimodal and trimodal) versus depth in very short intervals. Due to this complexity and non-homogeneity in pore size distribution, the Arbuckle permeability was calculated based on pore size classification (micro, meso, and mega pores). FZI in each pore size class was correlated to $1/(\text{Swir} \cdot \Phi)$ of the same class.

Permeability was calculated based on correlations between FZI from core and $1/(\text{Swir} \cdot \phi)$ from log. FZI from core data was calculated using K90 permeability, and $1/(\text{swir} \cdot \phi)$ was calculated using effective porosity and irreducible water saturation from the NMR log. FZI and $1/(\text{swir} \cdot \phi)$ values were sorted from low to high. All FZI values less than 2 and $1/(\text{swir} \cdot \phi)$ values less than 48 were assigned for micro pore sizes, which correspond to permeability values less 0.5 milliDarcy (mD). FZI from 2 to 11 and $1/(\text{swir} \cdot \phi)$ from 48 to 106 were considered for meso pore sizes, which correspond to permeability from about 0.5 to 25 mD, and FZI from 11 to 150 and $1/(\text{swir} \cdot \phi)$ from 106 to 851 were considered for mega pore sizes, which correspond to permeability greater than 25 mD.

The calculated permeability is plotted versus depth in fig. 24, where calculated permeability values are compared with core permeability. Figure 24 is an example of derived permeability for the Arbuckle reservoir; a full account of permeability estimations for the entire Arbuckle interval is presented in Appendix D. Calculated micro pore permeability is shown by brown dots in this plot, meso pore permeability values are shown in green, and mega pore permeability values are shown in blue. Series 1 in the figure represents the continuous distribution of permeability derived by the methods above. A fairly good match between the calculated and core permeabilities can be inferred from the figure.

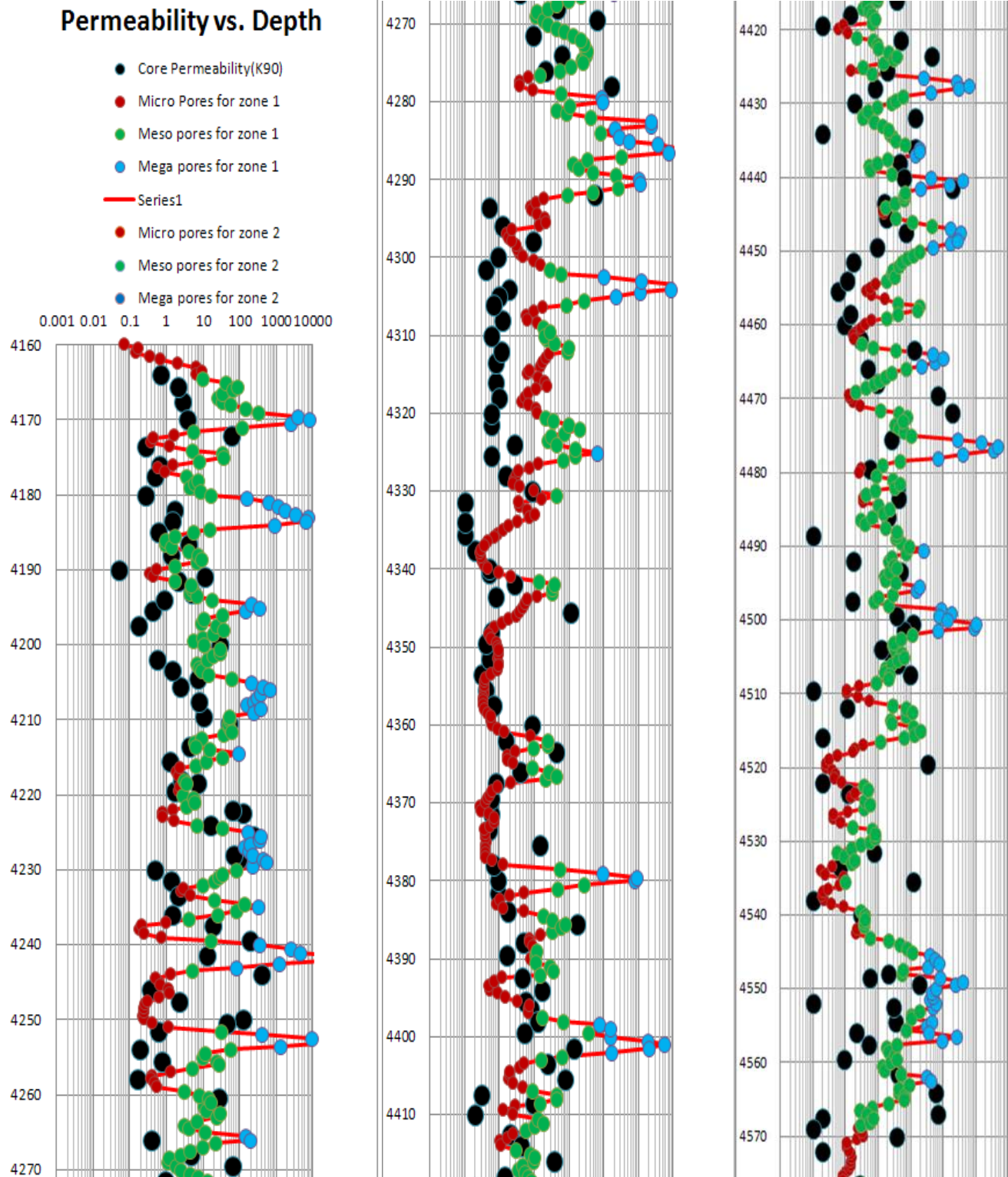


Figure 24. Comparison of core and estimated permeabilities.

Characterization of Confining Zone

The Chattanooga Shale was expected to provide much more confinement than the Simpson Group underneath it. The maximum entry pressure in the Chattanooga Shale at KGS 1-28 is 11,840 psi in the mercury-air system and 956 psi in the CO₂-brine system. As discussed in the modeling section, the maximum induced CO₂ pressure at the top of the Arbuckle/base of the Simpson Shale is approximately 13 psi. Therefore, the primary confining zone was expected to confine the injected CO₂ in the Arbuckle aquifer.

Estimating Structural Leakage Potential

South-central Kansas, although historically stable, has experienced an increase in seismic activity since 2013. The correlation with brine disposal operations has renewed interest in the role of fluids in fault reactivation, specifically in the crystalline basement, where the majority of events have occurred. This study focuses on determining the suitability of CO₂ and brine injection into a Cambrian-Ordovician reservoir (Arbuckle Group) for long-term storage and a shallower Mississippian reservoir for enhanced oil recovery (EOR) in Wellington Field, Sumner County, Kansas. Our approach for determining the potential for injection-induced seismicity has been to (1) map subsurface faults and estimate in-situ stresses, (2) perform slip and dilation tendency analysis to identify optimally oriented faults relative to the estimated stress field, and (3) determine the pressure changes required to induce slip, both at reservoir depth and basement depth. Through the use of 3-D seismic reflection data, 12 near-vertical faults were identified with fault planes striking between 325° and 049° and the majority oriented NNE, consistent with nodal planes from moment tensor solutions from recent earthquakes in Kansas and Oklahoma. Fault lengths range from 210 to 4,450+ m and vertical separations range from 12 to 33 m. The majority of faults cut through both reservoirs, with a number that clearly cut the top basement reflector. Drilling-induced tensile fractures (N=40) identified from image logs and inversion of moment tensor solutions (N=70) are consistent with the maximum horizontal stress (SHmax) oriented ~EW. Stress magnitudes were estimated using step rate tests (Shmin = 18.4 MPa), density logs (Sv = 36.6 MPa), and calculations from wells with drilling-induced tensile fractures (SHmax = 31.3–45.9 MPa) at the gauge depth of 1,484m (Fig. 25). Slip and dilation tendency analysis indicates that faults striking < 020° are stable under reservoir conditions, whereas faults striking 020°–049° may have a moderate to high risk for reactivation with increasing pore fluid pressure. These faults would require a pore fluid pressure increase of at least 1.1 MPa to 7.6 MPa at 1,117 m (Mississippian) and 1.31 MPa to 9.8 MPa at 1,484 m (Arbuckle) to reach failure. Given the proposed injection volume, it is unlikely that faults will be reactivated at reservoir depths. However, at basement depths, high-rate injection operations could reach pressures beyond the critical threshold for slip, as demonstrated by the large number of injection-induced earthquakes west of the study area.

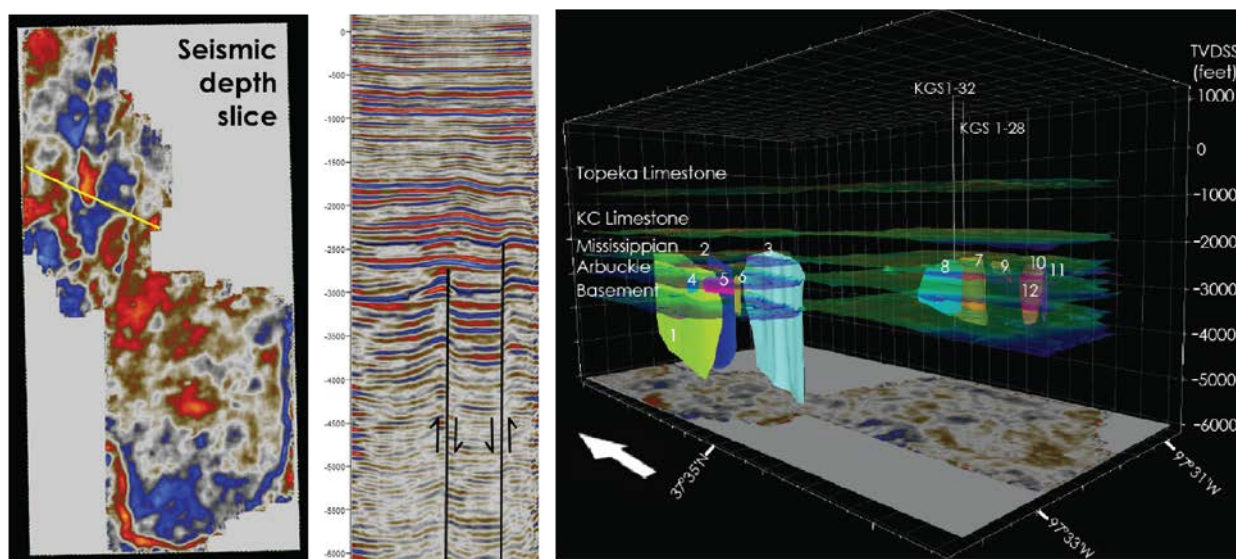


Figure 25. Map view of fault locations and seismic profile cross-section (left) and 3-D view of mapped fault (right).

Geochemistry-Based Evidence of Competent Upper Confining Zone

Geochemical logs and thin sections were analyzed for mineralogy and soil characterization to enable reaction kinetics modeling and determining potential for plugging pore space due to mineral precipitation

Ion Composition

Because of their conservative nature, bromine and chlorine are especially useful in differentiating salinity sources and establishing the basis of brine mixture in the subsurface (Whittemore, 1995). Bromine, chlorine, and sulfate concentrations of brine from nine depths in the Arbuckle and three depths in the Mississippian formations were evaluated. The Br-/Cl- and $\text{SO}_4^{2-}/\text{Cl-}$ weight ratios versus chloride concentration for the Arbuckle saline aquifer and Mississippian reservoir at Wellington are presented in fig. 26, from which it is clear that the geochemical composition of the Mississippian waters is markedly different from that of the Arbuckle. The salinity within the Mississippian varies between 120,000 mg/l and 135,000 mg/l versus 30,500 mg/l in the underlying upper Arbuckle. Similarly, the $\text{SO}_4^{2-}/\text{Cl-}$ ratio of approximately 0.002 in the Mississippian formation is significantly different from the range of this ratio of 0.002–0.0055 in the upper Arbuckle. Collectively, the chloride and $\text{SO}_4^{2-}/\text{Cl-}$ data suggest a hydraulic separation between the Mississippian and the Arbuckle systems, which supports the conceptualization of a tight upper confining zone.

Isotopic Characterization

Oxygen and hydrogen isotope distributions present another opportunity to assess hydraulic connectivity between the Arbuckle Group and the Mississippian System. Figure 27 shows the δD vs $\delta^{18}\text{O}$, reported as the difference between the $^{18}\text{O}/^{16}\text{O}$ and $2\text{H}/1\text{H}$ abundance ratios of the samples vs. the Vienna Standard Mean Ocean Water (VSMOW) in per mil notation (‰) for the Arbuckle and Mississippian samples. Best fit regression lines for each formation, compared with the global

meteoric water line (GMWL) and modern seawater is also presented, which suggests different water isotopic composition in the Arbuckle and Mississippian systems.

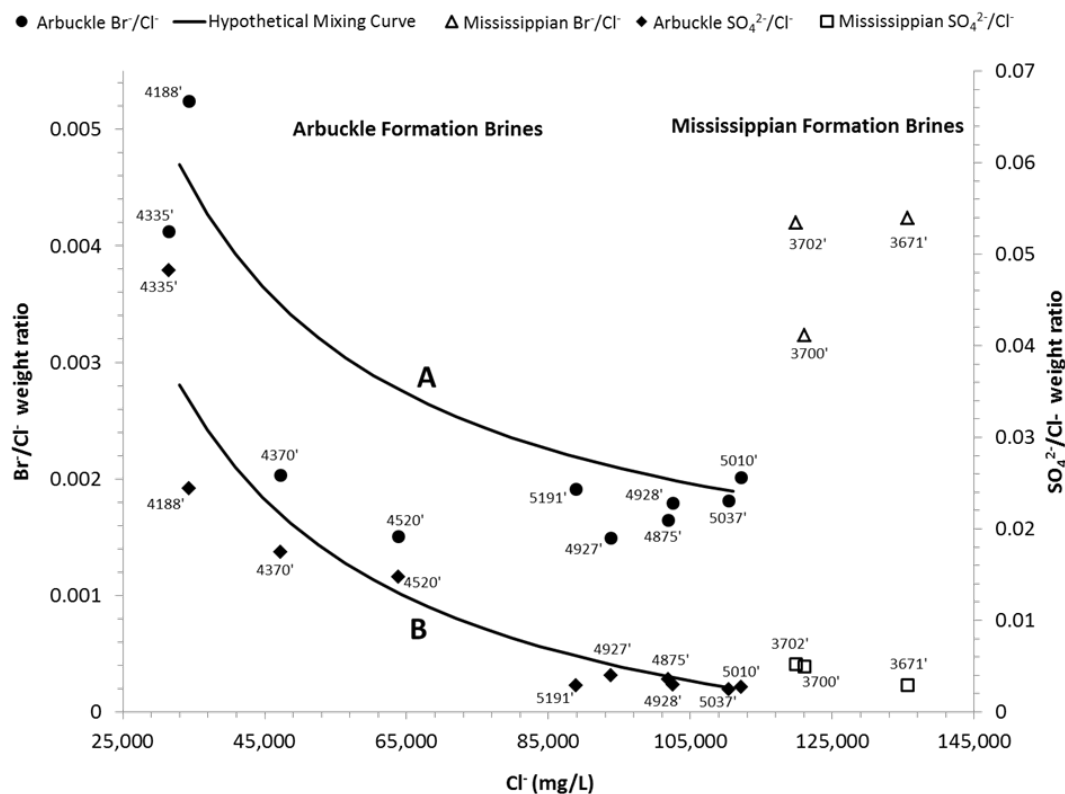


Figure 26. Br^-/Cl^- and $\text{SO}_4^{2-}/\text{Cl}^-$ weight ratios versus chloride concentration for the Arbuckle saline aquifer and Mississippian oil producing brines at Wellington, Kansas. Also shown are the hypothetical mixing curves for Br^-/Cl^- (A) and $\text{SO}_4^{2-}/\text{Cl}^-$ (B) (Scheffer, 2012)

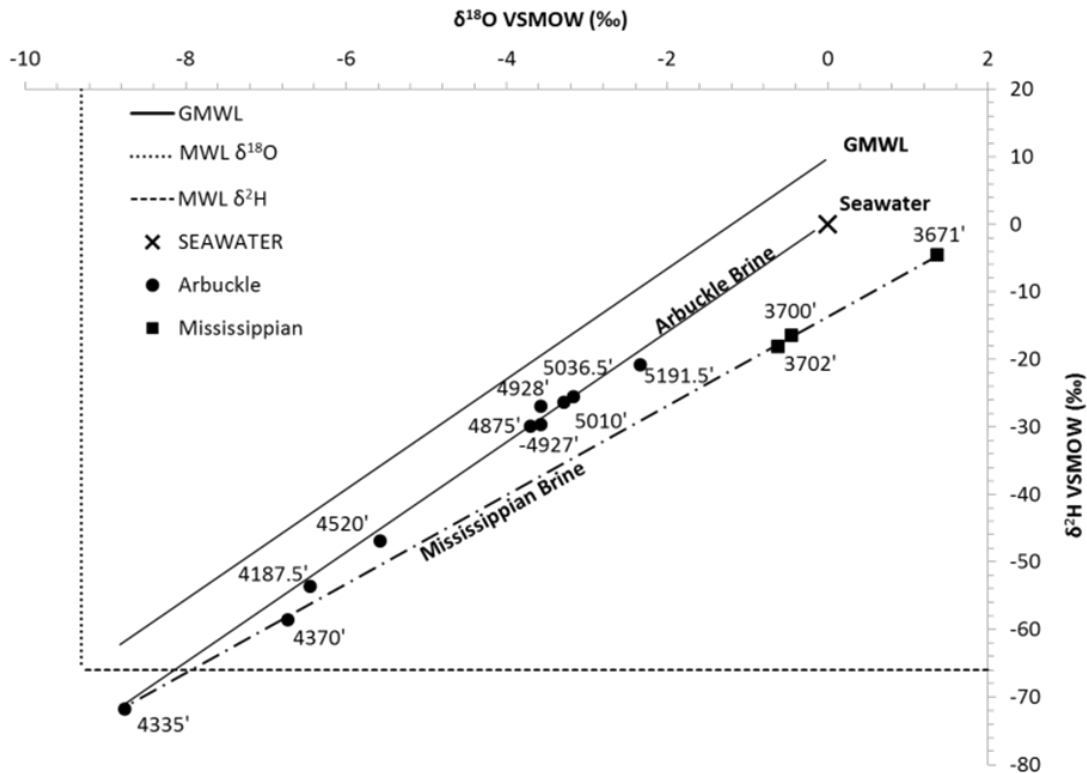


Figure 27. δD vs $\delta^{18}\text{O}$ (‰, VSMOW) for the Arbuckle and Mississippian reservoirs (Scheffer, 2012)

The chloride distribution in the Arbuckle and Mississippian systems at KGS 1-28 and KGS 1-32, obtained from data collected during DST and swabbing, is presented in fig. 28. The chloride gradient in the Arbuckle approximates a linear trend with chloride concentration increasing from approximately 30,500 mg/l in the Upper Arbuckle to as much as 118,000 mg/l in the injection zone. Chloride concentration in the Mississippian formation at 119,000 mg/l is substantially higher than in the upper Arbuckle. The large difference in chloride concentrations between the Mississippian and upper Arbuckle supports the conceptualization that the confining zone separating the Arbuckle aquifer from the Mississippian reservoir is tight and that there are no conductive faults in the vicinity of the Wellington site that hydraulically link the two systems.

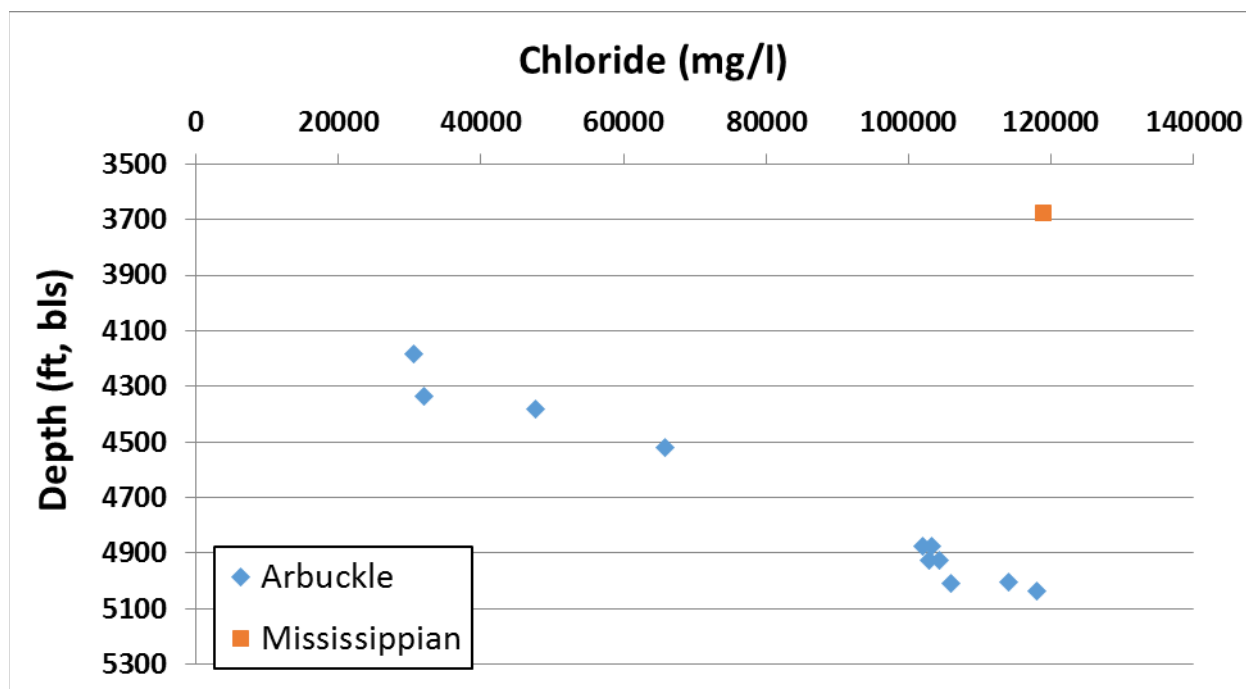


Figure 28. Chloride distribution within the Arbuckle aquifer and Mississippian reservoir at KGS 1-28 and KGS 1-32.

Ca/Sr molar ratios plotted against Ca/Mg molar ratios of Arbuckle data (fig. 29) with trends for dolomitization and calcite recrystallization as described in McIntosh (2004). This plot clearly shows two groupings within the Arbuckle samples. The upper Arbuckle shows a calcite recrystallization signature while the lower Arbuckle shows the influence of dolomitization on brine chemistry. This presents evidence that the upper and lower Arbuckle have different hydrochemical regimes (Barker et al., 2012).

The Br-/Cl- ratio provides further evidence of the separation of the upper and lower high permeability zones in the Arbuckle. As can be inferred from fig. 26, the Br-/Cl- values of the lower Arbuckle varies over a narrow range in the neighborhood of 0.002, while the variation is much larger (between 0.002 and 0.0055) in the upper Arbuckle. A hypothetical Br-/Cl- mixing curve (curve A, fig. 26) was calculated using averaged end-member values from the two deepest samples in the Arbuckle (5,010 ft and 5,036 ft) and the two shallowest samples in the Arbuckle (4,182 ft and 4,335 ft) to examine mixing of reservoir fluids for purposes of evaluating connectivity throughout the reservoir. In the lower Arbuckle samples, Br-/Cl- concentrations remained relatively consistent, but they increased sharply in the upper Arbuckle. This suggests possible different brine origins for the lower and upper regions of the Arbuckle. Regardless of the origin, the data suggest that the brines in the upper and lower Arbuckle are distinctly different and there does not appear to be any mixing between the two zones; supporting the hypothesis of the presence of low permeability baffle zone between the upper Arbuckle and the lower injection interval, which was also inferred from the permeability data.

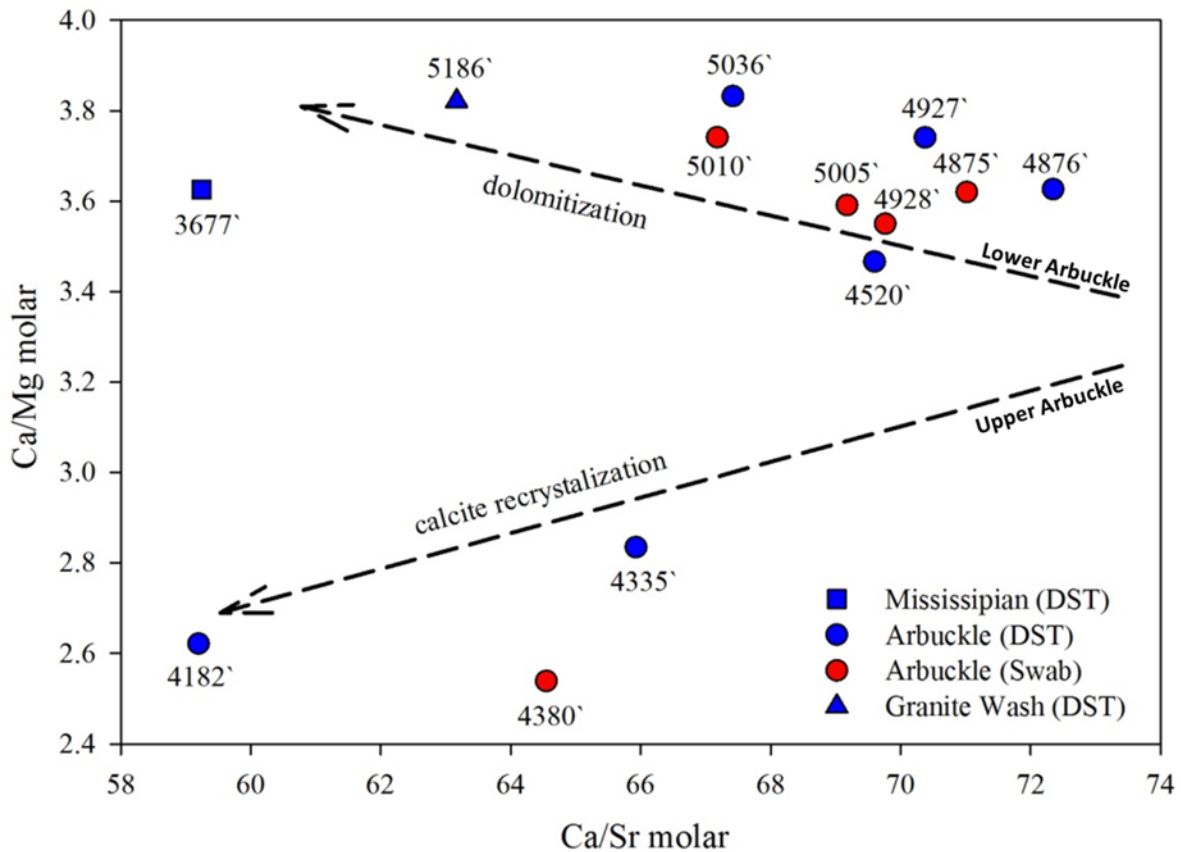


Figure 29. Ca/Sr vs Ca/Mg molar ratios showing trends of dolomitization and calcite recrystallization (from Barker et al., 2012).

Biogeochemistry

The concentration of the redox reactive ions ferrous iron, sulfate, nitrate, and methane (Fe^{2+} , SO_4^{2-} , NO_3^- , CH_4) can be used as evidence of biological activity in the subsurface (Scheffer, 2012). In oxygen-restricted sediments that are rich in organic carbon such as the Arbuckle, stratification would follow the redox ladder with aerobes at shallower depths where oxygen is available, followed by nitrate, iron, and sulfate reducers (in this order), and methanogens at the deepest level based on availability of terminal electron acceptors. Because there is a paucity of oxygen in the Arbuckle, typical stratification of microbial metabolisms would involve dissimilar iron reducing bacteria (DIRB) above sulfate reducing bacteria (SRB) above methanogens. This biogenic stratification would be manifested by a zone with increased reduced iron over decreasing sulfate (or increasing sulfide) over increasing methane. However, as shown in fig. 30, there appears to be two separate trends observed in the Arbuckle aquifer; one trend 4.40, for samples above the suspected baffle (1,277 m to 1,321 m [4,190 ft to 4,334 ft]) in the upper Arbuckle, and one trend below the suspected baffle (1,378 m to 1,582 m [4,521 ft to 5,190 ft]) in the lower Arbuckle. This suggests a reset of the biogeochemistry due to lack of hydraulic communication between the Upper and Lower Arbuckle.

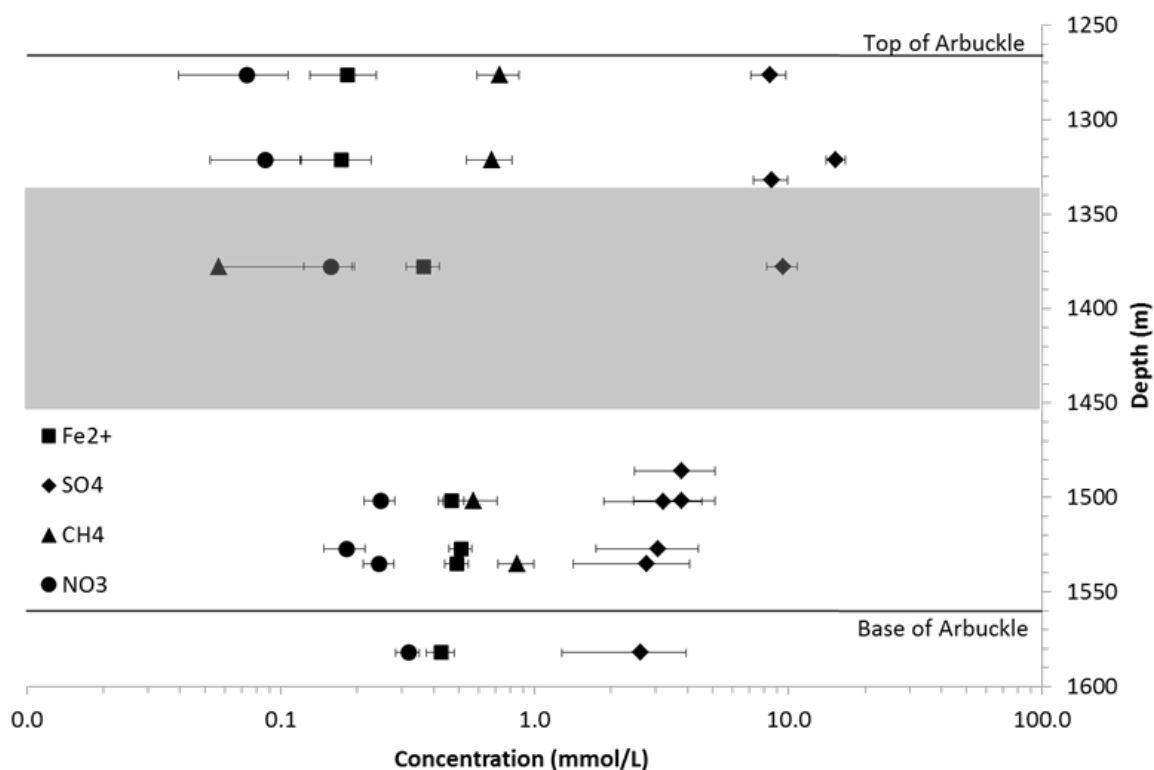


Figure 30. Concentrations of redox reactive ions ferrous iron, sulfate, methane, and nitrate (Fe^{2+} , SO_4^{2-} , CH_4 , NO_3^-) in the Arbuckle reservoir (Scheffer, 2012).

Microbial Diversity

Biomass concentrations of 2.1×10^6 , 1.9×10^7 , and 2.6×10^{-3} cells/ml were determined using the quantitative polymerase chain reaction (qPCR) procedures at depths of 1,277 m (4,190 ft), 1,321 m (4,334 ft), and 1,378 m (4,520 ft), respectively. The lowest biomass coincides with the low permeability baffle zone in the mid-Arbuckle (1,378 m [4,520 ft]). Decreased flow through the baffle zone could decrease nutrient recharge and lead to nutrient depletion (Scheffer, 2012). The highest biomass and most unique sequences occurred in the upper Arbuckle at 1,321 m (4,334 ft) as shown in fig. 31.

The free-living microbial community was also examined in the Arbuckle aquifer. Results show 43% diversity at a depth of 1,276 m (4,190 ft), 62% diversity at 1,321 m (4,334 ft), and 39% diversity at 1,378 m (4,520 ft), which follows the same trend as biomass shown in fig. 31. Notably, the microbial communities from 1,277 m (4,190 ft) and 1,321 m (4,334 ft) are very similar to one another and vary distinctly from the community detected at 1,378 m (4,520 ft). Nine genera of bacteria were detected at 1,276 m (4,190 ft) and 1,321 m (4,334 ft). Seven genera of bacteria were detected at 1,378 m (4,520 ft). *Alkalibacter*, *Bacillus* and *Erysipelthrix* were found at the two shallower depths but not at 1,378 m (4,520 ft). *Dethiobacter* was detected only at the deeper depth of 1,378 m (4,520 ft).

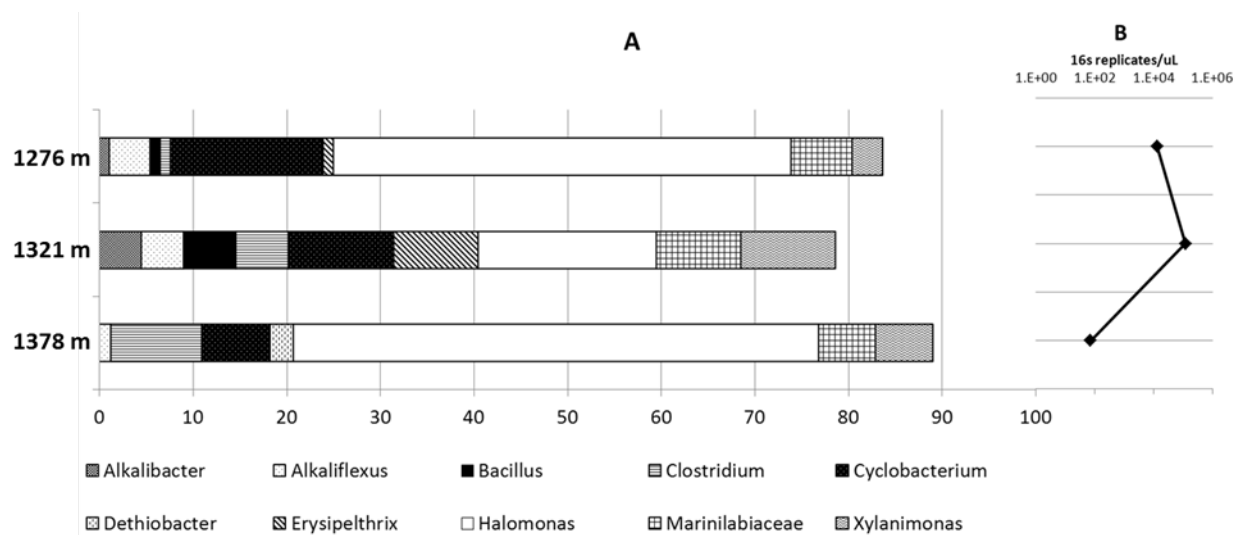


Figure 31. Arbuckle aquifer microbial profile showing the distribution of bacteria in the Arbuckle (A), and the DNA concentration (B) (from Scheffer, 2012).

Conceptual Model and Geologic Models

The simulation model spans the entire thickness of the Arbuckle aquifer. The CO₂ was to be injected in the lower portion of the Arbuckle in the interval 4,910–5,050 feet, which has relatively high permeability based on the core data collected at the site. Preliminary simulations indicated that the bulk of the CO₂ would remain confined in the lower portions of the Arbuckle because of the low permeability intervals in the baffle zones and also shown in analysis of geologic logs at wells KGS 1-28 and KGS 1-32. Therefore, no-flow boundary conditions were specified along the top of the Arbuckle. The specification of a no-flow boundary at the top is also in agreement with hydrogeologic analyses presented, which indicate that the upper confining zone—comprising the Simpson Group, the Chattanooga Shale, and the Pierson formation—has very low permeability, which should impede any vertical movement of groundwater from the Arbuckle Group. Evidence for sealing integrity of the confining zone and absence of transmissive faults include the following:

- 1) under-pressured Mississippian group of formations relative to pressure gradient in the Arbuckle,
- 2) elevated chlorides in Mississippian group of formations relative to brine recovered at the top of the Arbuckle,
- 3) geochemical evidence for stratification of the Arbuckle aquifer system and presence of a competent upper confining zone.

Additionally, entry pressure analyses indicate that an increase in pore pressure of more than 956 psi within the confining zone at the injection well site is required for the CO₂-brine to penetrate through the confining zone. As discussed in the model simulation results section below, the maximum increase in pore pressure at the top of the Arbuckle is less than 1.5 psi under the worst-case scenario. This small pressure rise at the top of the Arbuckle is due to CO₂ injection below the lower vertical-permeability baffle zones present in the middle of the Arbuckle Group, which confines the CO₂ in the injection interval in the lower portions of the Arbuckle Group. The confining zone is also documented to be locally free of transmissive fractures based on fracture

analysis conducted at KGS 1-28 (injection well). There are no known transmissive faults in the area. It should be noted that an Operation Plan for Safe and Efficient Injection has been submitted to the EPA, which has a provision for immediate cessation of injection should an anomalous pressure drop be detected owing to development or opening of fractures.

Based on the above evidence, it is technically appropriate to restrict the simulation region within the Arbuckle Group for purposes of numerical efficiency, without compromising predictions of the effects of injection on the plume or pressure fronts. Because of the presence of the Precambrian granitic basement under the Arbuckle Group, which is expected to provide hydraulic confinement, the bottom of the model domain was also specified as a no-flow boundary. Active, real-time pressure and temperature monitoring of the injection zone at the injection and monitoring wells will likely be able to detect any significant movement of CO₂ out of the injection zone along fractures. Also, the 18-seismometer array provided by Incorporated Research Institutions for Seismology (IRIS) will detect small seismicity and their hypocenters within several hundred feet resolution to provide additional means to monitor the unlikely movement of CO₂ above or below the Arbuckle injection zone.

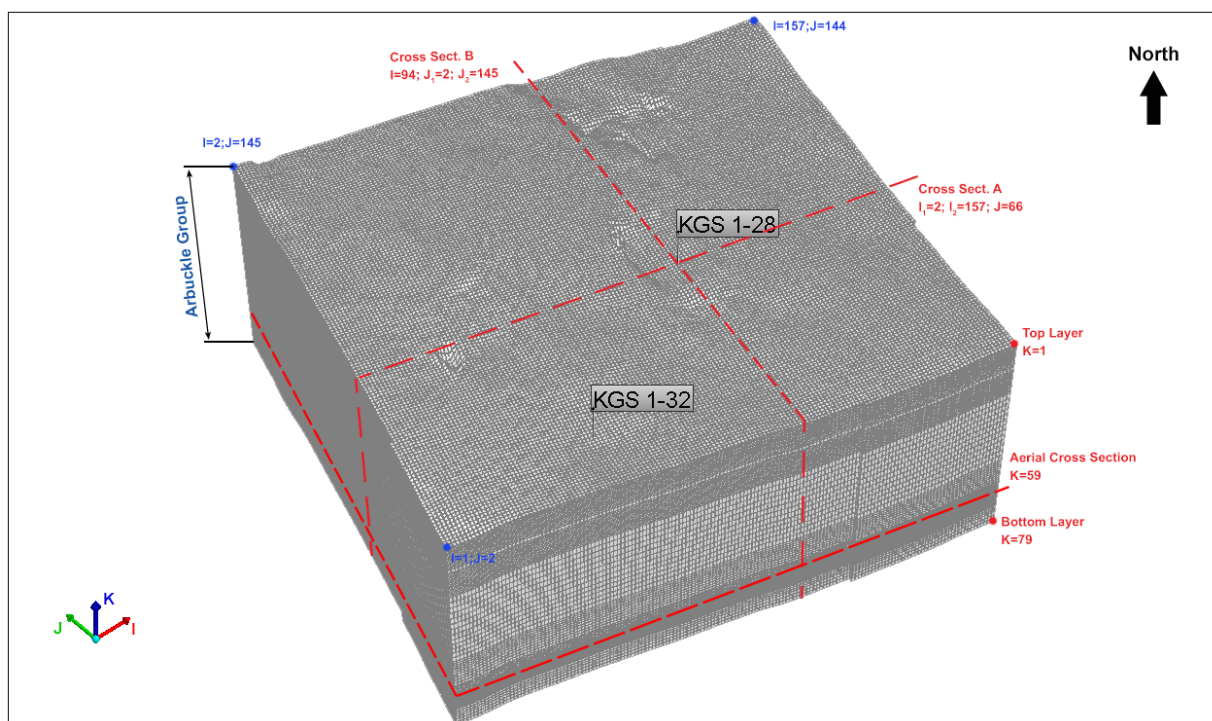


Figure 32a. Model mesh in 3-D showing location of Arbuckle injection (KGS 1-28) and monitoring (KGS 1-32) wells along with the east-west and north-south cross sections.

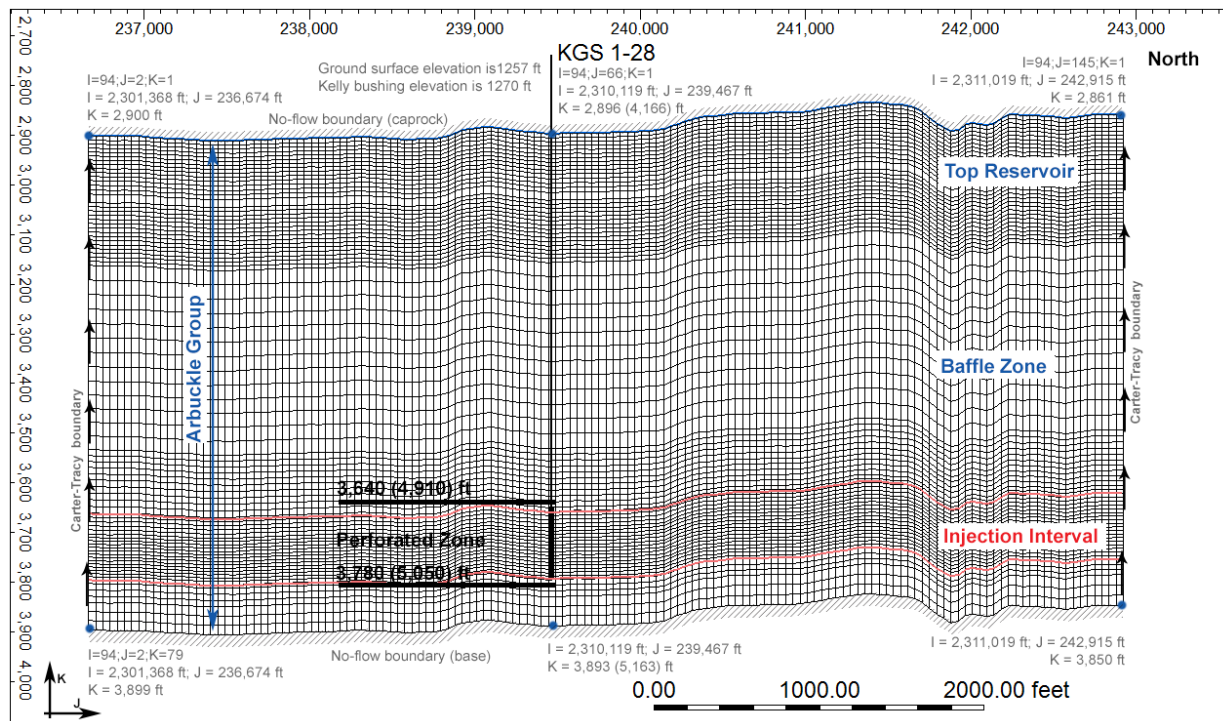
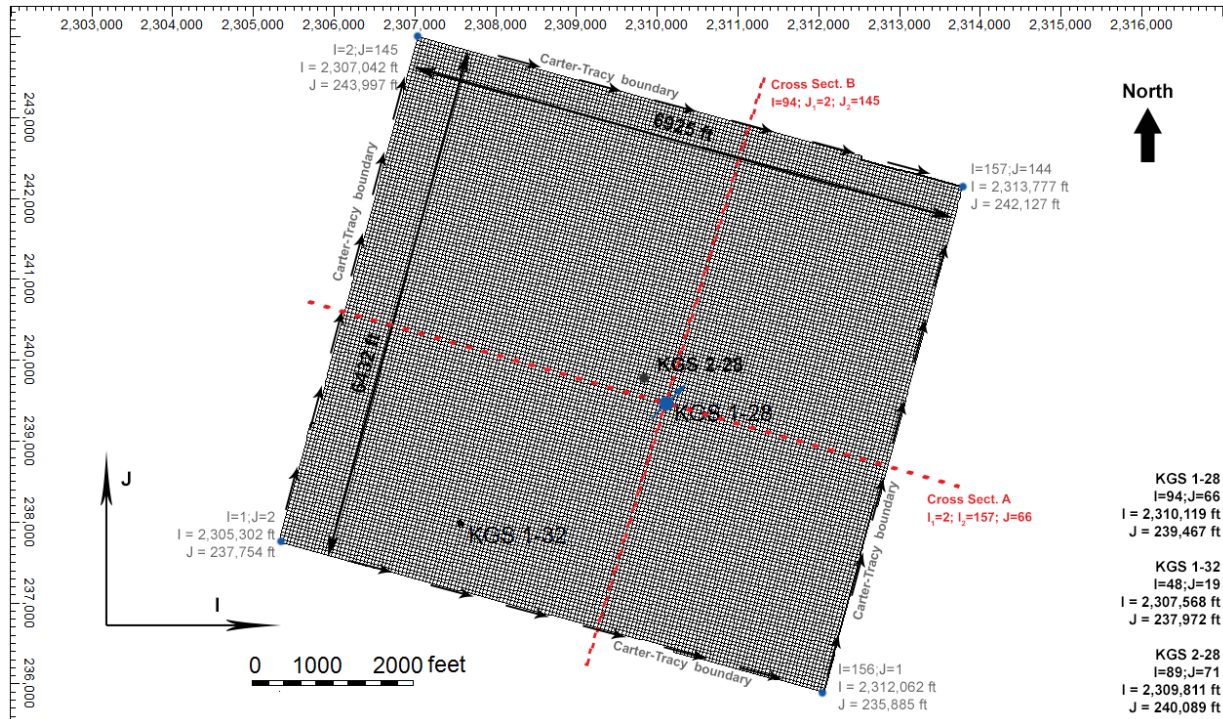


Figure 32b. North-south cross section of model grid along column 94 showing boundary conditions. Y-axis upper figure: vertical depth without kelly bushing (ft). X-axis upper figure: Global coordinates, latitude (ft). Y-axis lower figure: Global coordinates, longitude (ft). X-axis lower figure: Global coordinates, longitude (ft).

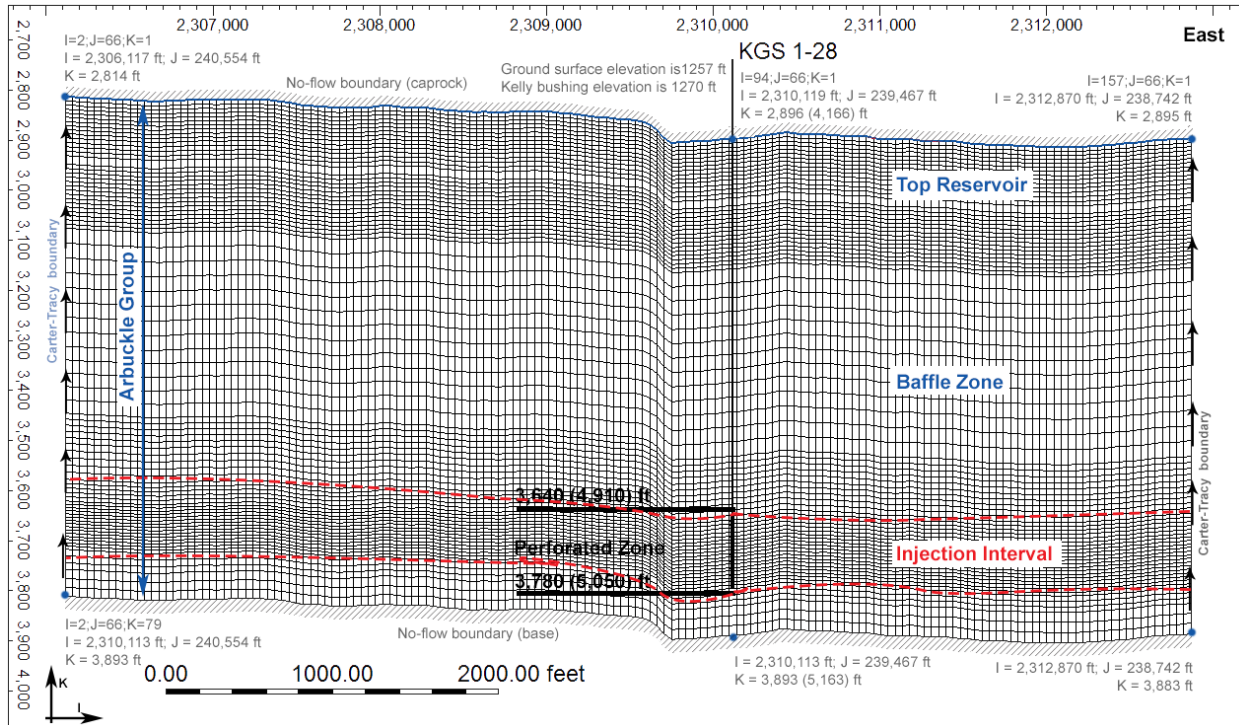


Figure 32c. East-west cross section of model grid along row 66 showing boundary conditions. Y axis: Vertical depth without kelly bushing (ft). X-axis: Global coordinates, longitude (ft).

Modeled Processes

Physical processes modeled in the reservoir simulations included isothermal multi-phase flow and transport of brine and CO₂. Isothermal conditions were modeled because the total variation in subsurface temperature in the Arbuckle Group from the top to the base is only slightly more than 10°F (which should not significantly affect the various storage modes away from the injection well) and because it is assumed that the temperature of the injected CO₂ will equilibrate to formation temperatures close to the well. Also, non-isothermal sensitivity simulations were conducted for the EPA in which it was demonstrated that including temperature as a variable affects the plume extent and the pressure distribution only minimally. Uniform salinity concentration was assumed as the effects of water salinity on the simulated AoR were found to be negligible (less than 0.5%).

Subsurface storage of CO₂ occurs via the following four main mechanisms:

- structural trapping,
- aqueous dissolution,
- hydraulic trapping, and

- mineralization.

The first three mechanisms were simulated in the Wellington model. Mineralization was not simulated as geochemical modeling indicated that due to the short-term and small-scale nature of the pilot project, mineral precipitation is not expected to cause any problems with clogging of pore space that may reduce permeability and negatively affect injectivity. Therefore, any mineral storage that may occur will only result in faster stabilization of the CO₂ plume and make projections presented in this model somewhat more conservative with respect to the extent of plume migration and CO₂ concentrations.

Model Operational Constraints

The bottomhole injection pressure in the Arbuckle should not exceed 90% of the estimated fracture gradient of 0.75 psi/ft (measured from land surface). Therefore, the maximum induced pressure at the top and bottom of the Arbuckle Group should be less than 2,813 and 3,483 psi, respectively, as specified in table 3. At the top of the perforations (4,910 ft), pressure would not exceed 2,563 psi.

Table 3. Maximum allowable pressure at the top and bottom of the Arbuckle Group based on 90% fracture gradient of 0.675 psi/ft.

Depth (feet, bls)	Maximum Pore Pressure (psi)
4,166 (Top of Arbuckle)	2,813
4,910 (Top of Perforation)	3,314
5,050 (Bottom of Perforation)	3,408
5,163 (Bottom of Arbuckle)	3,483

Geostatistical Reservoir Characterization of Arbuckle Group

Statistical reservoir geomodeling software packages have been used in the oil and gas industry for decades. The motivation for developing reservoir models was to provide a tool for better reconciliation and use of available hard and soft data (fig. 33). Benefits of such numerical models include 1) transfer of data between disciplines, 2) a tool to focus attention on critical unknowns, and 3) a 3-D visualization tool to present spatial variations to optimize reservoir development. Other reasons for creating high-resolution geologic models include the following:

- volumetric estimates;
- multiple realizations that allow unbiased evaluation of uncertainties before finalizing a drilling program;
- lateral and top seal analyses;
- integration (i.e., by gridding) of 3-D seismic surveys and their derived attributes assessments of 3-D connectivity;
- flow-simulation-based production forecasting using different well designs;

- optimizing long-term development strategies to maximize return on investment.

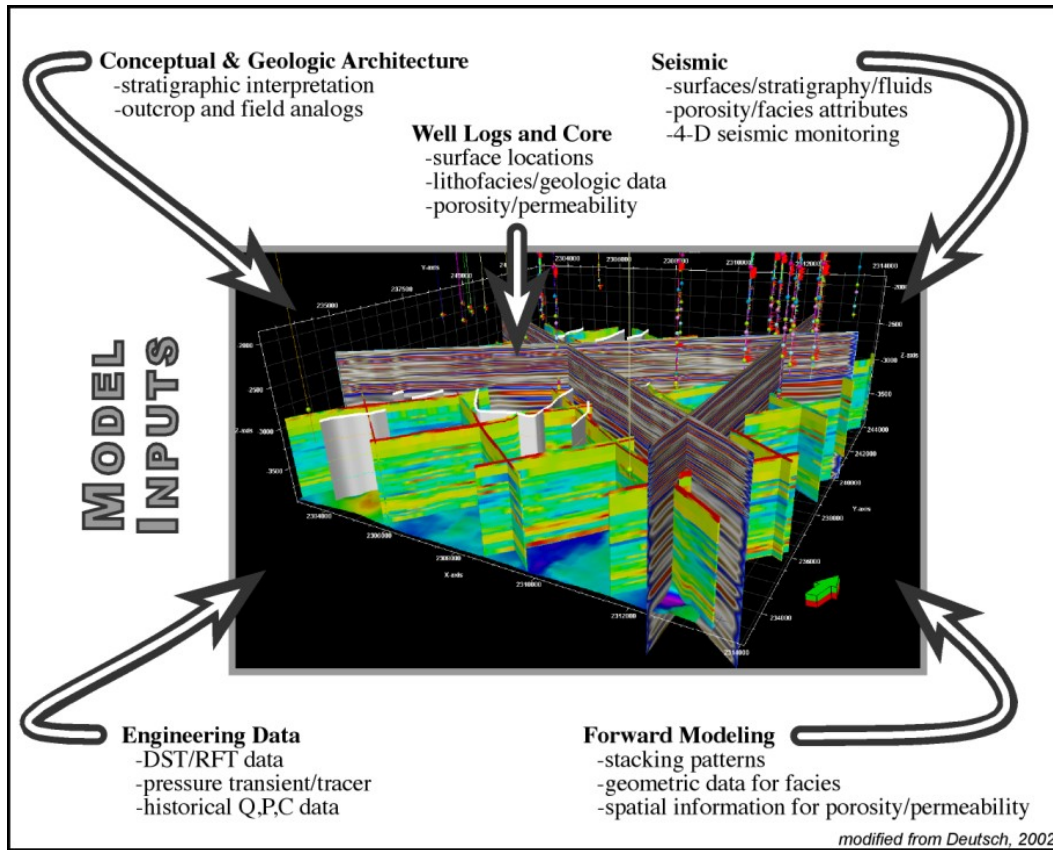


Figure 33. A static, geocellular reservoir model showing the categories of data that can be incorporated (modified from Deutsch, 2002).

Although geocellular modeling software has largely flourished in the energy industry, its utility can be important for reservoir characterization in CO₂ research and geologic storage projects, such as the Wellington Field. The objective in the Wellington project is to integrate various data sets of different scales into a cohesive model of key petrophysical properties, especially porosity and permeability. The general steps for applying this technology are to model the large-scale features followed by modeling progressively smaller, more uncertain, features. The first step applied at the Wellington Field was to establish a conceptual depositional model and its characteristic stratigraphic layering. The stratigraphic architecture provided a first-order constraint on the spatial continuity of facies, porosity, permeability, saturations, and other attributes within each layer. Next, facies (i.e., rock fabrics) were modeled for each stratigraphic layer using cell-based or object-based techniques. Porosity was modeled by facies and conditioned to “soft” trend data, such as seismic inversion attribute volumes. Likewise, permeability was modeled by facies and collocated, co-kriged to the porosity model.

Geological Model

Lower Arbuckle core from Wellington reveals sub-meter-scale, shallowing-upward peritidal cycles. The two common motifs are cycles passing from basal dolo-mudstones/wackestones into algal dololaminites or matrix-poor monomict breccias. Bioclasts are conspicuously absent. Breccias are clast-supported, monomictic, and angular, and their matrix dominantly consists of cement. They are best classified as crackle to mosaic breccias (Loucks, 1999) because there is little evidence of transportation. Lithofacies and stacking patterns (i.e., sub-meter scale, peritidal cycles) are consistent with an intertidal to supratidal setting. Breccia morphologies, scale (< 0.1 m), mineralogy (e.g., dolomite, anhydrite, length-slow chalcedony), depositional setting, greenhouse climate, and paleo-latitude (~15° S) support mechanical breakdown processes associated with evaporite dissolution. The Arbuckle-Simpson contact (~800 ft above the proposed injection interval) records the super-sequence scale, Sauk-Tipppecanoe unconformity, which records subaerial-related karst landforms across the early Phanerozoic supercontinent Laurentia.

Facies Modeling

The primary depositional lithofacies were documented during core description at KGS 1-32. A key issue was reconciling large variations between permeability measurements derived from wireline logs (i.e., nuclear resonance tool), whole core, and step-rate tests. Poor core recovery from the injection zone resulted from persistent jamming, which is commonly experienced in fractured or vuggy rocks (Figure 34). Image logs acquired over this interval record some intervals with large pores (cm scale) that are likely solution-enlarged vugs (touching-vugs of Lucia, 1999; fig. 35). Touching-vug fabrics commonly form a reservoir-scale, interconnected pore system characterized by Darcy-scale permeability. It is hypothesized that a touching-vug pore system preferentially developed within fracture-dominated crackle and mosaic breccias—formed in response to evaporite removal—which functioned as a strataform conduit for undersaturated meteoric fluids (fig. 36). As such, this high-permeability, interwell-scale, touching-vug pore system is largely strataform and, therefore, predictable.



Figure 34. Example of the carbonate facies and porosity in the injection zone in the lower Arbuckle (part of the Gasconade Dolomite Formation). Upper half is light olive-gray, medium-grained dolomitic packstone with crackle breccia. Scattered subvertical fractures and limited cross stratification. Lower half of interval shown has occasional large vugs that crosscut the core consisting of a light olive-gray dolopackstone that is medium grained. Variable-sized vugs range from cm-size irregular to subhorizontal.

Petrophysical Properties Modeling

The approach taken for modeling a particular reservoir can vary greatly based on available information and often involves a complicated orchestration of well logs, core analysis, seismic surveys, literature, depositional analogs, and statistics. Because well log data were available in only two wells (KGS 1-28 and KGS 1-32) that penetrate the Arbuckle reservoir at the Wellington site, the geologic model also relied on seismic data, SRT, and DST information. Schlumberger's Petrel™ geologic modeling software package was used to produce the current geologic model of the Arbuckle saline aquifer for the pilot project area. This geomodel extends 1.3 mi by 1.2 mi laterally and is approximately 1,000 ft in thickness, spanning the entire Arbuckle Group as well as a portion of the sealing units (Simpson/Chattanooga shale).

4.3 Porosity Modeling

In contrast to well data, seismic data are extensive over the reservoir and are, therefore, of great value for constraining facies and porosity trends within the geomodel. Petrel's volume attribute processing (i.e., genetic inversion) was used to derive a porosity attribute from the prestack depth migration (PSDM) volume to generate the porosity model (fig. 37). The seismic volume was created by re-sampling (using the original exact amplitude values) the PSDM 50 ft above the Arbuckle and 500 ft below the Arbuckle (i.e., approximate basement). The cropped PSDM volume and conditioned porosity logs were used as learning inputs during neural network processing.

A correlation threshold of 0.85 was selected and 10,000 iterations were run to provide

the best correlation. The resulting porosity attribute was then re-sampled, or upscaled (by averaging), into the corresponding 3-D property grid cell.

The porosity model was constructed using SGS. The porosity logs were upscaled using arithmetic averaging. The raw upscaled porosity histogram was used during SGS. The final porosity model was then smoothed. The following parameters were used as inputs:

- I. Variogram
 - a. Type: spherical
 - b. Nugget: 0.001
 - c. Anisotropy range and orientation
 - i. Lateral range (isotropic): 5,000 ft
 - ii. Vertical range: 10 ft
- II. Distribution: actual histogram range (0.06–0.11) from upscaled logs
- III. Co-Kriging
 - a. Secondary 3-D variable: inverted porosity attribute grid
 - b. Correlation coefficient: 0.75

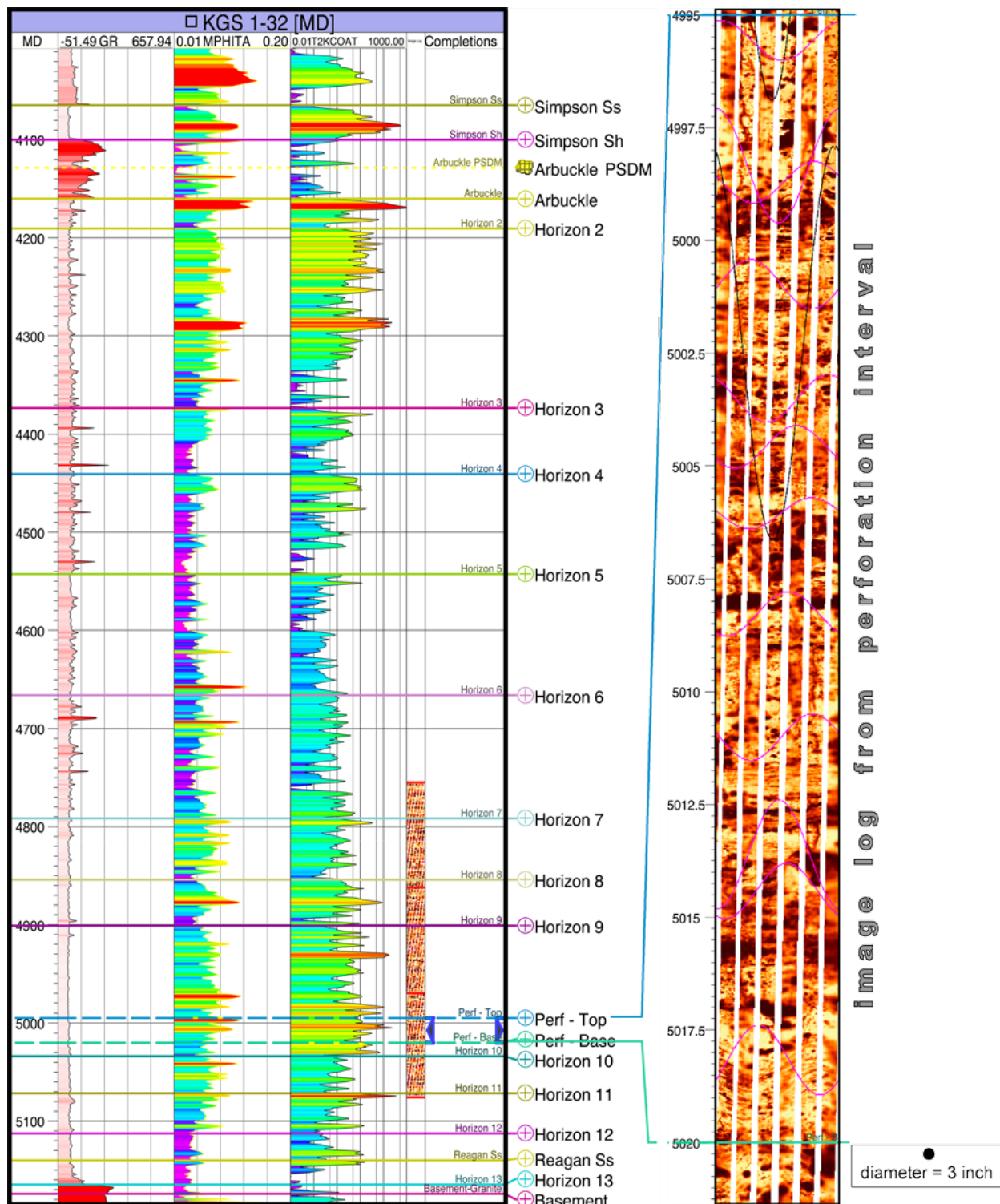


Figure 35. Geophysical logs within the Arbuckle Group at KGS 1-32. (Notes: MPHITA represents Haliburton porosity. Horizon markers represent porosity package. Image log on right presented to provide example of vugs; 3-in diameter symbol represents size of vug).

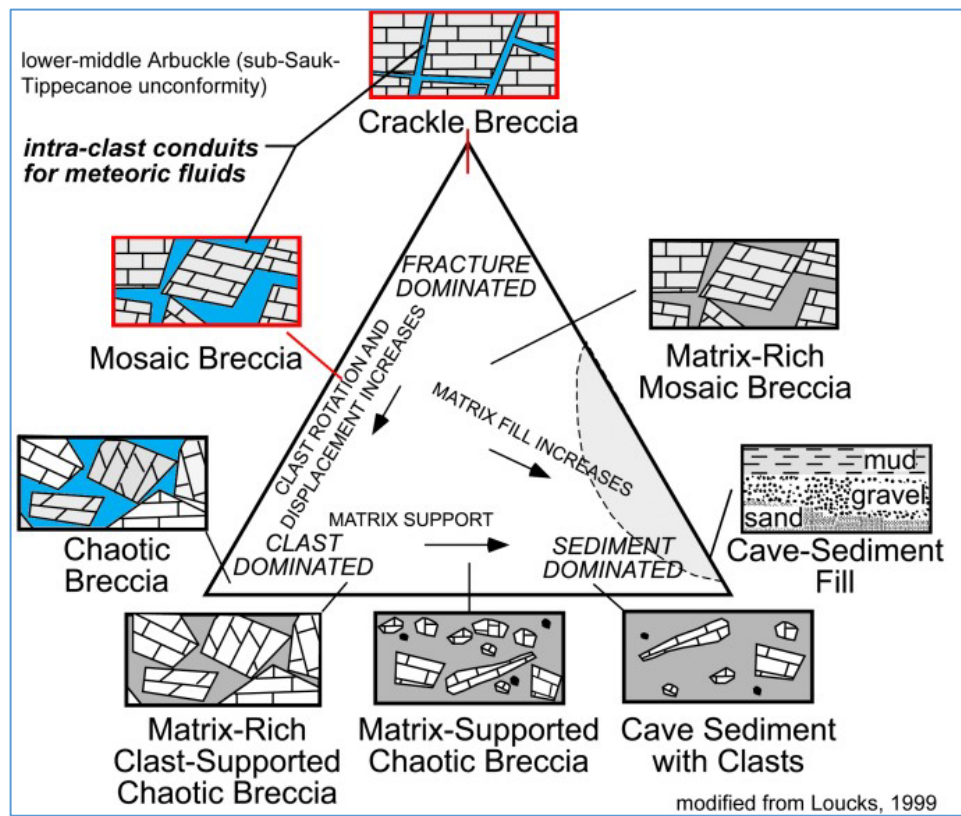


Figure 36. Classification of breccias and clastic deposits in cave systems exhibiting relationship between chaotic breccias, crackle breccias, and cave-sediment fill (source: Loucks, 1999).

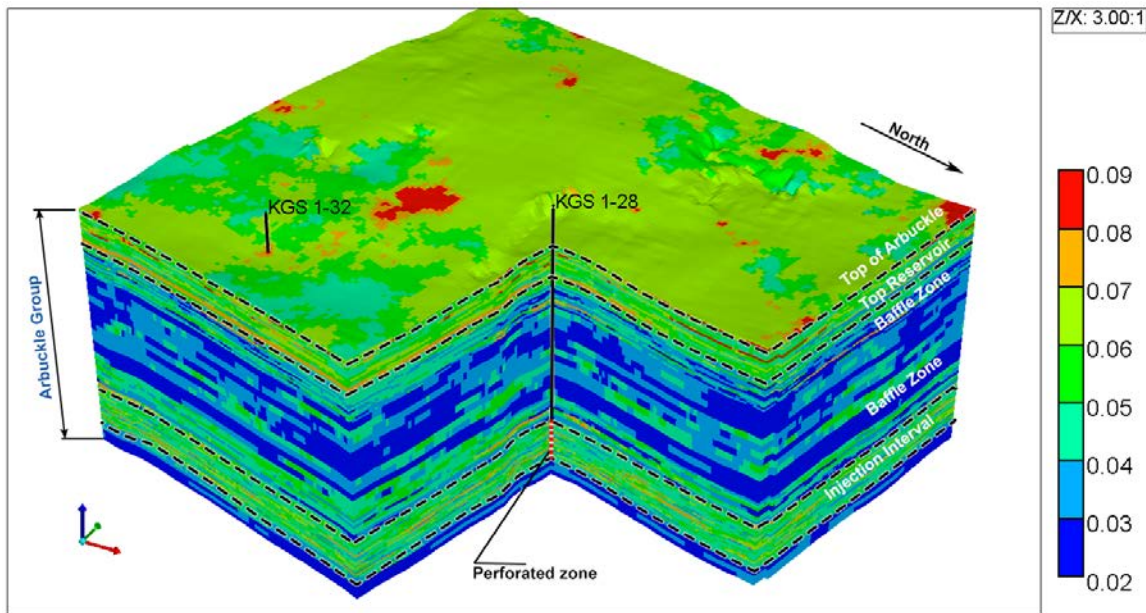


Figure 37. Upscaled porosity distribution in the Arbuckle Group based on the Petrel geomodel.

Permeability Modeling

The upscaled permeability logs shown in fig. 35 were created using the following controls: geometric averaging method; logs treated as points; and method set to simple. The permeability model was constructed using SGS. Isotropic semi-variogram ranges were set to 3,000 ft horizontally and 10 ft vertically. The permeability was collocated and co-Kriged to the porosity model using the calculated correlation coefficient (~ 0.70). The resulting SGS-based horizontal and vertical permeability distributions are presented in fig. 38a–f, which shows the relatively high permeability zone selected for completion within the injection interval. Table 4 presents the minimum, maximum, and average permeabilities within the Arbuckle Group in the geomodel.

Table 4. Hydrogeologic property statistics in hydrogeologic characterization and simulation models.

Property	Reservoir Characterization Geomodel			Reservoir Simulation Numerical Model		
	min	max	avg	min	max	avg
Porosity (%)	3.2	12.9	6.8	3.2	12.9	6.7
Horizontal Permeability (mD)	0.05	23,765	134.2	0.05	23,765	130.7
Vertical Permeability (mD)	.005	1,567	387	0.005	1,567	385

Arbuckle Reservoir Flow and Transport Model

Extensive computer simulations were conducted to estimate the potential impacts of CO₂ injection in the Arbuckle injection zone. The key objectives were to determine the resulting rise in pore pressure and the extent of CO₂ plume migration. The underlying motivation was to

determine whether the injected CO₂ could affect the USDW or potentially escape into the atmosphere through existing wells or hypothetical faults/fractures that might be affected by the injected fluid.

As in all reservoirs, there are data gaps that prevent an absolute or unique characterization of the geology and petrophysical properties. This results in conceptual, parametric, and boundary condition uncertainties. To address these uncertainties, comprehensive simulations were conducted to perform a sensitivity analysis using alternative parameter sets. A key objective was to derive model parameter sets that would result in the most negative impacts (the worst-case scenario; i.e., maximum formation pressures and largest extent of plume migration). However, simulations involving alternative parameter and boundary conditions that resulted in more favorable outcomes were also conducted to bracket the range of possible induced system states and outcomes.

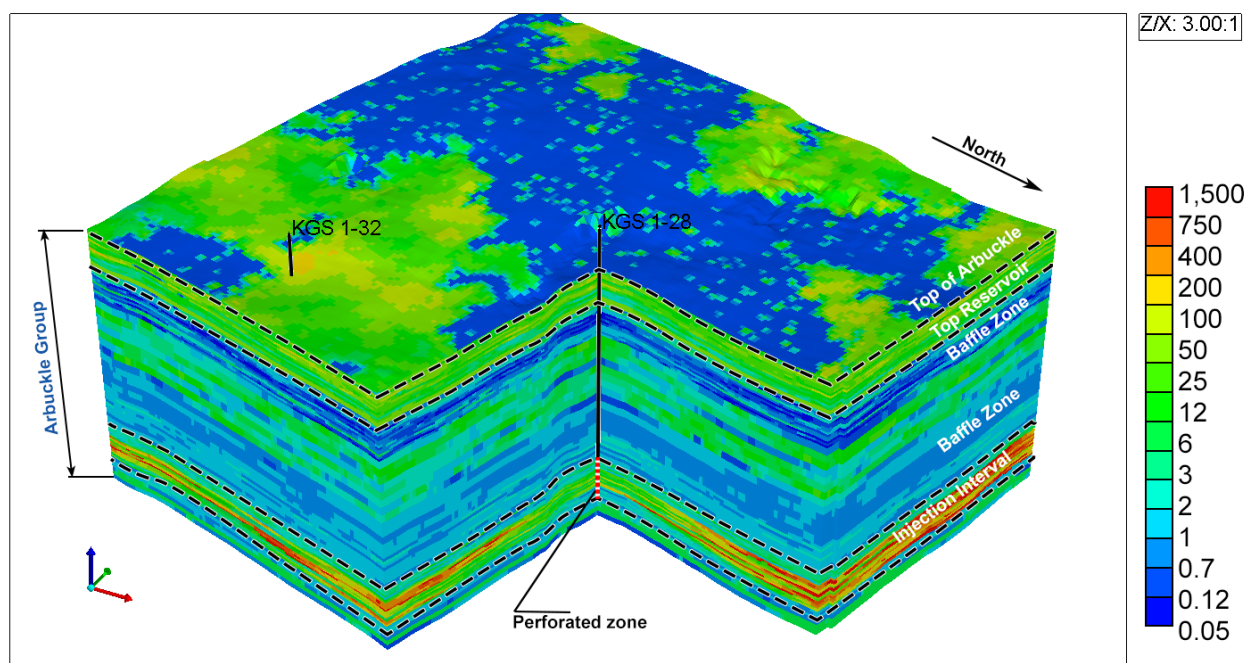


Figure 38a. Upscaled horizontal permeability (mD) distributions in the Arbuckle Group derived from Petrel geomodel.

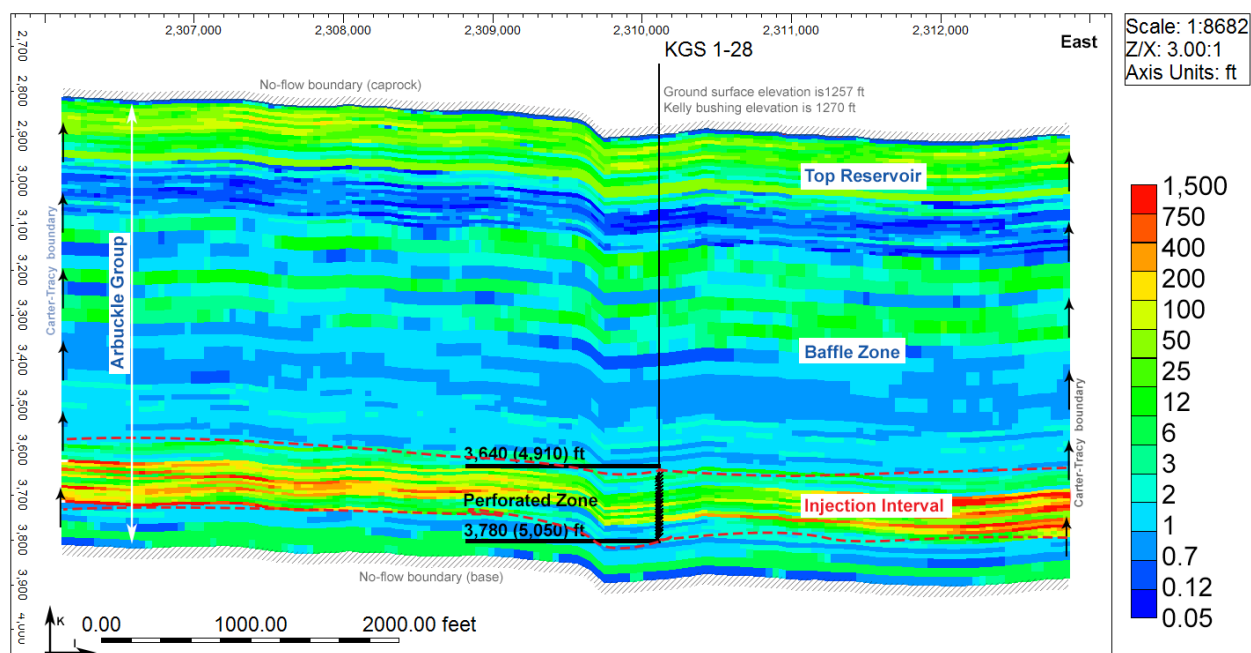


Figure 38b. Horizontal permeability (mD) distribution within an east-west cross section through the injection well (KGS 1-28), vertical cross-section A. Location of cross section shown in fig. 32a.

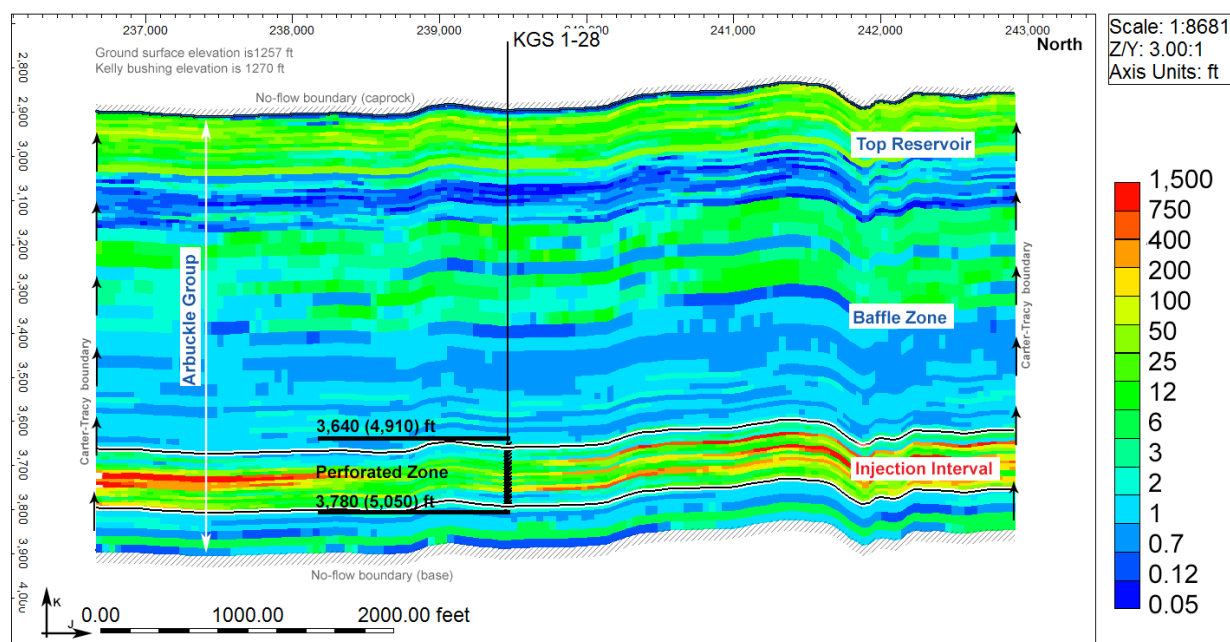


Figure 38c. Horizontal permeability (mD) distribution within a north-south cross section through the injection well (KGS 1-28), vertical cross-section B. Location of cross section shown in fig. 32a.

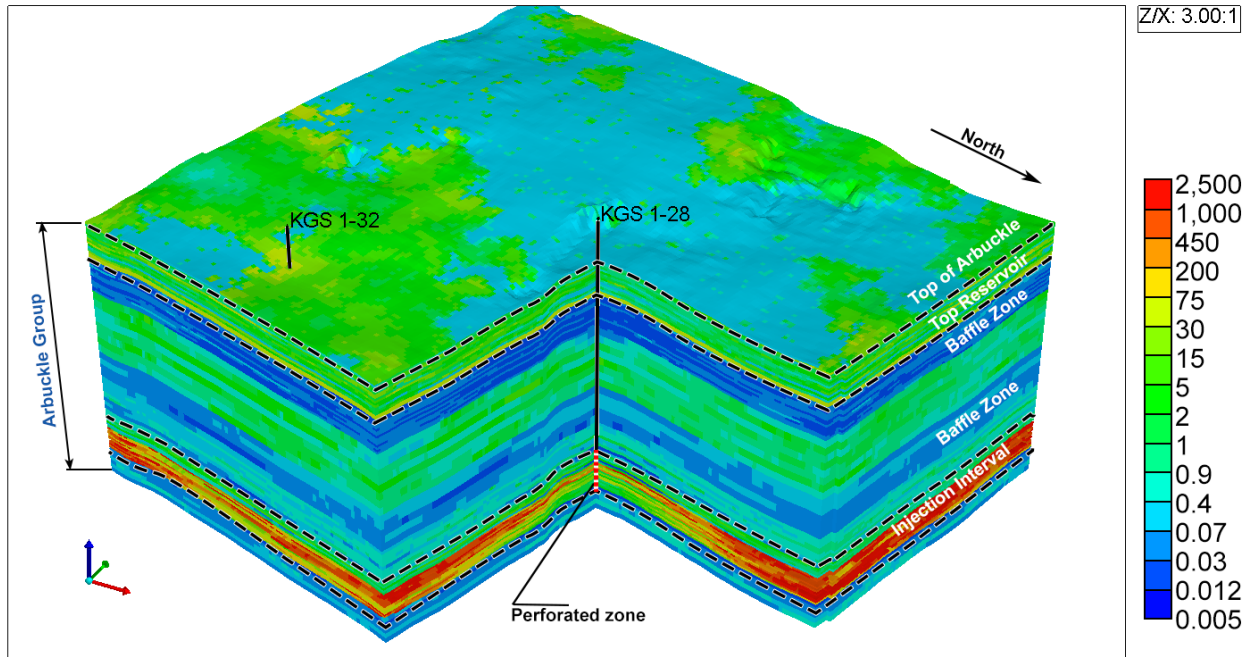


Figure 38d. Upscaled vertical permeability (mD) distributions in the Arbuckle Group derived from Petrel geomodel.

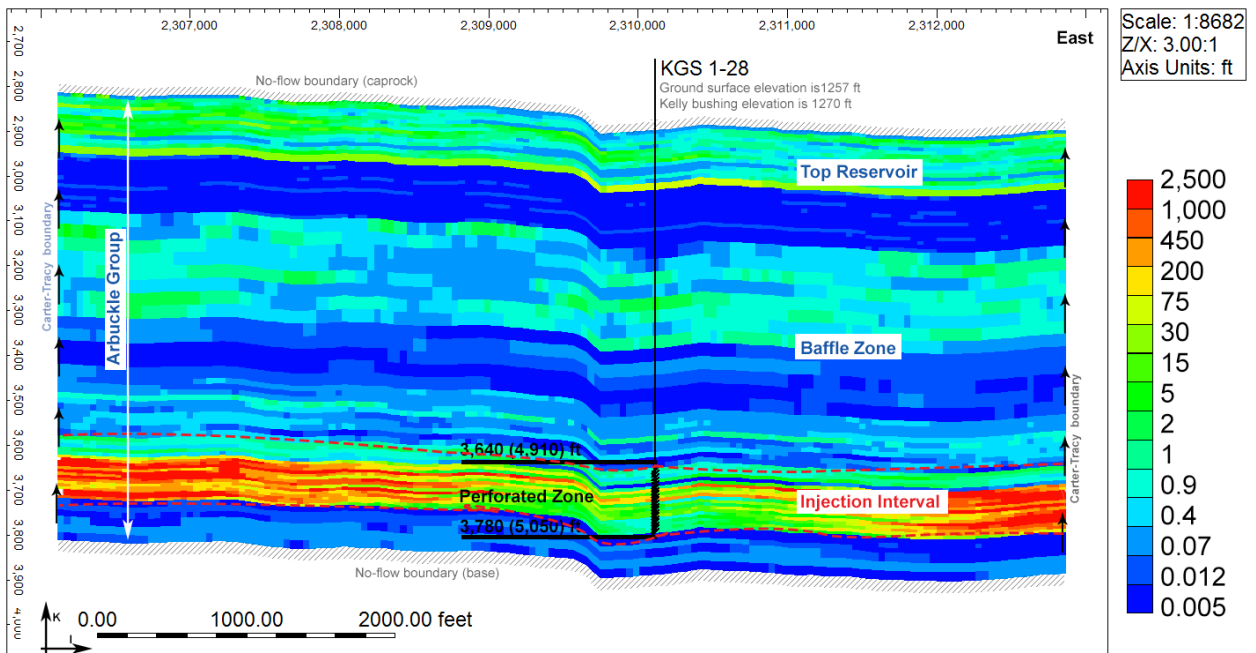


Figure 38e. Vertical permeability (mD) distribution within an east-west cross section through the injection well (KGS 1-28), vertical cross-section A. Location of cross section shown in fig. 32a.

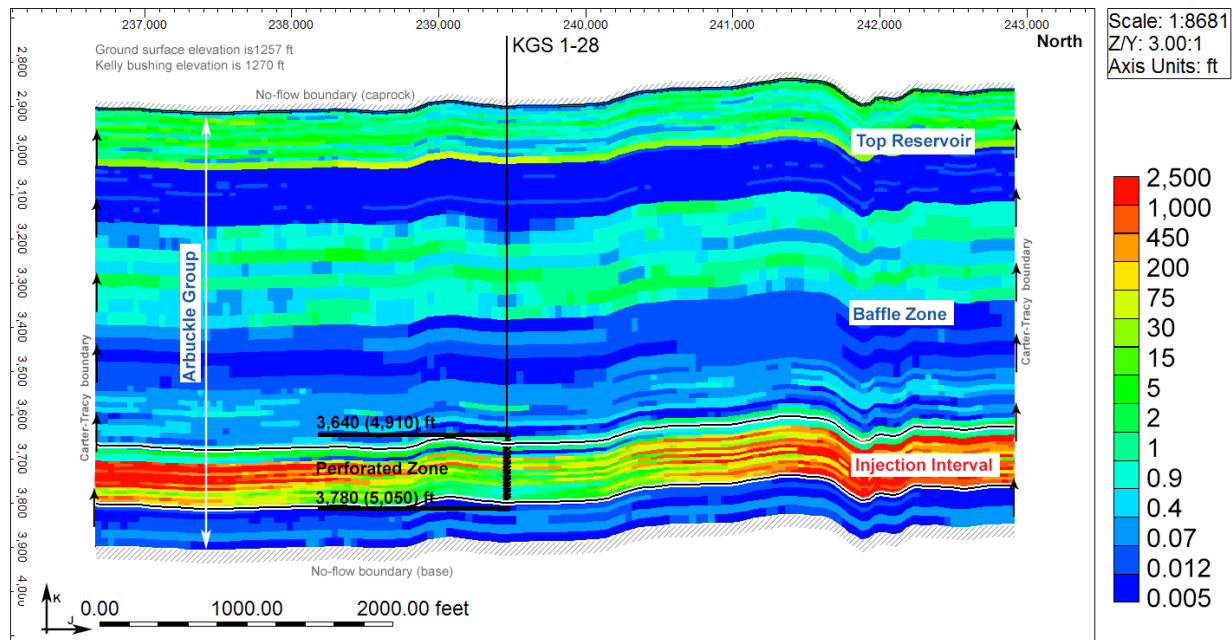


Figure 38f. Vertical permeability (mD) distribution within a north-south cross section through the injection well (KGS 1-28), vertical cross section B. Location of cross section shown in fig. 32a.

Simulation Software Description

The reservoir simulations were conducted using the Computer Modeling Group (CMG) GEM simulator. GEM is a full equation of state compositional reservoir simulator with advanced features for modeling the flow of three-phase, multi-component fluids and has been used to conduct numerous CO₂ studies (Chang et al., 2009; Bui et al., 2010). It is considered by DOE to be an industry standard for oil/gas and CO₂ geologic storage applications. GEM is an essential engineering tool for modeling complex reservoirs with complicated phase behavior interactions that have the potential to affect CO₂ injection and transport. The code can account for the thermodynamic interactions between three phases: liquid, gas, and solid (for salt precipitates). Mutual solubilities and physical properties can be dynamic variables depending on the phase composition/system state and are subject to well-established constitutive relationships that are a function of the system state (pressures, saturation, concentrations, temperatures, etc.). In particular, the following assumptions govern the phase interactions:

- Gas solubility obeys Henry's Law (Li and Nghiem, 1986)
- The fluid phase is calculated using Schmit-Wenzel or Peng-Robinson (SW-PR) equations of state (Sørense and Whitson, 1992)
- Changes in aqueous phase density with CO₂ solubility, mineral precipitations, etc., are accounted for with the standard or Rowe and Chou correlations.
- Aqueous phase viscosity is calculated based on Kestin, Khalifa, and Correia (1981).

Model Mesh and Boundary Conditions

The Petrel-based geomodel mesh discussed above consists of a 706 x 654 horizontal grid and 79 vertical layers for a total of 36,476,196 cells. The model domain spans from the base of the Arbuckle Group to the top of the Pierson Group. To reduce reservoir simulation time, this model was upscaled to a 157 x 145 horizontal mesh with 79 layers for a total of 1,798,435 cells to represent the same rock volume as the Petrel model for use in the CMG simulator. The thickness of the layers varies from 5 to 20 ft based on the geomodel, with an average of 13 feet.

Based on preliminary simulations, it was determined that due to the small scale of injection and the presence of a competent confining zone, the plume would be contained within the Arbuckle system for all alternative realizations of reservoir parameters. Therefore, the reservoir model domain was restricted to the Arbuckle aquifer with no-flow boundaries specified along the top (Simpson Group) and bottom (Precambrian basement) of the Arbuckle Group. The specification of no-flow boundaries along the top and bottom of the Arbuckle Group is justified because of the low permeabilities in the overlying and underlying confining zones. The permeability in the Pierson formation was estimated to be as low as 1.6 nanoDarcy (nD; 1.0^{-9} Darcy).

The simulation model, centered approximately on the injection well (KGS 1-28), extends approximately 1.2 mi in the east-west and 1.3 mi in the north-south orientations. Vertically, the model extends approximately 1,000 ft from the top of the Precambrian basement to the bottom of the Simpson Group. As discussed above, the model domain was discretized laterally by 157 x 145 cells in the east-west and north-south directions and vertically in 79 layers. The lateral boundary conditions were set as an infinite-acting Carter-Tracy aquifer (Dake, 1978; Carter and Tracy, 1960) with leakage. This is appropriate since the Arbuckle is an open hydrologic system extending over most of Kansas. Sensitivity simulations indicated that the increases in pore pressures and the plume extent were not meaningfully different by using a closed boundary instead of a Carter-Tracy boundary.

Hydrogeologic Properties

Geologic and hydrologic data pertaining to the Arbuckle Group are detailed in Sections 3 and 4 of the permit application. Site-specific hydrogeologic properties were used to construct a geomodel at the Wellington site. The porosity and permeability of the geomodel were upscaled to the coarser grid using a weighted averaging approach so that the total pore space volume in the Petrel geomodel was maintained in the upscaled reservoir simulation model. As shown in figs. 39a–b and 40, the qualitative representation (i.e., the shape) of the permeability and porosity distribution remained similar in both the geo and reservoir models. The upscaled reservoir grid was imported from Petrel into CMG Builder, where the model was prepared for dynamic simulations assuming an equivalent porous medium model with flow limited to only the rock matrix. The minimum, maximum, and average porosity and permeabilities in the reservoir model are documented in table 4 alongside the statistics for the geomodel.

Rock Type Assignment

Nine rock types and corresponding tables with capillary pressure hysteresis were developed based on reservoir quality index (RQI) ranges, where RQI is calculated for each grid cell using the formula:

$$RQI = 0.0314 \sqrt{Perm/Porosity}$$

Using RQI ranges, rock types are assigned using CMG Builder's Formula Manager. The resulting maps of rock type distribution in the model are shown in fig. 41a–c. The division of the nine rock-types (RT) was based on dividing the irreducible water saturation into nine ranges to find their equivalent RQI as shown in table 5. Relative permeability and capillary pressure curves were calculated for each of the nine RQI values.

Table 5. RQI and relative permeability types assignments (RT).

	RQI		
RT	RQI from	RQI To	Ave RQI
1	40	10	25
2	10	2.5	6.25
3	2.5	1	1.75
4	1	0.5	0.75
5	0.5	0.4	0.45
6	0.4	0.3	0.35
7	0.3	0.2	0.25
8	0.2	0.1	0.15
9	0.1	0.01	0.055

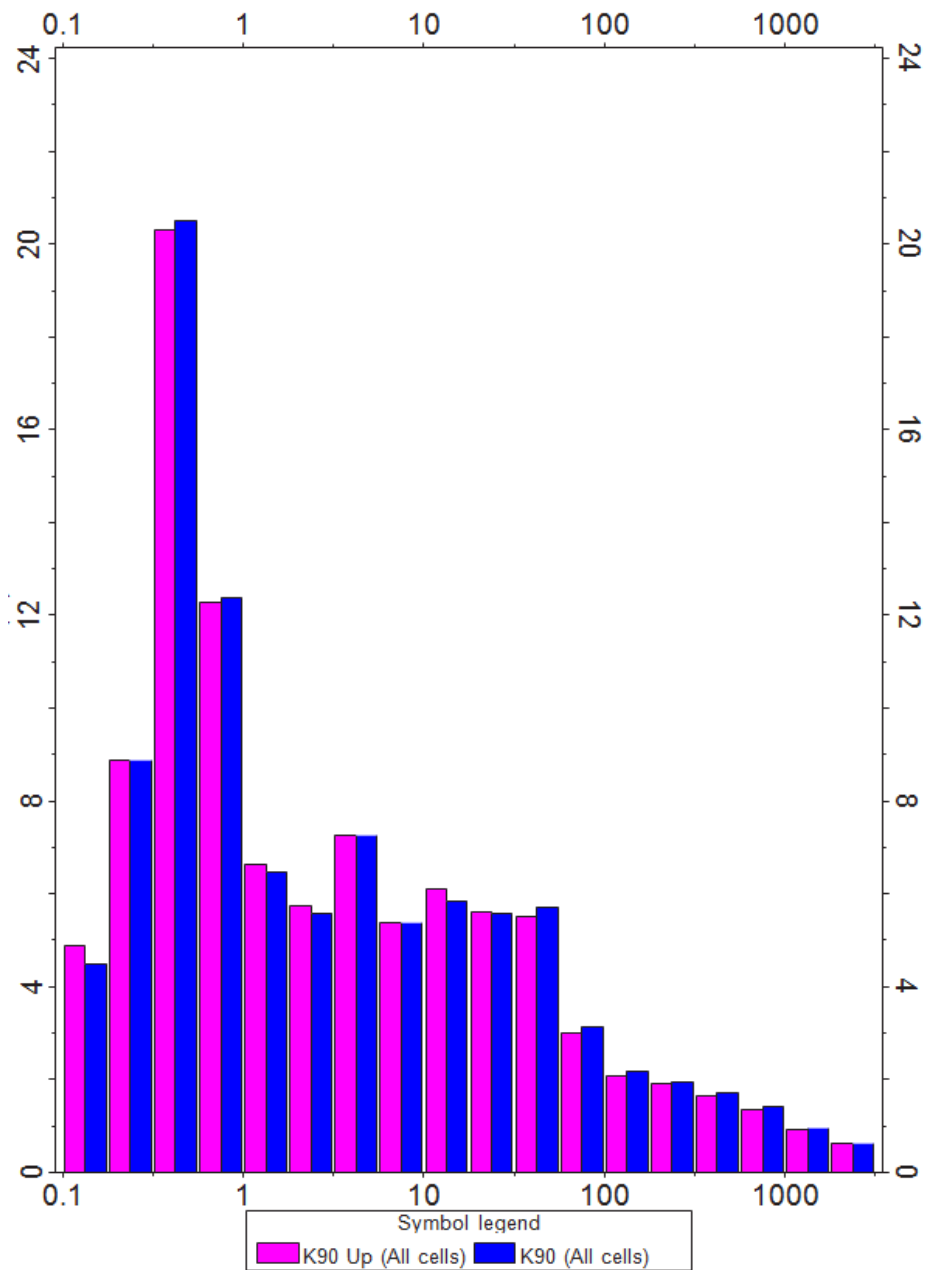


Figure 39a. Horizontal permeability distribution histogram comparison for original (blue) and upscaled (pink) model properties, showing horizontal permeability distributions (in mD) for an Arbuckle modeling domain used for simulation of the CO₂ plume. (Note: x-axis represents permeability in milliDarcy, mD. Y-axis is showing the percentages of each horizontal permeability block that is present in a model.)

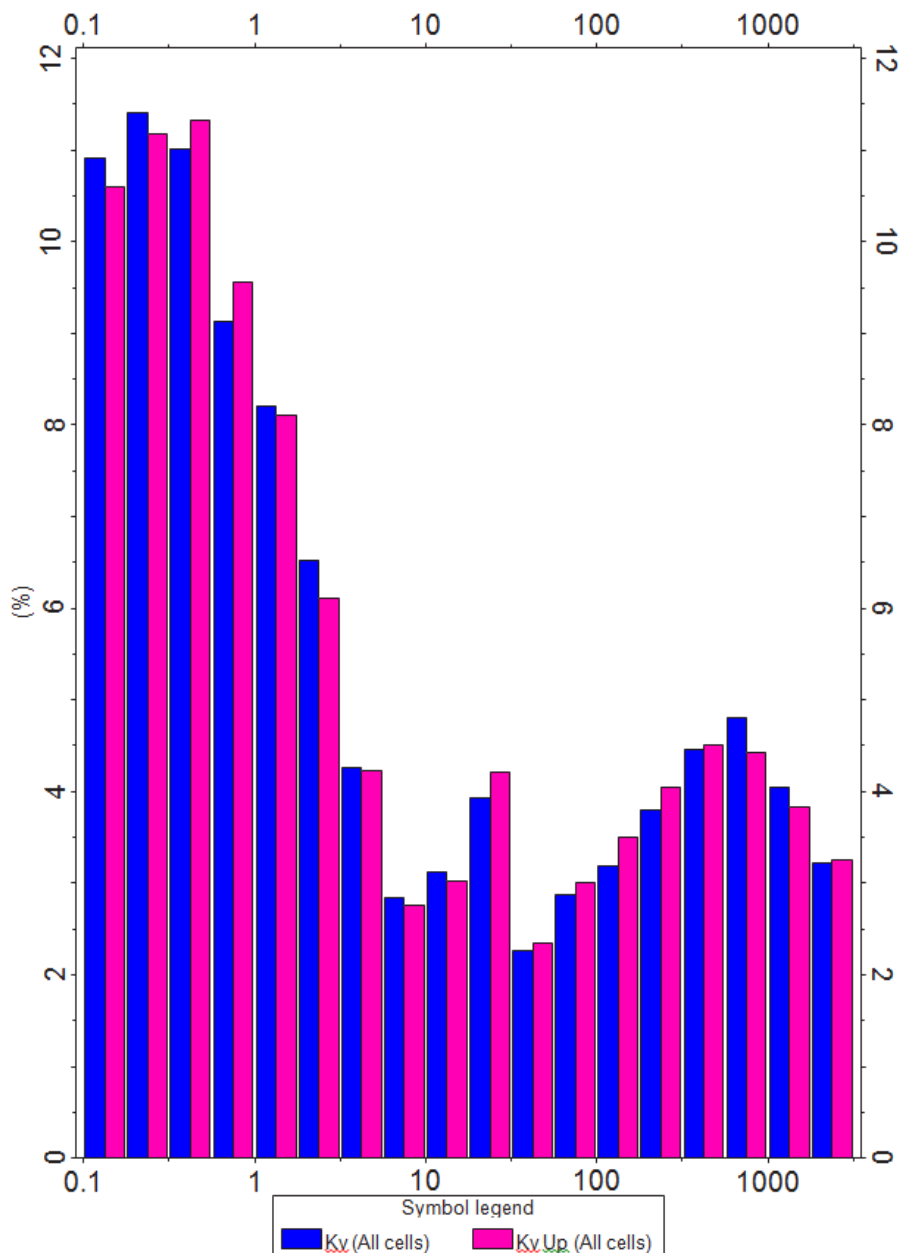


Figure 39b. Vertical permeability distribution histogram comparison for original (blue) and upscaled (pink) model properties, showing vertical permeability distributions (in mD) for an Arbuckle modeling domain used for simulation of the CO₂ plume. (Note: x-axis represents permeability in milliDarcy, mD. Y-axis is showing the percentages of each vertical permeability block that is present in a model.)

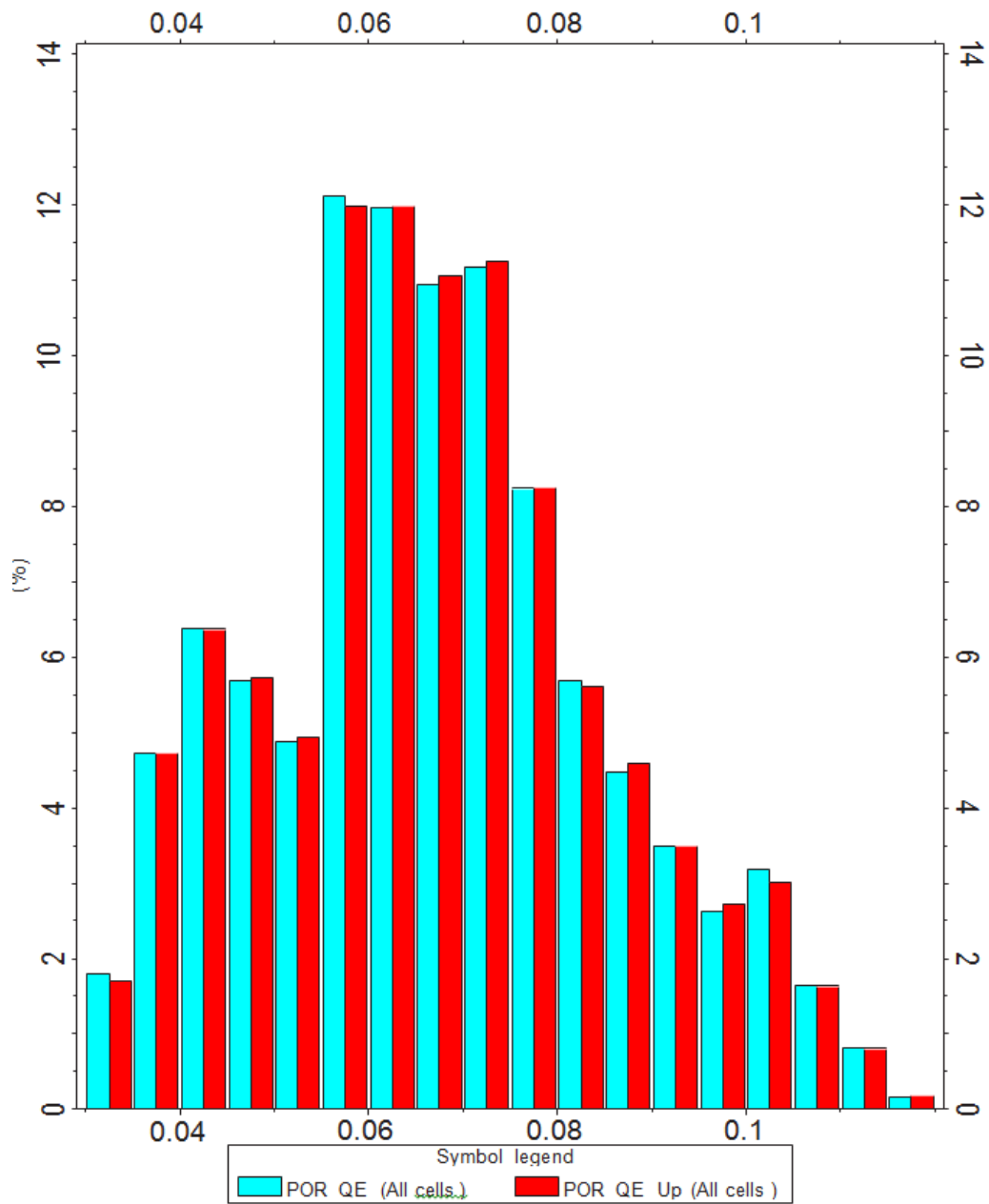


Figure 40. Porosity distribution histogram comparison for original and upscaled model properties.
 (Note: x-axis represents porosity.)

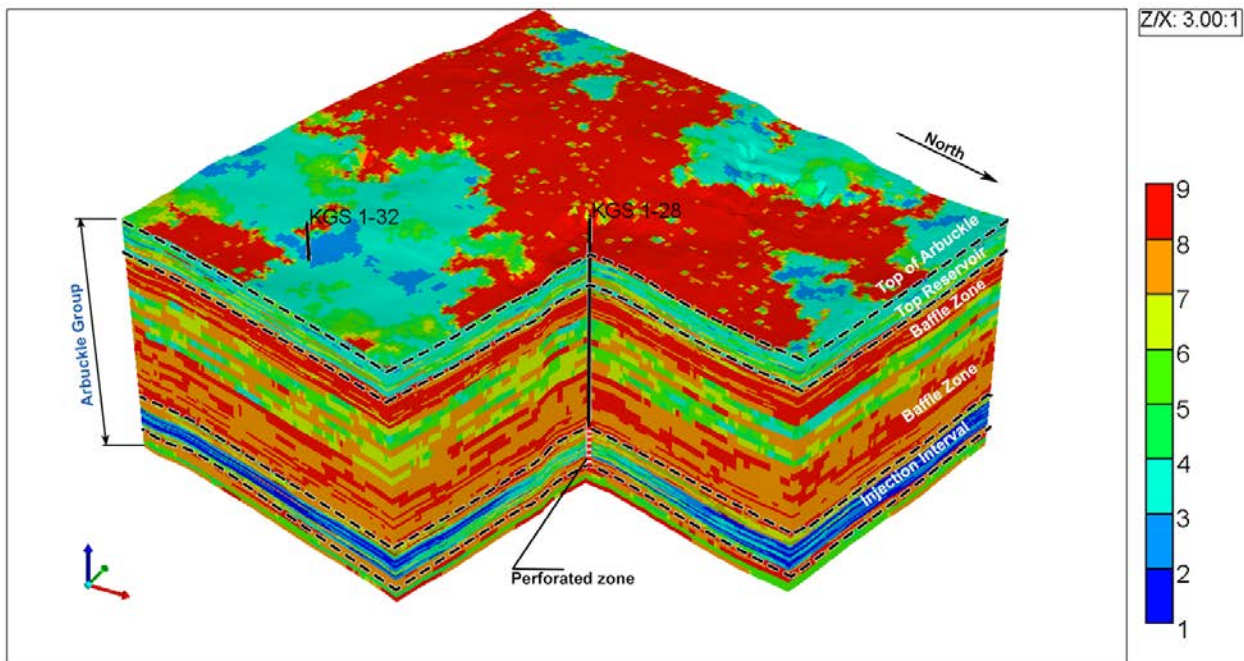


Figure 41a. Rock type distribution model.

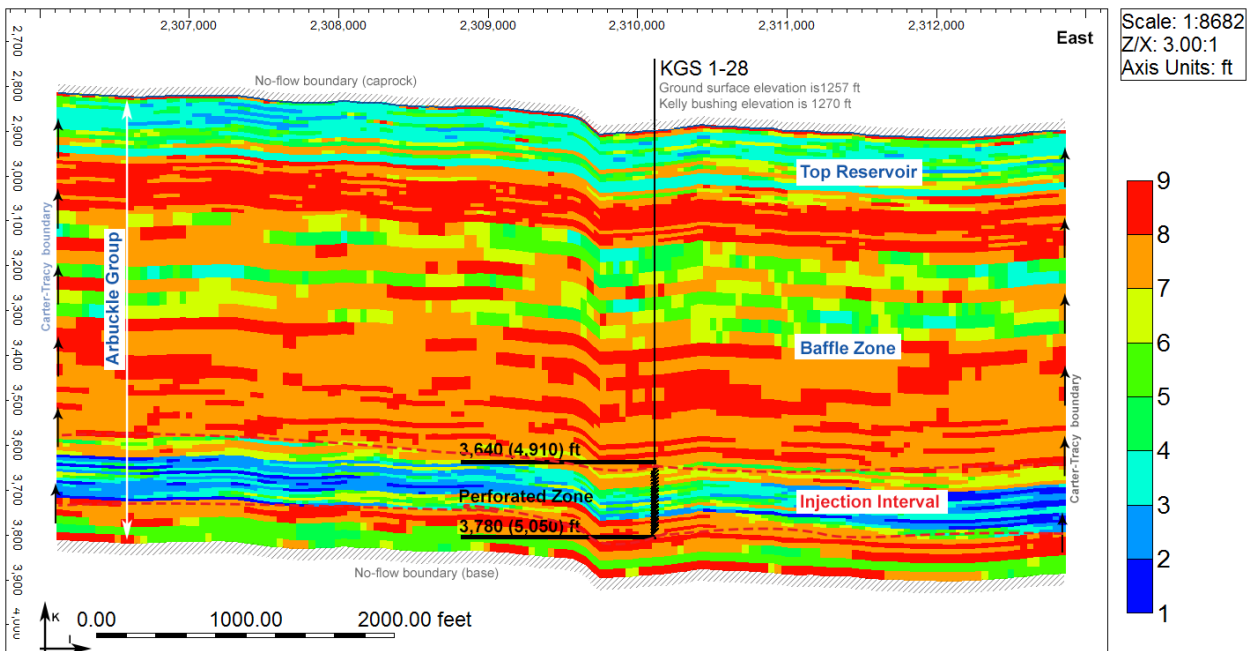


Figure 41b. Rock type distribution model, distribution within an east-west cross section through the injection well (KGS 1-28), vertical cross-section A.

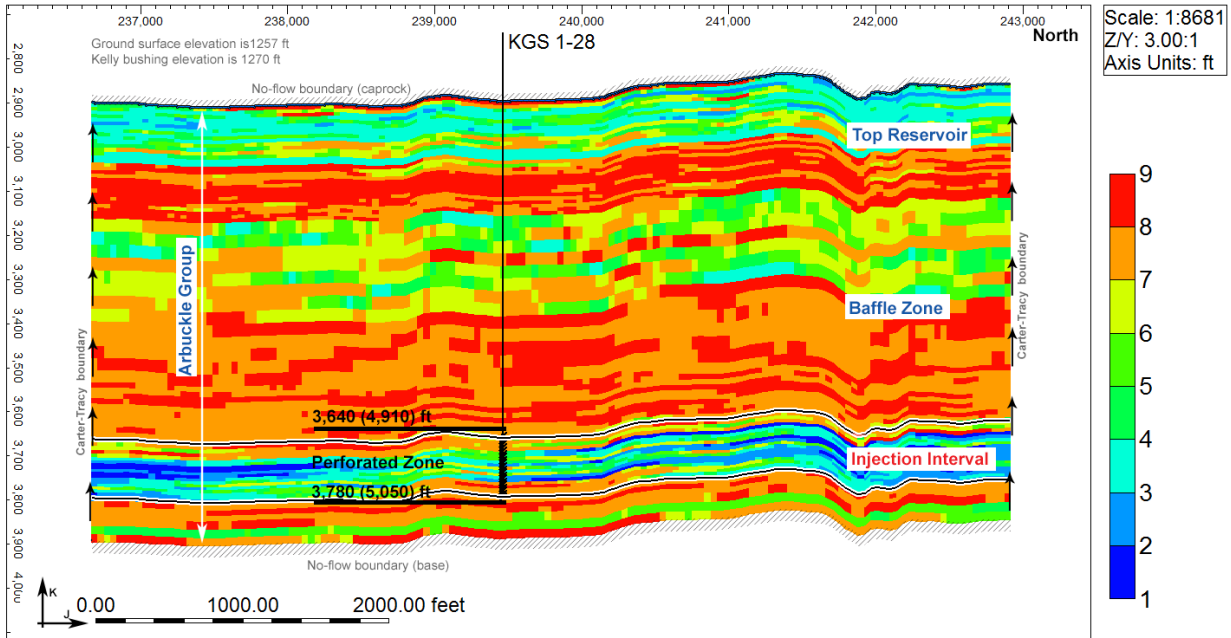


Figure 41c. Rock type distribution within a north-south cross section through the injection well (KGS 1-28), vertical cross-section B.

5.6 Relative Permeability

Nine sets of relative permeability curves for both drainage and imbibition were calculated for the nine rock types. These sets of relative permeability curves were calculated based on a recently patented formula (SMH reference No: 1002061-0002) that relates the end points to RQI, thereby resulting in a realistic relative permeability data set. The validation of the method is presented below under Validation of the Capillary Pressure and Relative Permeability Methods. Literature experimental studies, including Krevor and Benson (2012, 2015), indicate that the maximum experimental CO_2 saturation ($\text{SCO}_{2\text{max}}$) and maximum CO_2 relative permeability ($\text{KrCO}_{2\text{max}}$) in higher permeability samples typically do not reach their actual values and are lower than expected. The authors note that the cause of low experimental end points is the unattainable high capillary pressure in the high permeability core samples. Calculations based on the new patented method addresses and resolves this issue. The highest maximum CO_2 relative permeability ($\text{KrCO}_{2\text{max}}$) for drainage curves from literature (Bennion and Bachu, 2007) is 0.54, which is lower than expected; however, the highest maximum CO_2 relative permeability using the new method is 0.71, which is a more realistic value. As noted above, measured relative permeabilities from literature do not represent the end points of relative permeability curves and they need to be adjusted. Using this new method, $\text{SCO}_{2\text{max}}$ and $\text{KrCO}_{2\text{max}}$ are scaled up to reasonable values.

Highest and lowest Corey CO_2 exponent values from Bennion and Bachu (2010) were selected and they were assigned to the nine RQI values in a descending order from high to low. The full range of RQI assignments and relative permeability tables can be found in Appendix E. An example of capillary pressure and relative permeability for both drainage and imbibition is presented in table 6. Corey Water exponents for different permeabilities from literature did not show much variability. Therefore, average values were used for both drainage and imbibition curves. Figure 42a presents relative permeability curves for an RQI value of 0.35 for illustrative

purposes. Figure 42b presents the same set of curves for the full range of RQI values. Residual CO_2 saturation (SCO_{2r}) for calculating imbibition curves was needed. SCO_{2r} was calculated based on a correlation between residual CO_2 saturation (SCO_{2r}) and initial CO_2 saturation (SCO_{2i}) (Burnside and Naylor, 2014).

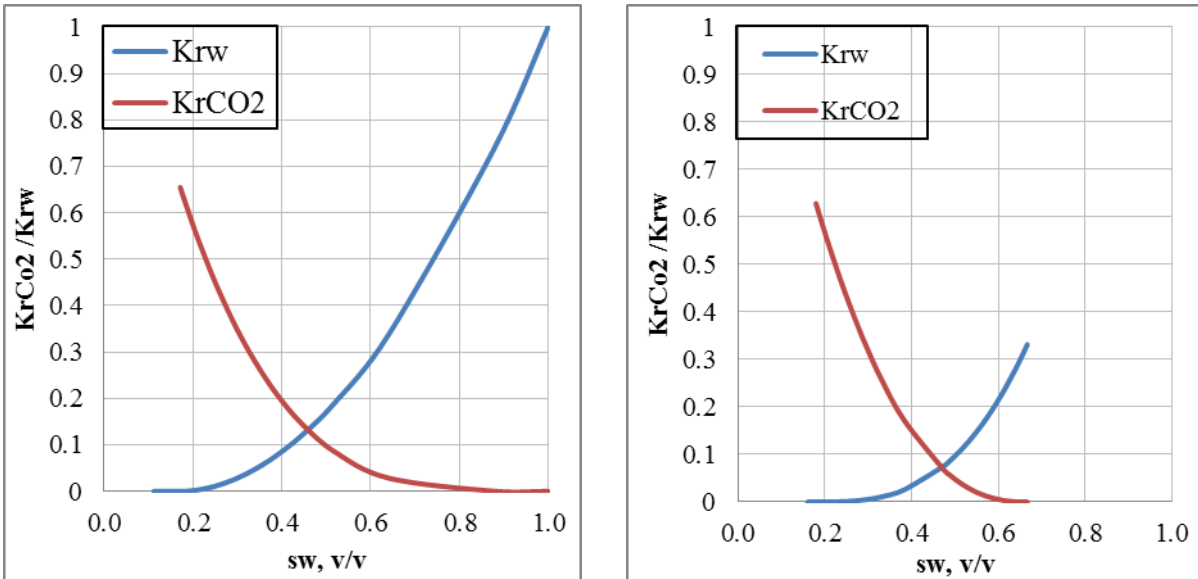
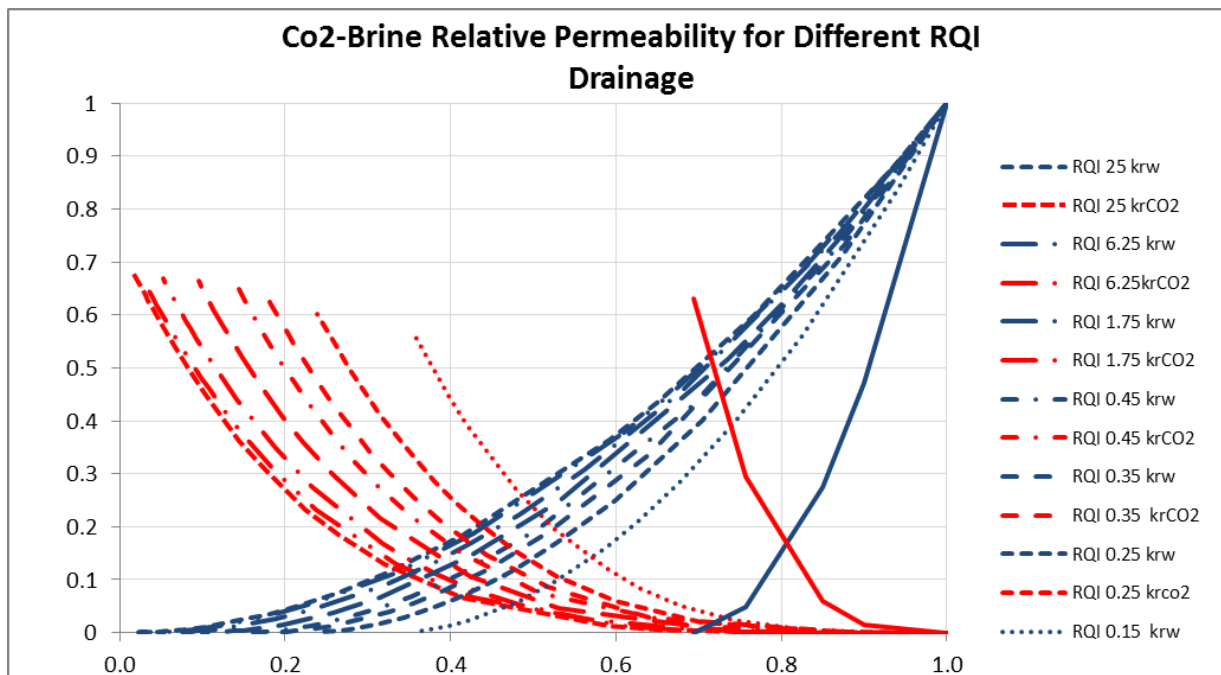


Figure 42a. Calculated relative permeability for drainage (left) and imbibition (right) for $\text{RQI}=0.35$.



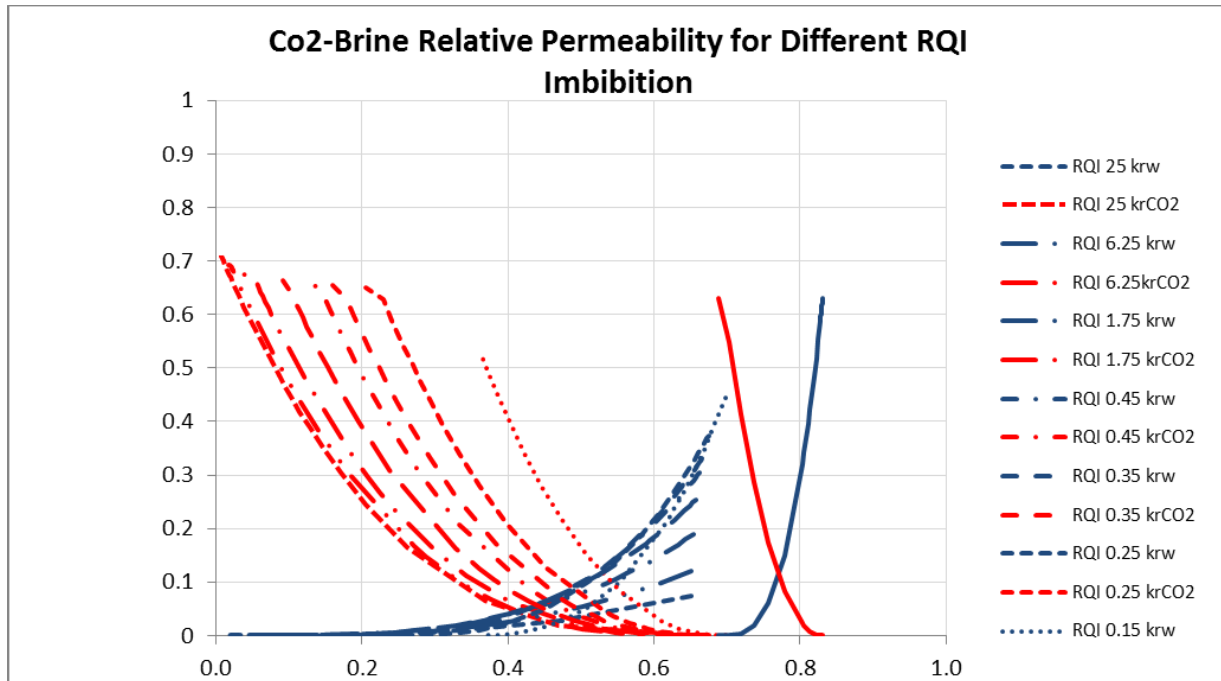


Figure 42b. Calculated relative permeability for drainage (top) and imbibition (bottom) for full set of RQI.

Table 6. Example of capillary pressure and relative permeability drainage and imbibition tables for rock type 6 (RQI=0.35).

Drainage Curves

RQI range from 0.3-0.4-AveRQI=0.35				
Pc	Sw	SCO ₂	Krw	krCO ₂
1	1.000	0.000	1.000	0.000
2	0.877	0.123	0.735	0.001
3	0.641	0.359	0.338	0.029
4	0.518	0.482	0.190	0.086
5	0.443	0.557	0.119	0.148
6	0.392	0.608	0.080	0.205
7	0.354	0.646	0.056	0.257
8	0.326	0.674	0.041	0.302
9	0.304	0.696	0.030	0.341
10	0.286	0.714	0.023	0.375
12	0.258	0.742	0.013	0.432
14	0.238	0.762	0.008	0.478
18	0.211	0.789	0.003	0.545

Imbibition Curves

RQI range from 0.3-0.4-AveRQI=0.35				
Pc	Sw	SCO ₂	Krw	krCO ₂
0	0.666	0.334	0.331	0.000
0.00	0.665	0.335	0.328	0.000
0.01	0.663	0.337	0.325	0.000
0.02	0.660	0.340	0.319	0.000
0.03	0.657	0.343	0.313	0.000
0.04	0.654	0.346	0.308	0.000
0.05	0.652	0.348	0.302	0.000
0.06	0.649	0.351	0.297	0.000
0.07	0.646	0.354	0.292	0.000
0.08	0.643	0.357	0.287	0.000
0.09	0.640	0.360	0.282	0.001
0.1	0.638	0.362	0.277	0.001
0.2	0.612	0.388	0.234	0.003

20	0.201	0.799	0.002	0.571
25	0.183	0.817	0.000	0.620
30	0.171	0.829	0.000	0.655
40	0.156	0.844	0.000	0.655
50	0.146	0.854	0.000	0.655
60	0.140	0.860	0.000	0.655
70	0.135	0.865	0.000	0.655
80	0.131	0.869	0.000	0.655
90	0.129	0.871	0.000	0.655
100	0.126	0.874	0.000	0.655
150	0.119	0.881	0.000	0.655
200	0.116	0.884	0.000	0.655
300	0.112	0.888	0.000	0.655

0.3	0.589	0.411	0.200	0.008
0.4	0.569	0.431	0.171	0.013
0.5	0.550	0.450	0.148	0.020
0.6	0.532	0.468	0.128	0.029
0.7	0.516	0.484	0.112	0.038
0.8	0.501	0.499	0.098	0.047
0.9	0.487	0.513	0.086	0.057
1	0.474	0.526	0.076	0.067
2	0.383	0.617	0.026	0.172
3	0.329	0.671	0.011	0.261
4	0.293	0.707	0.005	0.333
5	0.267	0.733	0.002	0.390
6	0.248	0.752	0.001	0.437
7	0.233	0.767	0.001	0.476
8	0.221	0.779	0.000	0.508
9	0.211	0.789	0.000	0.536
10	0.203	0.797	0.000	0.559
12	0.189	0.811	0.000	0.598
14	0.180	0.820	0.000	0.629
20	0.160	0.840	0.000	0.655
30	0.144	0.856	0.000	0.655
40	0.135	0.865	0.000	0.655
50	0.129	0.871	0.000	0.655
60	0.126	0.874	0.000	0.655
70	0.123	0.877	0.000	0.655
80	0.121	0.879	0.000	0.655
90	0.119	0.881	0.000	0.655
100	0.117	0.883	0.000	0.655
150	0.113	0.887	0.000	0.655
200	0.111	0.889	0.000	0.655
300	0.109	0.891	0.000	0.655

Capillary Pressure Curves

Nine capillary pressure curves were calculated for drainage and imbibition for nine RQI values based on a recently patented formula (SMH reference No: 1002061-0002). The formula constitutes a function for the shape of P_c curves and functions for the end points that are entry pressure (P_{entry}) and irreducible water saturation (S_{wir}). The end points are correlated to RQI. P_{entry} was calculated from entry radius (R15) and Winland (R35). There is a relationship between R35 and R15 and a relationship between P_{entry} and R15; therefore, P_{entry} can be calculated from R15 derived from R35. S_{wir} was calculated from the NMR log at a P_c equal to 20 bars (290 psi). To calculate imbibition curves, a residual CO_2 saturation (CO_{2r}) value was needed. CO_{2r} was calculated from a relationship between initial CO_2 saturation and CO_{2r} as discussed above. The capillary pressure curves for drainage and imbibition for RQI of 0.35 are presented in fig. 43. The capillary pressure data for the full set of RQI values are presented in Appendix E.

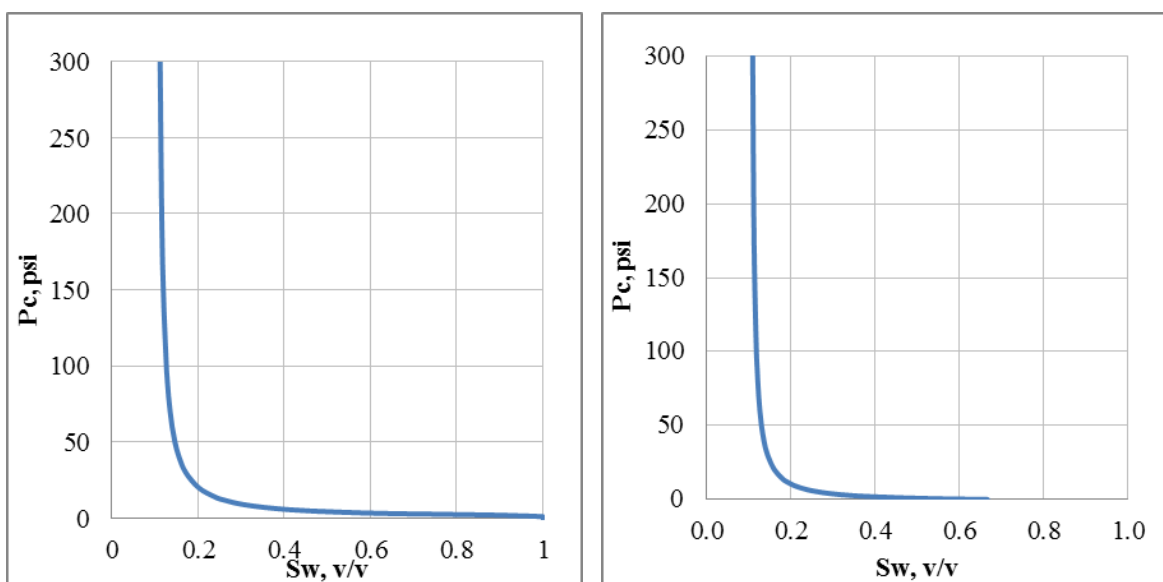


Figure 43. Capillary pressure curves for drainage (left) and imbibition (right) for an RQI value of 0.35.

Validation of the Capillary Pressure and Relative Permeability Methods

The capillary pressure and relative permeability curves were estimated in the laboratory for the Mississippian Reservoir as part of the Wellington Mississippian Enhanced Oil Recovery (EOR) project located approximately a mile southwest of the Wellington CO_2 storage site. The laboratory-derived curves were used to validate the relative permeability and capillary pressure approach for the Arbuckle discussed above and this was deemed reasonable since the same approach that was used in the Mississippian was also used for the Arbuckle.

Two core plug samples with similar RQI values were sent to Core Laboratories for capillary pressure and relative permeability measurements. The relative permeability and capillary pressure curves were calculated twice for the Mississippian reservoir—before and after the core results were obtained from the laboratory. The initial estimation of P_c curves was based on the end points that were calculated from the NMR log. As shown in fig. 44a, there is a slight difference between the calculated P_c and measured P_c before calibration. However, there is an excellent match between the calculated P_c and the measured P_c after calibration using the core

measured end points. Similarly, as shown in fig. 44b, there is a slight difference between the initial calculated relative permeability and measured relative permeability, but the match is excellent after calibration.

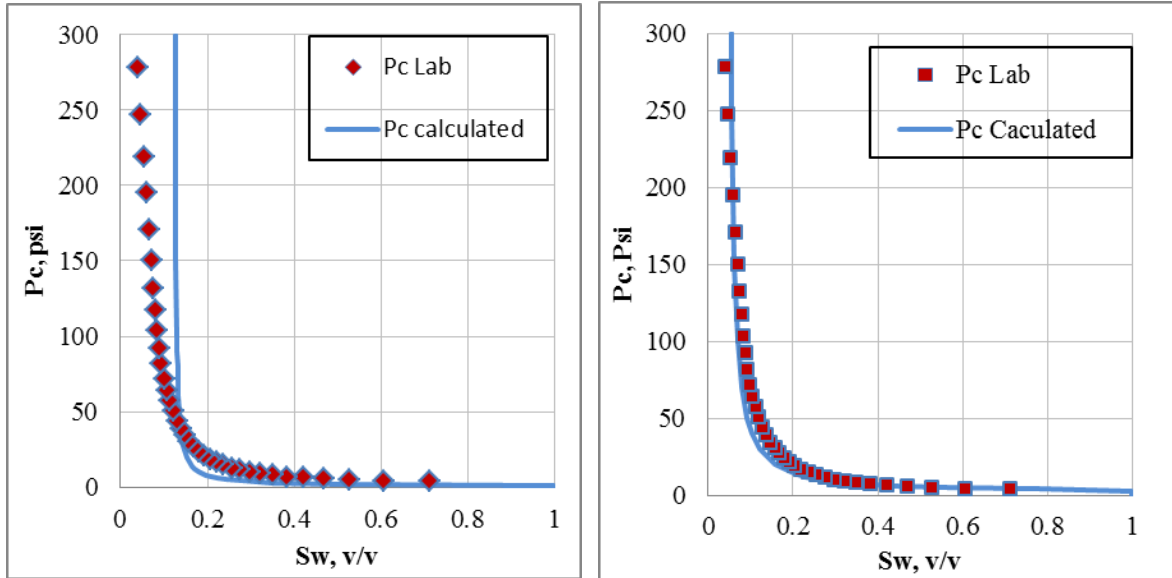


Figure 44a. Capillary pressure curves for an RQI value of 0.2 before calibration (left) and after calibration (right).

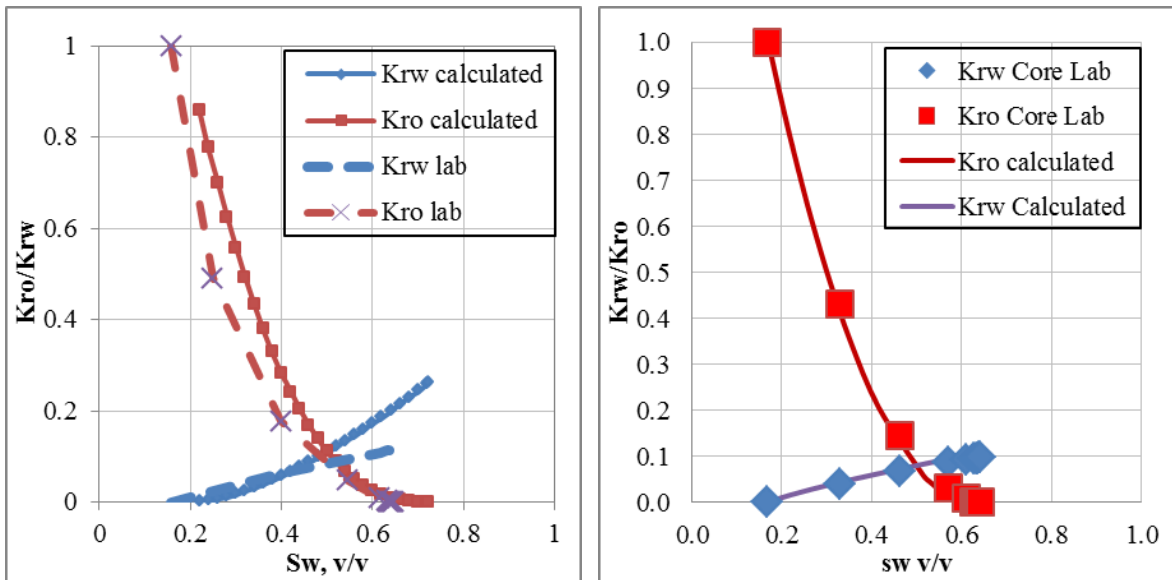


Figure 44b. Relative permeability curves for an RQI value of 0.16 before calibration (left) and after calibration (right).

Initial Conditions and Injection Rates

Table 7 lists the initial conditions specified in the reservoir model. The simulations were conducted assuming isothermal conditions, but a thermal gradient of 0.008 °C/ft was considered

for specifying petrophysical properties that vary with layer depth and temperature such as CO₂ relative permeability, CO₂ dissolution in formation water, etc. The original static pressure in the injection zone (at a reference depth of 4,960 ft) was set to 2,093 psi and the Arbuckle pressure gradient of 0.48 psi/ft was assumed for specifying petrophysical properties. A 140 ft thick perforation zone in well KGS 1-28 was specified between 4,910 and 5,050 ft. A constant brine density of 68.64 lbs/ft³ (specific gravity of 1.1) was assumed. A total of 40,000 metric tons (MT) of CO₂ was injected in the Arbuckle Formation over a period of nine months at an average injection rate of 150 tons/day

Table 7. Model input specification and CO₂ injection rates.

Temperature	60 °C (140 °F)
Temperature Gradient	0.008 °C/ft
Pressure	2,093 psi (14.43 MPa) @ 4,960 ft RKB
Perforation Zone	4,910-5,050 ft
Perforation Length	140 ft (model layers 54 to 73)
Injection Period	9 months
Injection Rate	150 tons/day
Total CO ₂ injected	40,000 MT

Permeability and Porosity Alternative Models

The base-case reservoir model has been carefully constructed using a sophisticated geomodel as discussed in previous sections, which honors site-specific hydrogeologic information obtained from laboratory tests and log-based analyses. However, to account and test for sensitivity of hydrogeologic uncertainties, a set of alternate parametric models were developed by varying the porosity and horizontal hydraulic permeability. Specifically, the porosity and permeability were increased and decreased by 25% following general industry practice (FutureGen Industrial Alliance, 2013). This resulted in nine alternative models, listed in table 8. Simulation results based on all nine models were evaluated to derive the worst-case impacts on pressure and migration of the plume front for purposes of establishing the AoR and ensuring that operational constraints are not exceeded

Table 8. Nine alternative permeability-porosity combination models (showing multiplier of base-case permeability and porosity distribution assigned to all model cells).

Alternative Models	Base Porosity x 0.75	Base Porosity	Base Porosity x 1.25
Base Permeability x 0.75	K-0.75/Phi-0.75	K-0.75/Phi-1.0	K-0.75/Phi-1.25
Base Permeability	K-1.0/Phi-0.75	K-1.0/Phi-1.0	K-1.0/Phi-1.25
Base Permeability x 1.25	K-1.25/Phi-0.75	K-1.25/Phi-1.0	K-1.25/Phi-1.25

6. Reservoir Simulation Results

For the simulations, 40,000 MT of CO₂ were injected into the KGS 1-28 well at a constant rate of approximately 150 tons per day for a period of nine months. Although Berexco sought a permit for injecting 40,000 tons, it was expected that only 26,000 tons would be injected due to budgetary constraints. At the request of the EPA, an alternate set of simulations were conducted with a total injection volume of only 26,000 tons. All simulation results presented below for 40,000 tons are repeated for an injection volume of 26,000 tons in Appendix F. Note that only the simulation result figures are provided in Appendix A; the context for each figure is the same as provided in the following description for an injection volume of 40,000 tons.

A total of nine models representing three sets of alternate permeability-porosity combinations as specified in table 8 were simulated with the objective of bracketing the range of expected pressures and extent of CO₂ plume migration.

The extent of lateral plume migration depends on the particular combination of permeability-porosity in each of the nine alternative models. These two parameters are independently specified in CMG as they are assumed to be decoupled. A high-permeability value results in farther travel of the plume due to gravity override, buoyancy, and updip migration. Similarly, a low effective porosity for the same value of permeability results in farther travel for the plume as compared to high porosity as the less-connected pore volume results in faster pore velocity. The high-permeability/low-porosity combination (k-1.25/phi-0.75) resulted in the largest horizontal plume dimension. In contrast, the highest induced pressures were obtained for the alternative model with the lowest permeability and the lowest porosity (k-0.75/phi-0.75).

CO₂ Plume Migration

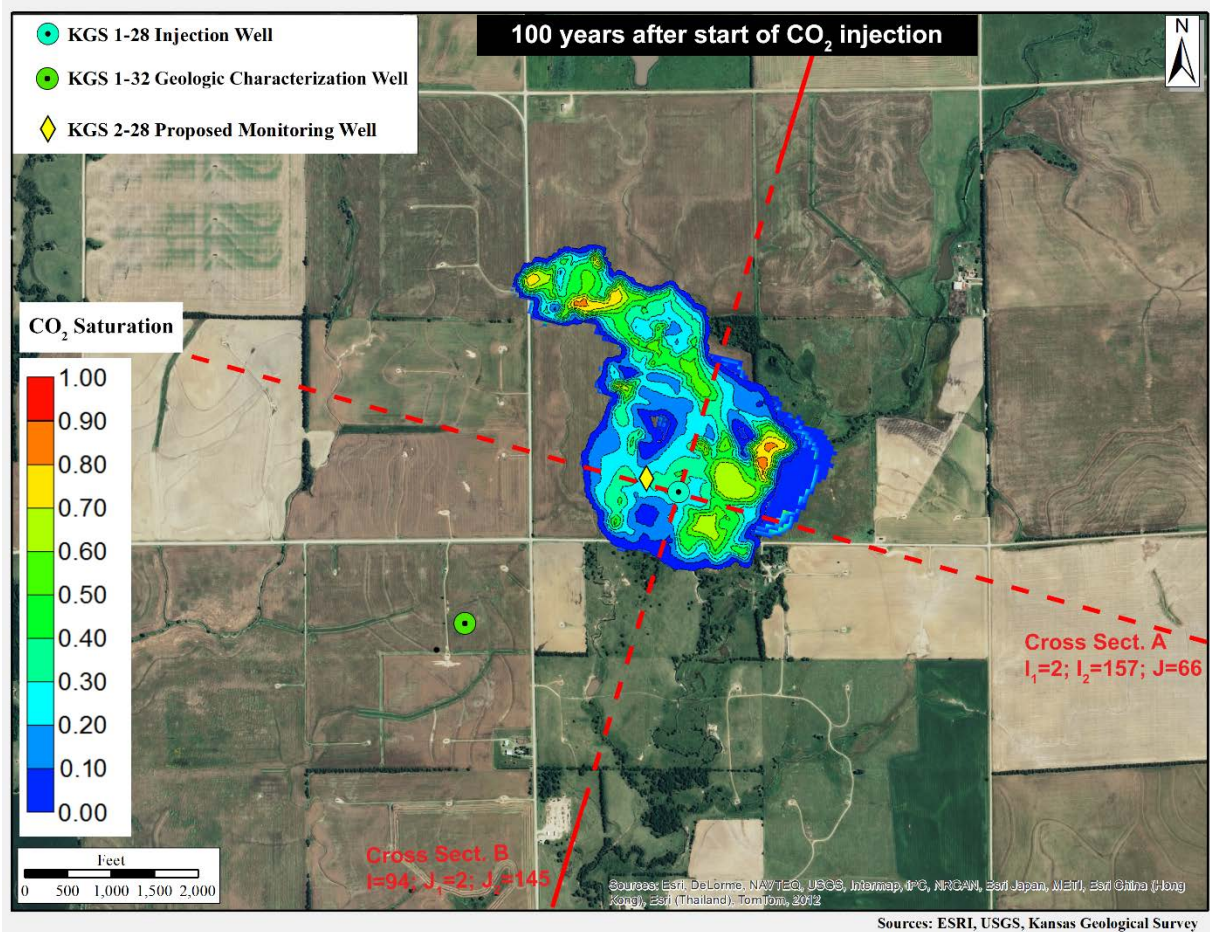
Figure 45 shows the maximum lateral migration of the CO₂ plume in the injection interval (elevation 5,010 ft) for the largest areal migration case (k-1.25/phi-0.75). The plume grows rapidly during the injection phase and is largely stabilized by the end of the second year. The plume at the end of 100 years (fig. 45) has spread only minimally since cessation of injection and has a maximum lateral spread of approximately 2,150 ft from the injection well. It does not intercept any well other than the proposed Arbuckle monitoring well KGS 2-28, which was to be constructed in compliance with Class VI injection well guidelines.

The evolution of the maximum lateral extent of the free phase plume is shown in fig. 46 for the maximum plume spread case (k-1.25/phi-0.75). The plume grows rapidly during the injection period and up to the second year from commencement of injection. Thereafter, the plume has stabilized to a maximum lateral extent of approximately 2,150 ft. The plume only intercepts the proposed Arbuckle monitoring well KGS 2-28, which was to be built to be in compliance with Class VI design and construction requirements. There are no additional natural or artificial penetrations that will allow CO₂ to escape upward from the Arbuckle injection zone.

Figure 47 shows the extent of vertical plume migration for the fast vertical migration case (k-1.25/phi-0.75), the base case (k-1.00/phi-1.00), and the high pressure case (k-0.75/phi-0.75). The free-phase plume remains confined in the injection interval (lower Arbuckle) because of the presence of the low-permeability baffle zones above the injection interval. For all three cases, the plume remains confined in the injection interval in the lower Arbuckle.

To account for uncertainties of CO₂ movement in the vertical direction, an alternate vertical permeability model was also developed in which the vertical permeability parameter was increased by 50% along with a porosity of 75% ($k=1.50/\phi=0.75$). Figure 47 presents the extent of vertical migration of the free phase plume for this case in addition to the three cases already described. The figure shows that the CO₂ migrates approximately 30 ft higher for the altered vertical permeability case, but it does not penetrate the low permeability baffle zone in the middle of the Arbuckle and stays contained within the lower Arbuckle injection zone.

The simulation results discussed above are expected to represent conservative estimates of plume migration because the present CMG simulations neglect mineral sequestration trapping. Additionally, the modeling results presented in this document do not simulate convection cells, which as demonstrated recently by Pau et al. (2010) can greatly accelerate the dissolution rate. Because of time and computational constraints, these mechanisms were ignored, and therefore the storage rates and quantities are likely to be underestimated, thus ensuring that the projections presented in this application provide a “worst-case” scenario.



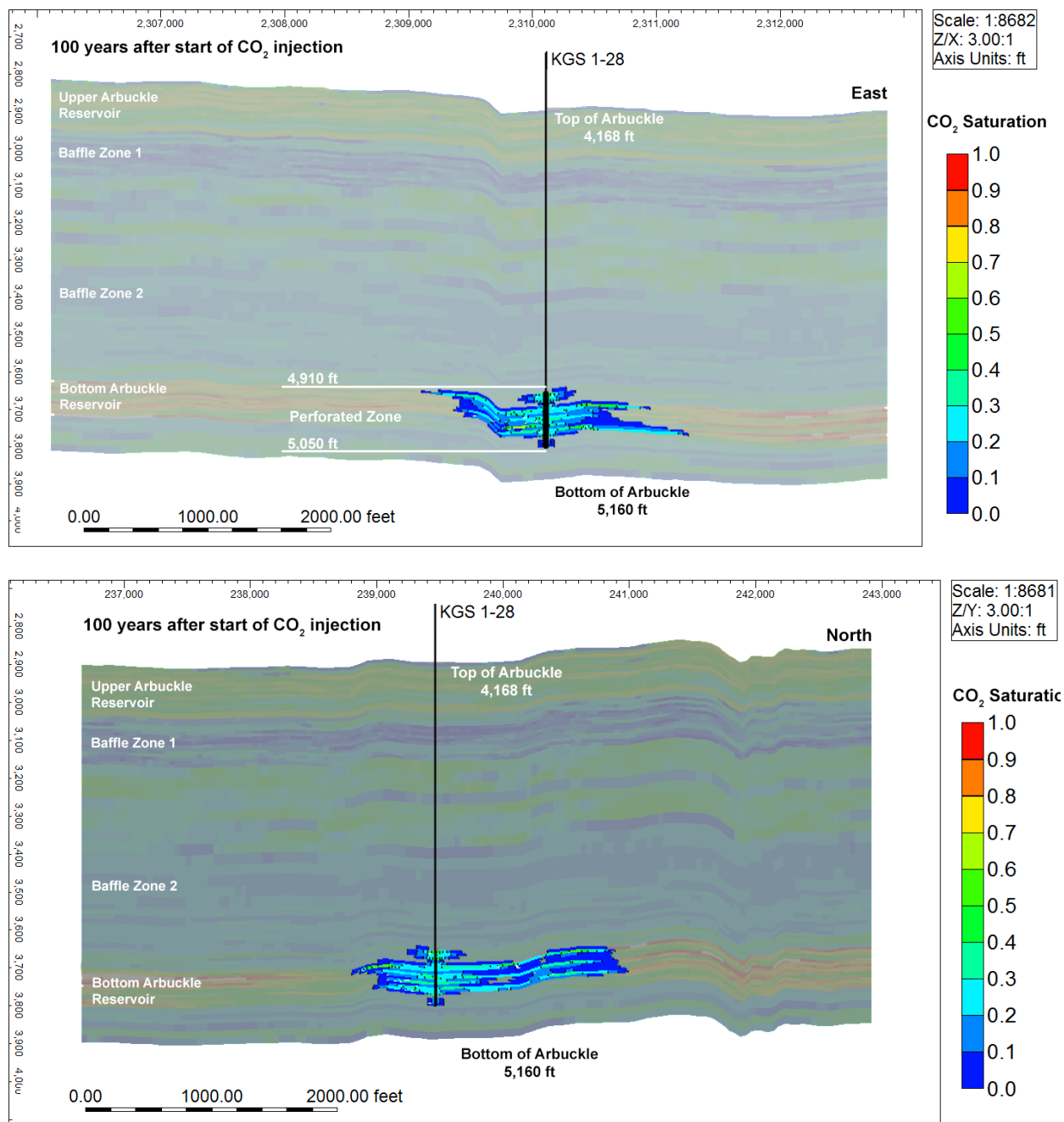


Figure 45. Free-phase CO₂ plume in aerial and cross-sectional view for the largest migration alternative model (k-1.25/phi-0.75) at 100 years from start of injection.

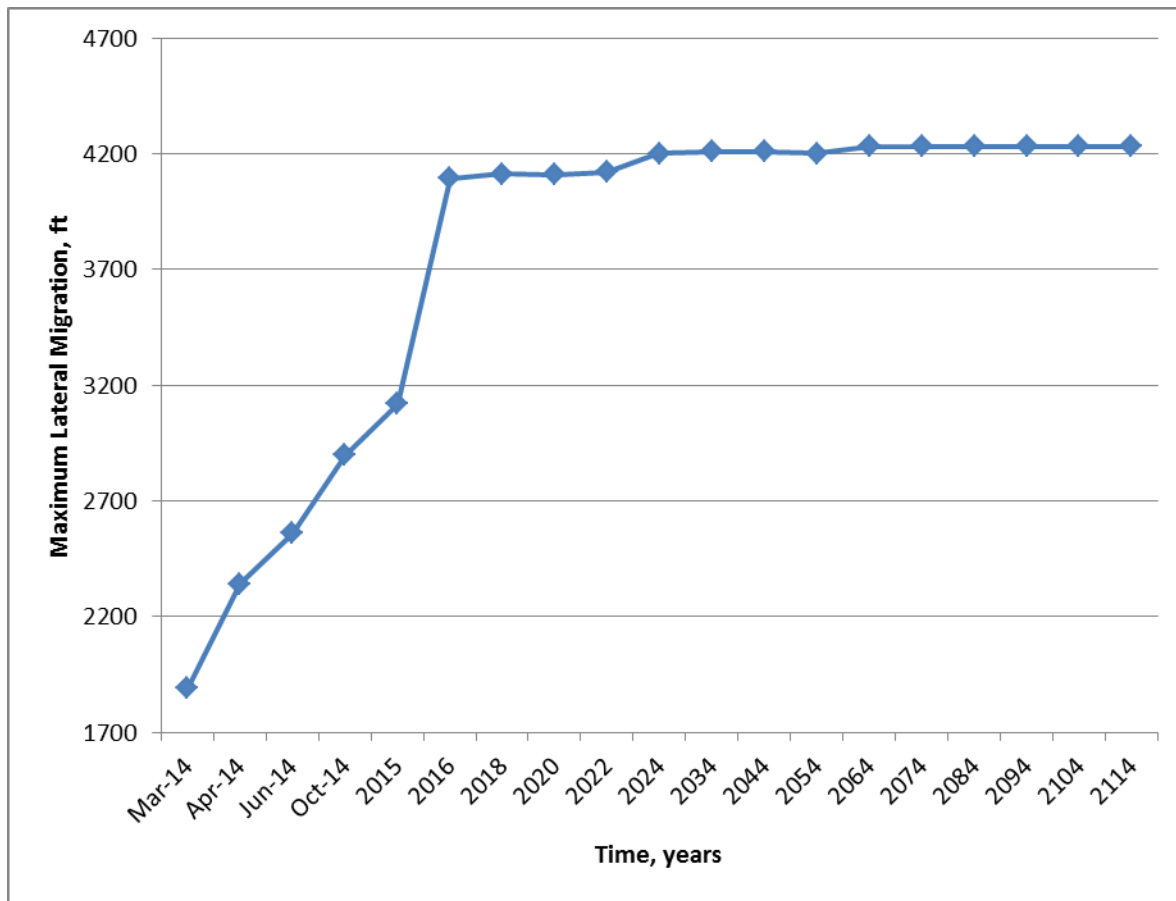


Figure 46. Maximum lateral extent of CO₂ plume migration (as defined by the 0.5% CO₂ saturation isoline) for the largest plume migration case k-1.25/phi-0.75.

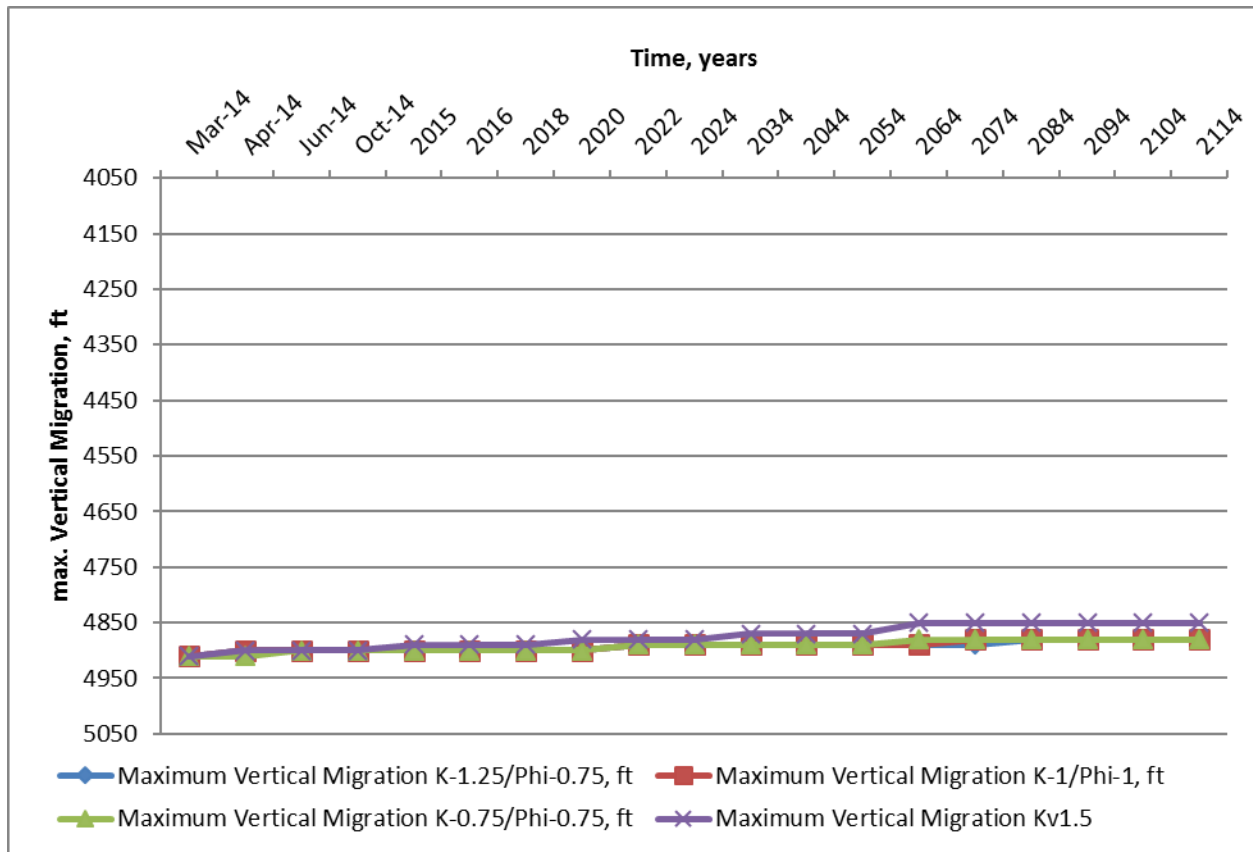


Figure 47. Maximum vertical extent of free-phase CO₂ migration for the two alternative cases that result in the maximum plume spread (k-1.25/phi-0.75) and the maximum induced pressure (k-0.75/phi-0.75) along with base case (k-1.0/phi-1.0) and vertical permeability sensitivity case (k-1.25/phi-0.75).

Simulated Pressure Distribution

Figure 48 presents the bottomhole pressure (at a reference depth of 5,050 ft) for the highest pressures alternative model (k-0.75/phi-0.75). The pressure increases to 2,485 psi upon commencement of injection and then gradually drops during the injection period as the capillary effects are overcome. The pressure decreases to pre-injection levels upon cessation of injection. The rise in pressure to 2,485 psi upon commencement of injection represents an increase of 392 psi over pre-injection levels and results in a pressure gradient of 0.515 psi/ft, which is less than the maximum allowable pressure gradient of 0.675 psi/ft corresponding to 90% of the fracture gradient (0.75 psi/ft).

Figure 49 presents the change in pore pressure at the base of the confining zone (Simpson Group) for the k-0.75/phi-0.75 alternate model that resulted in the highest pressures. The maximum pressure increase at the end of the injection period of approximately 1.15 psi is fairly small and well below the entry pressure of 956 psi for the confining zone.

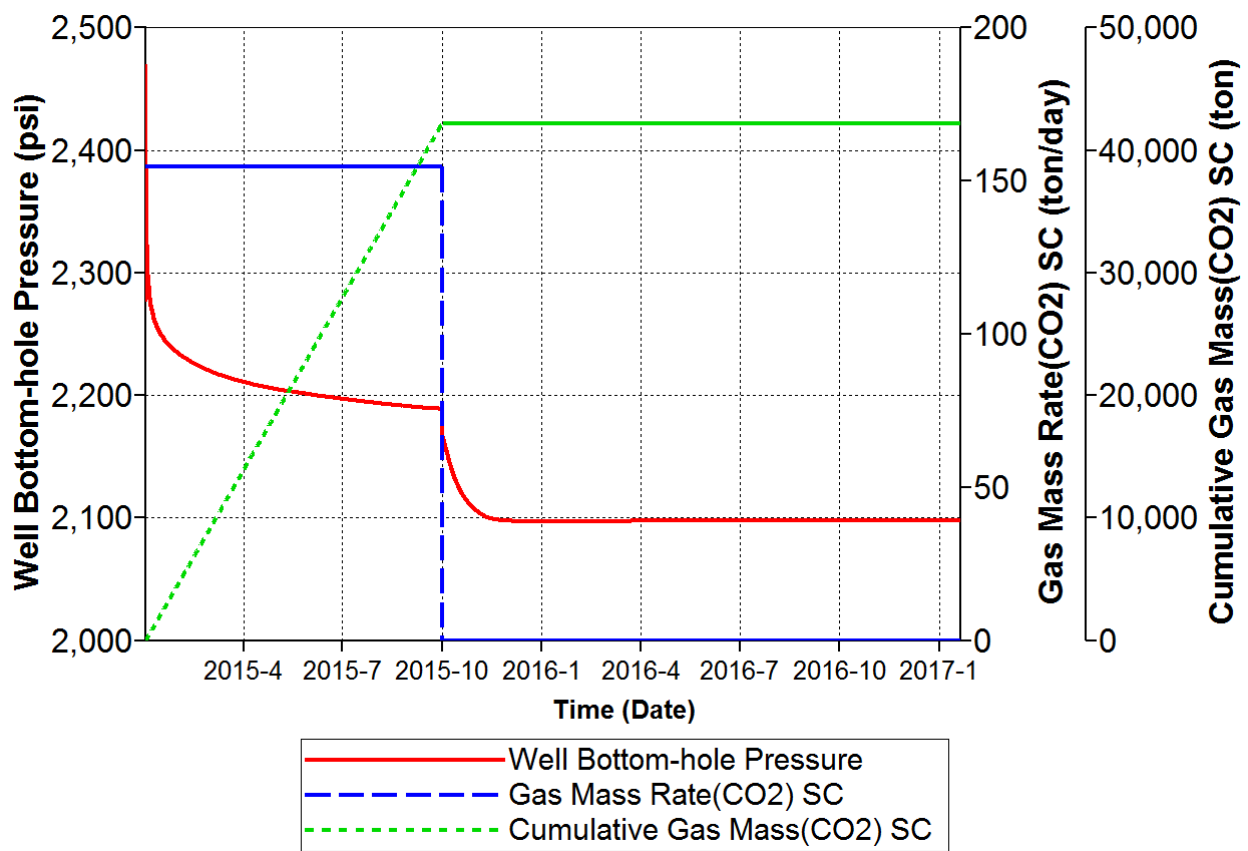


Figure 48. Maximum well bottomhole pressure at a depth of 5,050 ft for the minimum porosity and minimum permeability case ($k=0.75/\phi=0.75$).

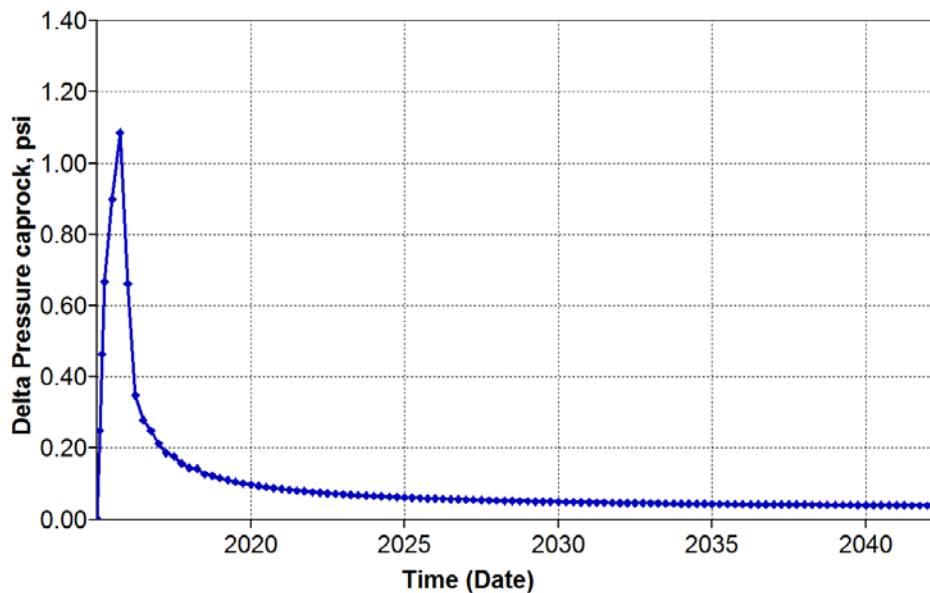


Figure 49. Change in pore pressure at the base of the confining zone (i.e., base of Simpson Group) at the injection well site for the maximum induced pressure ($k=0.75/\phi=0.75$).

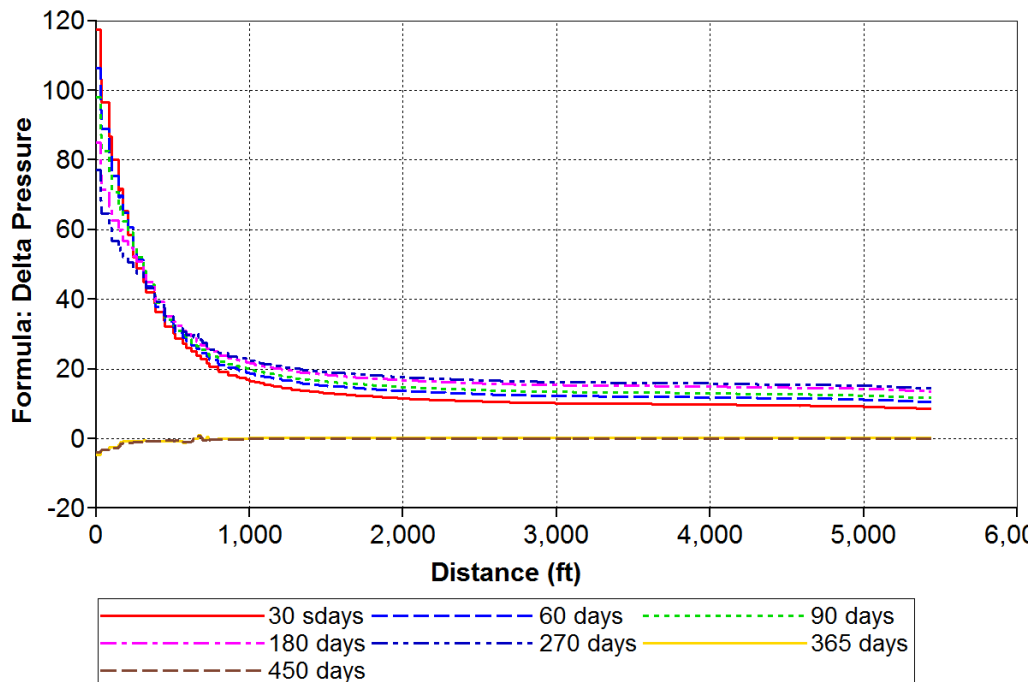
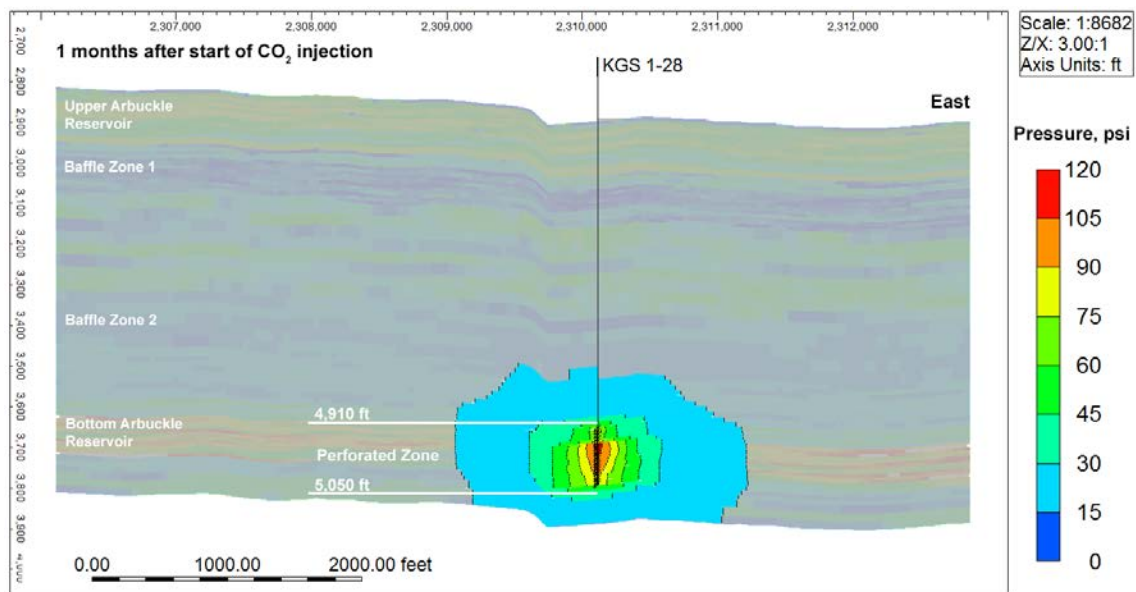
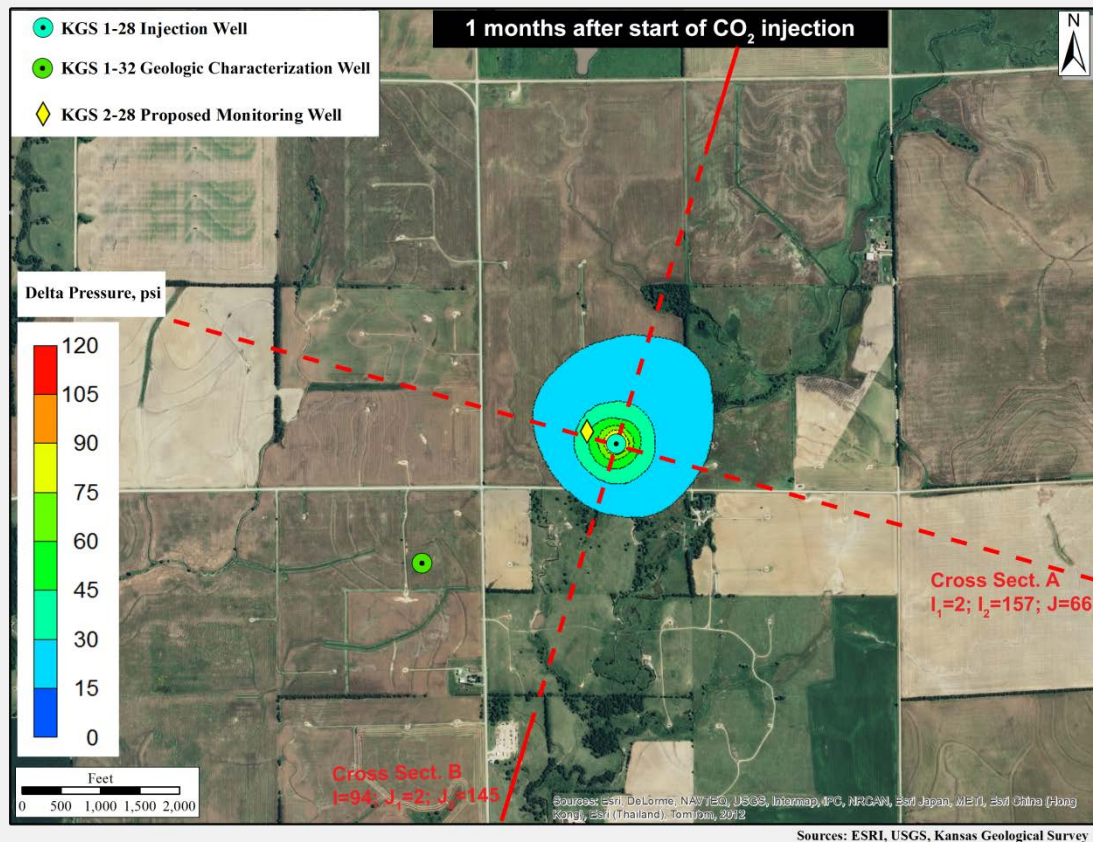


Figure 50. Pore pressure (psi) as a function of lateral distance from the injection well (KGS 1-28) at seven time intervals for the highest induced pressure case ($k=0.75/\phi=0.75$).

Figure 51 presents the lateral distribution of pressure in the Arbuckle injection interval (at an elevation of 4,960 ft) for the $k=0.75/\phi=0.75$ case, which resulted in the maximum induced pore pressures. The pressures increase from commencement of injection to nine months and then drop significantly by the end of the first year (three months after operations stop). The pressures also drop very rapidly at short distances from the injection well at the end of the nine-month injection period, as shown in fig. 50. The pressures at the end of the nine-month injection period drop from about 120 psi a short distance from the injection well to less than 15 psi at the geologic characterization well, KGS 1-32, which is approximately 3,500 ft southwest of the injection well. The maximum induced pressure at the model boundary is only 7–12 psi.

Figure 51 also shows the vertical pressure distribution for the maximum induced pressure case ($k=0.75/\phi=0.75$). The confining effect of the mid-Arbuckle baffle zones is evident in the plots as the large pressure increases are mostly restricted to the injection interval. The pressures decline rapidly at a short distance from the injection well. The pressures throughout the model subside to nearly pre-injection levels soon after injection stops.

For more detailed explanation of modeling results, see KGS Open-File Report 2016-29.



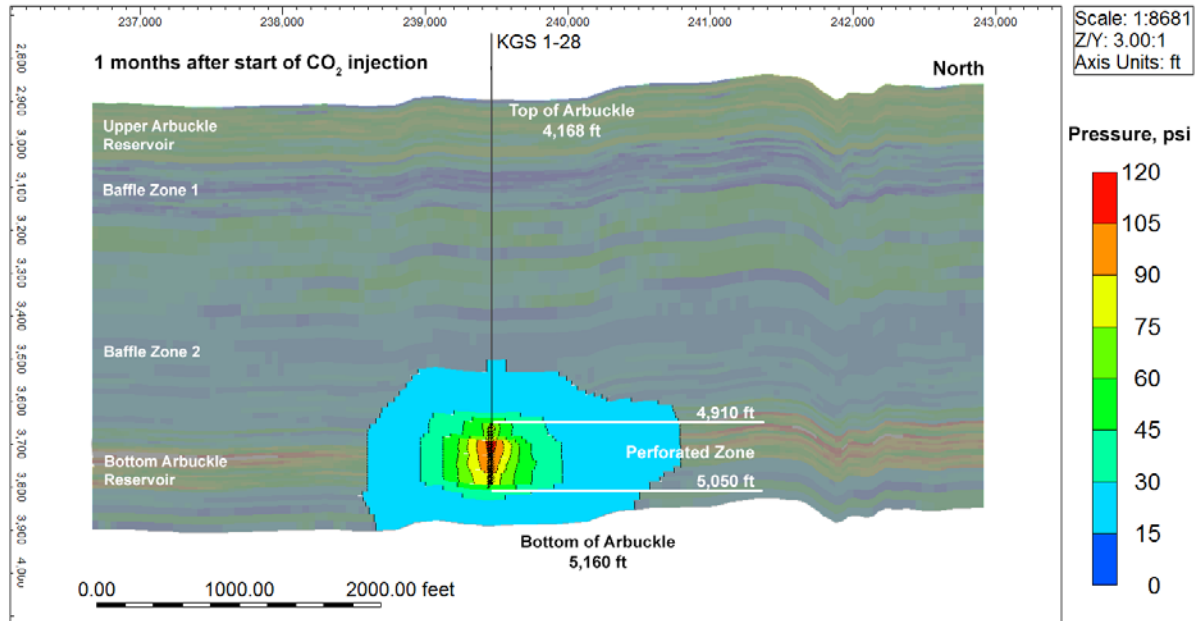


Figure 51. Simulated maximum increase in pressure in aerial and cross-sectional view at one month from start of injection for the low permeability–low porosity (k-0.75/phi-0.75) alternative case, which resulted in the largest simulated pressures.

Seismic reservoir characterization of the Mississippian and Arbuckle at Wellington Field for monitoring the injection of CO₂

The Mississippian reservoir and Arbuckle saline aquifer in Kansas are good candidates for CO₂ injection operations. The Mississippian is an oil producing reservoir that can benefit by CO₂ injection for enhanced oil recovery (EOR). The Arbuckle is an extensive, thick saline aquifer with significant potential for CO₂ storage. Both carbonate units are heterogeneous, fractured, and highly challenging to characterize reservoirs. Seismic methods have been used at other settings for reservoir characterization and CO₂ monitoring. This investigation examined the utility of active source surface seismic for characterization of Mississippian and Arbuckle reservoir properties in southern Kansas and for monitoring CO₂. In addition to the highly heterogeneous nature of carbonate reservoirs, the Mississippian thickness is below seismic resolution and the Arbuckle consists of numerous flow units, also below seismic resolution, which limit the effectiveness of conventional seismic analysis methods. This investigation used 3-D seismic imaging along with advanced analysis methods to map below-resolution reservoir thickness, porosity distribution, and fracture density and orientation. Time-lapse 2-D seismic was assessed for its ability to monitor CO₂ injected in the Mississippian reservoir. Analysis of post-stack 3-D seismic data at the Mississippian reservoir showed the response of a gradational velocity transition (ramp velocity function) where thicker reservoir units corresponded with lower reflection amplitudes, lower frequency, and a 90° phase change. Reflection amplitude was correlated to Mississippian reservoir thickness. Pre-stack gather analysis showed that porosity zones of the Mississippian and Arbuckle

reservoirs exhibit characteristic AVO response. Simultaneous AVO inversion estimated P- and S-impedances, which along with formation porosity logs and post-stack seismic data attributes were incorporated in multi-attribute linear-regression analysis and predicted reservoir porosity with an overall correlation of 0.90 to well data. The 3-D survey gather azimuthal anisotropy analysis (AVAZ) provided information about the fault and fracture network and showed good agreement to the regional stress field and well data. Mississippian reservoir porosity and fracture predictions agreed well with the observed mobility of injected CO₂ in KGS 2-32. Fluid substitution modeling predicted acoustic impedance reduction in the Mississippian carbonate reservoir introduced by the presence of CO₂. Continuing seismic data analysis at the writing of this report is evaluating the utility of time-lapse seismic for imaging injected CO₂ in the Mississippian reservoir. This work demonstrates that advanced seismic interpretation methods can be used successfully for characterization of the Mississippian reservoir and Arbuckle saline aquifer.

INTRODUCTION

Seismic imaging methods are evaluated for their effectiveness in characterizing the Mississippian reservoir and Arbuckle saline aquifer at Wellington Field in south-central Kansas. Both units are highly heterogeneous, fractured carbonates. 3-D seismic imaging along with time-lapse 2-D seismic are used to predict reservoir properties and monitor CO₂ injected in the Mississippian. Figure S-1 displays the location of Wellington seismic data. Background information about the geologic setting as well as seismic data used in this investigation is provided in the MS thesis by Sirazhiev (2012) (Appendix S-B) and the MS thesis by Fadolkarem (2015) (Appendix S-C).

Seismic data analysis methods employed for characterization of the Mississippian and Arbuckle at Wellington Field are summarized as follows:

- I. Post-stack seismic attribute analysis and impedance inversion for Mississippian reservoir thickness determination and porosity distribution prediction.
- II. Pre-stack seismic AVO (amplitude variation with offset) analysis and impedance inversion for determination of Mississippian reservoir thickness and porosity distribution, and Arbuckle flow unit delineation.
- III. Pre-stack seismic AVAZ (amplitude variation with azimuth) analysis for determination of Mississippian and Arbuckle fracture density and orientation.
- IV. Time-lapse seismic assessment of CO₂ injection in the Mississippian reservoir.

Key Findings

- A gradational porosity decrease at the top of the Mississippian reservoir corresponds to a gradational P-wave velocity increase.
- A gradational or “ramp” velocity function results in the integral of the seismic wavelet with lower amplitude, lower frequency content and a 90 degree phase shift corresponding to thicker reservoir zones.
- The characteristic seismic amplitude response of the top of the Mississippian is used to predict reservoir thickness when true thickness is $1/16\lambda$ – $5/16\lambda$ (16–82 ft; 5–25 m) (λ = wavelength).
- Post-stack model-based acoustic impedance inversion provides reliable porosity predictions for reservoir thickness range of $1/8\lambda$ – $7/16\lambda$ (32–115 ft; 10–35 m).

Background

Mississippian chert reservoirs are important hydrocarbon resources in North America. These reservoirs are highly heterogeneous, typically below seismic resolution and, therefore, present a challenging task for predicting reservoir properties from seismic data (e.g. Mazzullo et al., 2009; Montgomery, 1998; Rogers and Longman, 2001; Watney et al., 2001).

In this study, we conducted post-stack seismic attribute analysis of the Mississippian chert reservoir at the Wellington Field, south-central Kansas, using well-log and 3-D PSTM seismic data. The microporous cherty dolomite reservoir exhibits a characteristic vertical gradational porosity reduction and associated increase in acoustic velocity, known as a ramp-transition velocity function. The primary objective of this study was to investigate possible relationships of the reservoir thickness and porosity with post-stack seismic attributes, including inverted acoustic impedance.

Methods

We examined the seismic response of a ramp-transition velocity function to predict the thickness of the Mississippian chert reservoir. The Mississippian top is characterized by a vertical gradational porosity decrease and a corresponding ramp velocity increase that results in a gradational impedance increase (fig. S-2). We employed seismic wedge modeling using both synthetic and original sonic logs to aid the interpretation and investigate the resolution limits of the seismic data. A characteristic amplitude decrease and wavelength increase (frequency decrease) is observed at the top of the Mississippian as reservoir thickness increases (fig. S-3). Seismic amplitude is shown to reliably predict reservoir thickness in the range of 16-82 ft (5-25 m).

Post-stack model-based inversion of the seismic data was used to derive the acoustic impedance model of the subsurface. The resolution of the model-based inversion was evaluated for the case of the gradational impedance increase within the Mississippian reservoir interval using synthetic wedge models (Figure S-3). Multilinear regression analysis is used to transform the inverted acoustic impedance to porosity distribution within the Mississippian reservoir. The reliability of the predicted porosity model is tested by cross-validation during the multilinear regression analysis.

Results

The analysis of well log and seismic data revealed that the reservoir exhibits different characteristics across fault #1 which divides the Wellington Field diagonally from the southwestern corner to the northeastern corner.

The reservoir in the southeastern part of the field is characterized by a vertical gradational porosity decrease (from 25–30% to 4–6%), variable thickness (20–66 ft; 6–20 m), lower seismic amplitude and frequency content and a locally developed double reflector. In addition, a high correlation between seismic amplitude and reservoir thickness conformable with the theoretical amplitude response of a ramp-transition velocity function is observed. The amplitude envelope was used to predict the reservoir thickness in this part of the field (Figure S-4).

The Mississippian reservoir in the northwestern part of the field has more heterogeneous porosity distribution within the reservoir interval, thins in the north-north-west direction, while no clear relationship was found between reservoir thickness and instantaneous seismic attributes.

The model-based inversion result and predicted porosity model supported the well-log and seismic attribute interpretation (Figure S-5). The reliability of the predicted porosity model is tested by cross-validation. Resolution limits were determined as $1/16\lambda$ for the amplitude envelope attribute and $1/8\lambda$ for the model-based inversion within the Mississippian reservoir characterized by a vertical gradational porosity reduction.

Results of this research could benefit the characterization of similar chert as well as clastic and carbonate reservoirs characterized by downward porosity reduction. In addition to predicting the reservoir porosity and thickness, the seismic response of a ramp-transitional velocity function related to downward porosity reduction might be useful in understanding depositional and diagenetic histories of such reservoirs.

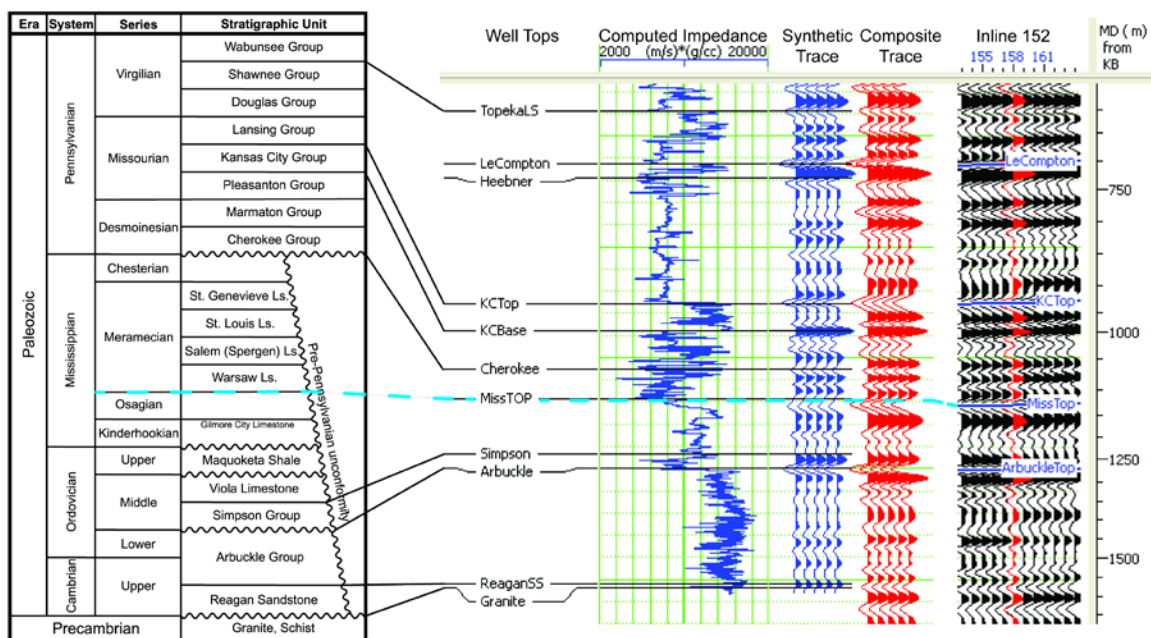


Figure S-2: From left to right: generalized stratigraphic section of central Kansas (modified from Nissen et al. (2009), originally from Cansler (2000)); well tops, computed impedance log, synthetic (blue) and seismic (red) traces at well #15-191-22591; part of inline #152. The Mississippian reservoir top is identified by the blue dashed line.

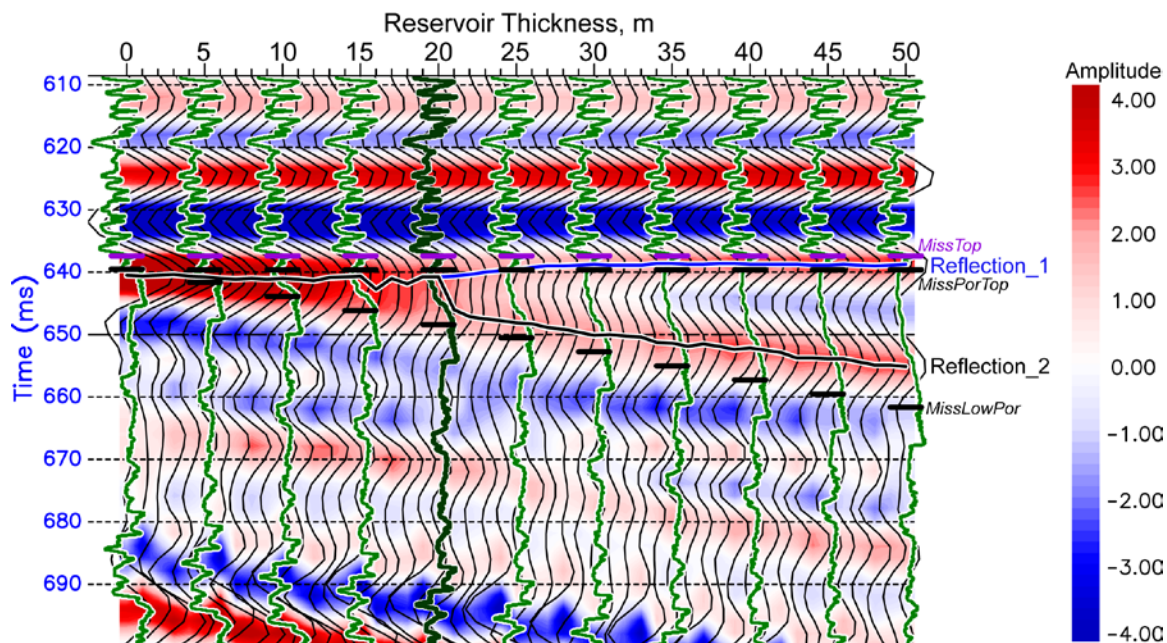


Figure S-3: Synthetic seismic section of the reservoir wedge model constructed at well #15-191-22591. Original sonic log is shown in dark green (corresponds to reservoir thickness of 20 m). Synthetic sonic logs calculated by stretching and squeezing the original log within the Mississippian reservoir are shown in light green for every 5th trace.

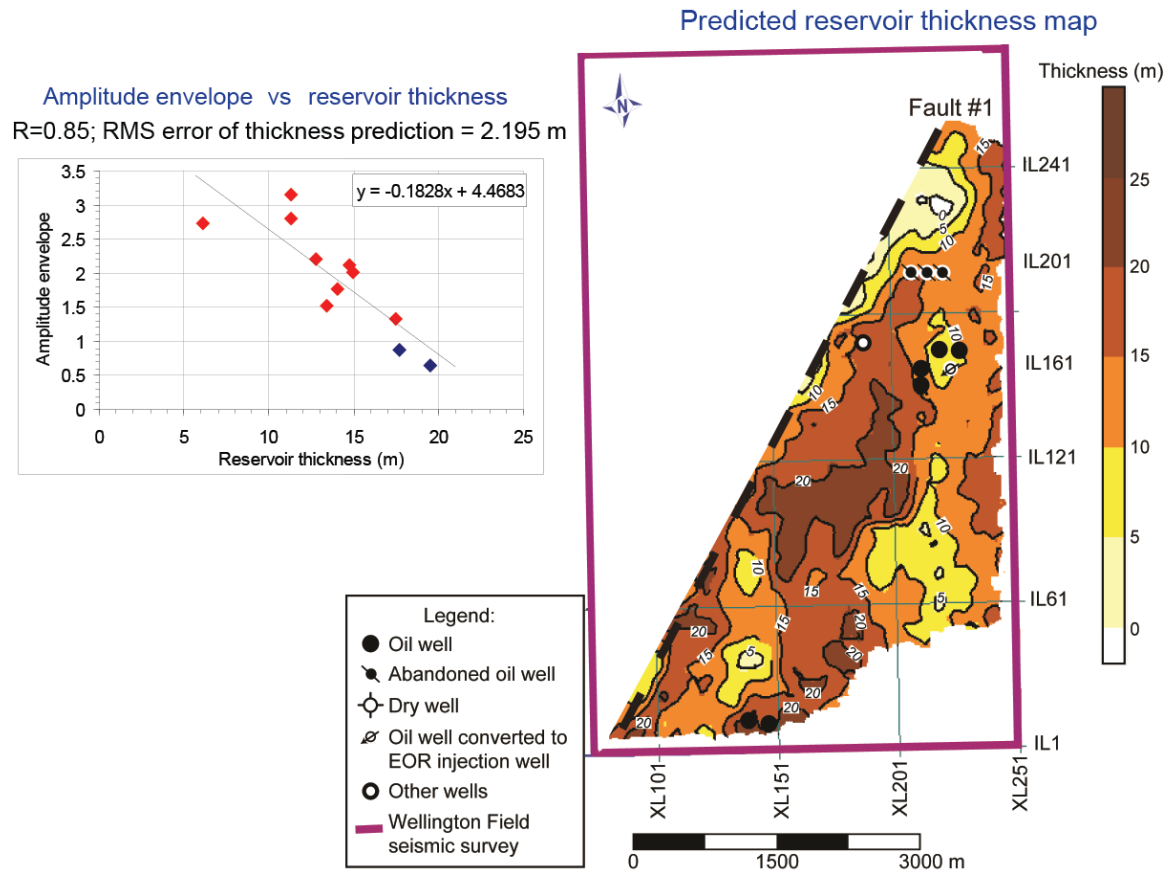


Figure S-4: (left) Crossplot of amplitude envelope of the Mississippian top horizon averaged around well locations within nine closest traces versus the Mississippian reservoir thickness. (right) Map of the thickness of the Mississippian reservoir at the Wellington Field predicted from the amplitude envelope.

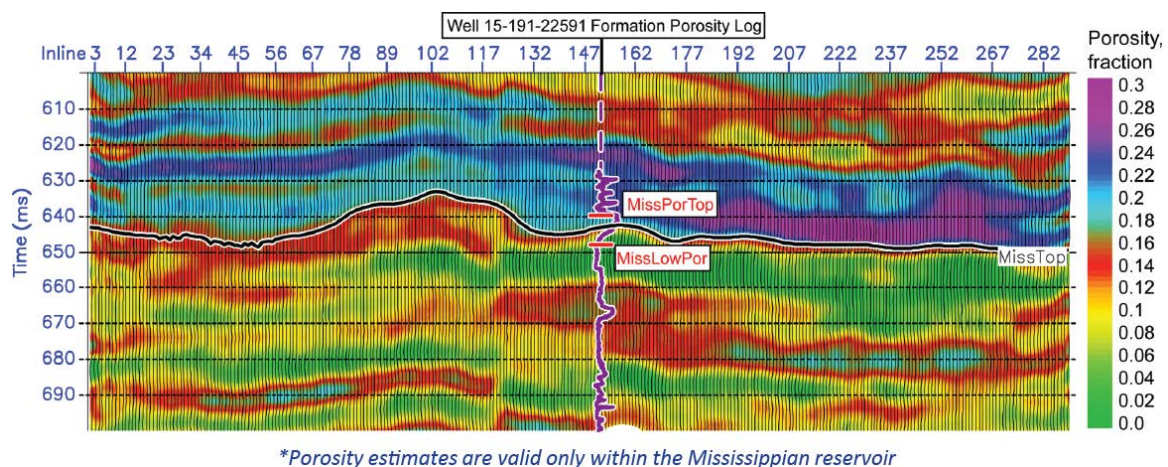


Figure S-5: Result of the formation porosity prediction from the inverted impedance volume across the inline #152 with overlain original formation porosity log at well #15-191-22591.

II. Pre-stack seismic AVO analysis and impedance inversion for determination of Mississippian reservoir thickness and porosity distribution, and Arbuckle flow unit delineation

For a detailed description, refer to the MS thesis by Fadolkarem (2015) (Appendix S-C).

Key Findings

- High porosity zones in the Mississippian and the Arbuckle Group exhibit characteristic AVO (amplitude variation with offset) response.
- AVO classification can be employed to identify the porous zones at Wellington Field 3-D volume using the intercept-gradient cross plotting technique.
- Simultaneous AVO impedance inversion results in improved estimation of Mississippian reservoir and the Arbuckle Group properties than model-based inversion of post-stack data.
- The resolution limit of simultaneous AVO inversion within the Mississippian chert reservoir was determined using wedge modeling at 32 ft (10 m), which corresponds to 1/8 of a wavelength.
- Flow units in the Arbuckle are mapped using AVO analysis and Simultaneous AVO impedance inversion.
- Multi-Attribute Linear Regression Analysis porosity predictions benefit by incorporating P- (Z_P) and S-impedance (Z_S) data obtained from simultaneous AVO inversion of pre-stack seismic gathers.
- Best porosity prediction at the Mississippian reservoir is achieved when the multi-attribute transform is constrained within the Mississippian reservoir.
- Optimum porosity prediction at the Arbuckle is achieved when the multi-attribute transform is derived between the Cherokee Group top (above Arbuckle) and the Reagan Sandstone top (Arbuckle base) using the 11 wells that have formation porosity logs, including the wells that did not penetrate the Arbuckle Group.
- The Mississippian reservoir thins to the northwest. The deeper Arbuckle Group has five main low impedance and high porosity zones that are deeper in the eastern and southeastern parts of the Wellington Field.

Background

In this study, we conduct pre-stack seismic analysis of the Mississippian reservoir and the Arbuckle Group at the Wellington Field, south-central Kansas, using 3-D pre-stack migrated seismic gathers. We examine pre-stack seismic attributes on both real and synthetic seismic data to identify the porous reservoir zones and to determine whether using pre-stack seismic data for porosity prediction can improve the reservoir characterization. Specifically, we examine the utility of AVO analysis and impedance inversion for characterization of the Mississippian and Arbuckle reservoirs. We also evaluate the use of multi-attribute regression for porosity prediction in the two reservoirs. This work helps advance the understanding of the capabilities and limitations of pre-stack seismic methods for reliably predicting Mississippian reservoir thickness and porosity and for mapping flow units in the Arbuckle.

The Mississippian reservoir is a microporous cherty dolomite reservoir that exhibits downward gradational porosity decrease resulting in a corresponding increase in velocity. It is typically thin (50 ft, 15 m) and below seismic resolution. The deeper Cambrian-Ordovician Arbuckle Group is a thick succession of interbedded dolomudstones, pack-grainstones, vuggy brecciated zones, and thin dolomudstone and shale beds (Watney et al., 2013). The Arbuckle aquifers are highly heterogeneous and compartmentalized with individual reservoir units below seismic resolution. Therefore, it is challenging to identify reservoirs or predict their properties from the seismic data (Franseen et al., 2003; Watney et al., 2001).

Methods

In this study, we investigate the AVO response of the Mississippian reservoir and the porous zones of Arbuckle Group. We examine whether the AVO classification can be used for identifying the porous zones at Wellington Field in both the Mississippian and the Arbuckle. Also, we perform simultaneous AVO inversion of the pre-stack migrated gathers for prediction of P-wave impedance (Z_P), S-wave impedance (Z_S) and density (ρ), and compare results to previous post-stack model-based inversion. The resolving power of the resulting inversion volumes is evaluated by correlating the inversion results with real well log data.

We also test the utility of multi-attribute transforms for reservoir porosity prediction. We incorporate inverted P-impedance (Z_P) and S-impedance (Z_S) obtained from pre-stack simultaneous AVO inversion, formation porosity well logs and post-stack seismic data in a multi-attribute linear-regression analysis to derive multi-attribute transforms that are used to predict porosity values in the seismic survey volume of the Wellington Field. The reliability of porosity prediction is tested by blind wells that are excluded from the analysis. Also, the porosity prediction is evaluated by correlating predicted porosity traces with formation porosity well logs.

Results

i) Mississippian and Arbuckle Reservoir AVO Classification

Porosity zones of the dolomitic reservoirs in both the Mississippian and the Arbuckle Group are shown to exhibit Class IV AVO response (Figure S-6a), which is characterized by negative intercept (A) and positive gradient (B) leading to A-B crossplots located in the fourth quadrant (Figure S-6b). This AVO classification was employed to identify and delineate the porous zones in the Wellington Field 3-D seismic.

AVO analysis was conducted using A-B cross plotting over the time window between the top of the Arbuckle horizon and the basement horizon. Fourth quadrant Class IV cross plot points highlighted by the red polygon shown in figure S-6b correspond to regions marked by red color in the seismic section shown in figure S-6c. Those red highlighted zones (identified by arrows) are high porosity zones as confirmed by the porosity log at well #15-121-22591. The high porosity zones in the Arbuckle Group have been correlated to distinct flow units. Therefore, AVO analysis is shown to be capable of delineating porous intervals that form flow units across the Arbuckle Group.

AVO analysis employed at the Mississippian shows that Class IV AVO response corresponds to the porous reservoir section, as confirmed by well data (Figure S-7).

ii) Pre-stack Seismic Inversion (Simultaneous AVO Inversion)

Simultaneous AVO inversion uses pre-stack gathers to invert simultaneously for P- and S-impedance and density (Hampson et al., 2005). The inverted P-impedance (Z_p) by simultaneous AVO Inversion showed better correlation with the real P-impedance from well logs, and lower RMS inversion error compared to post-stack model-based inversion conducted previously (Sirazhiev, 2012). Figure S-8 shows a comparison of seismic inversion results with measured properties at well #15-121-22591.

At the Arbuckle Group, five main low-impedance, high-porosity zones are observed. The low impedance zones in the inverted P-impedance volume show good contrast with the surrounding higher impedance zones, which allows mapping their extent across the Wellington Field (Figure S-9). Distinct flow units identified in the Arbuckle correlate spatially with the low P-impedance zones, therefore impedance can be used to map delineate flow units at the Arbuckle (Figure S-9).

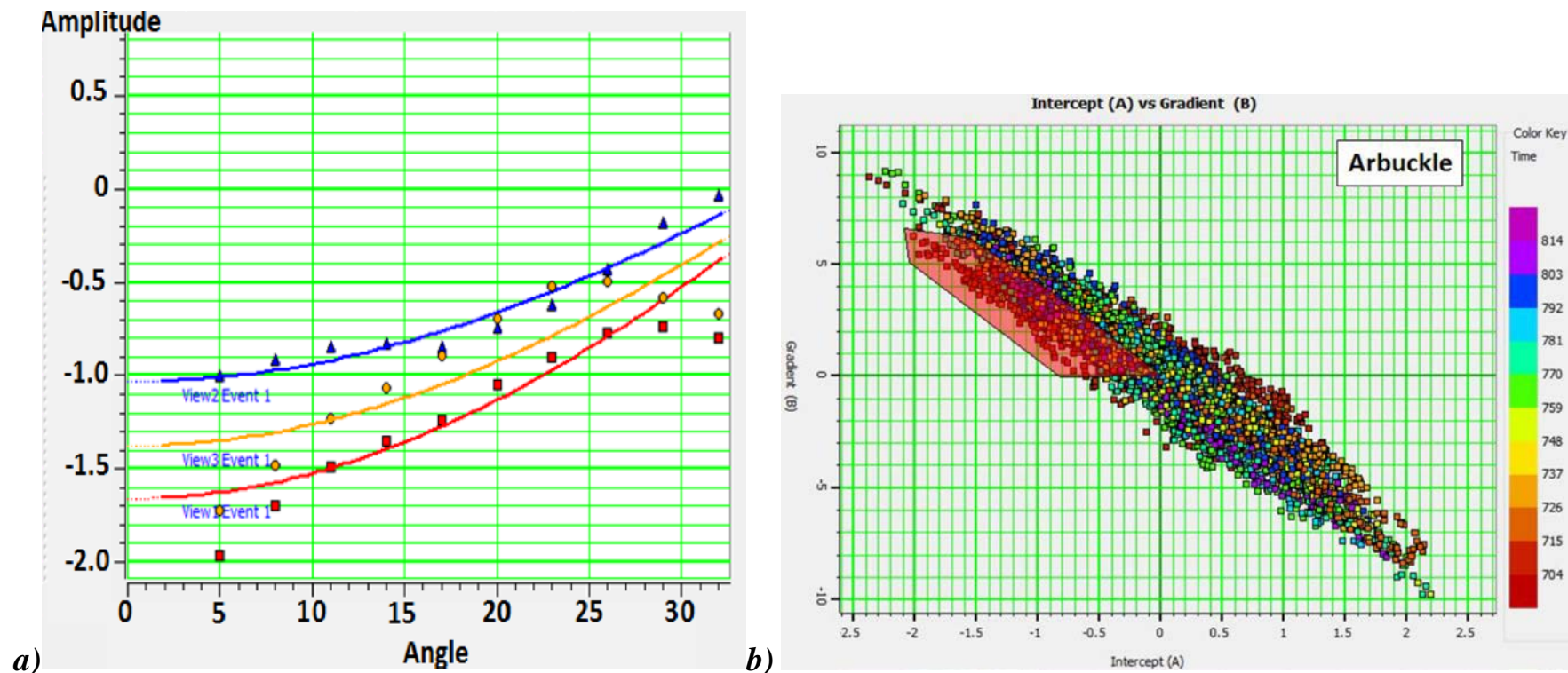
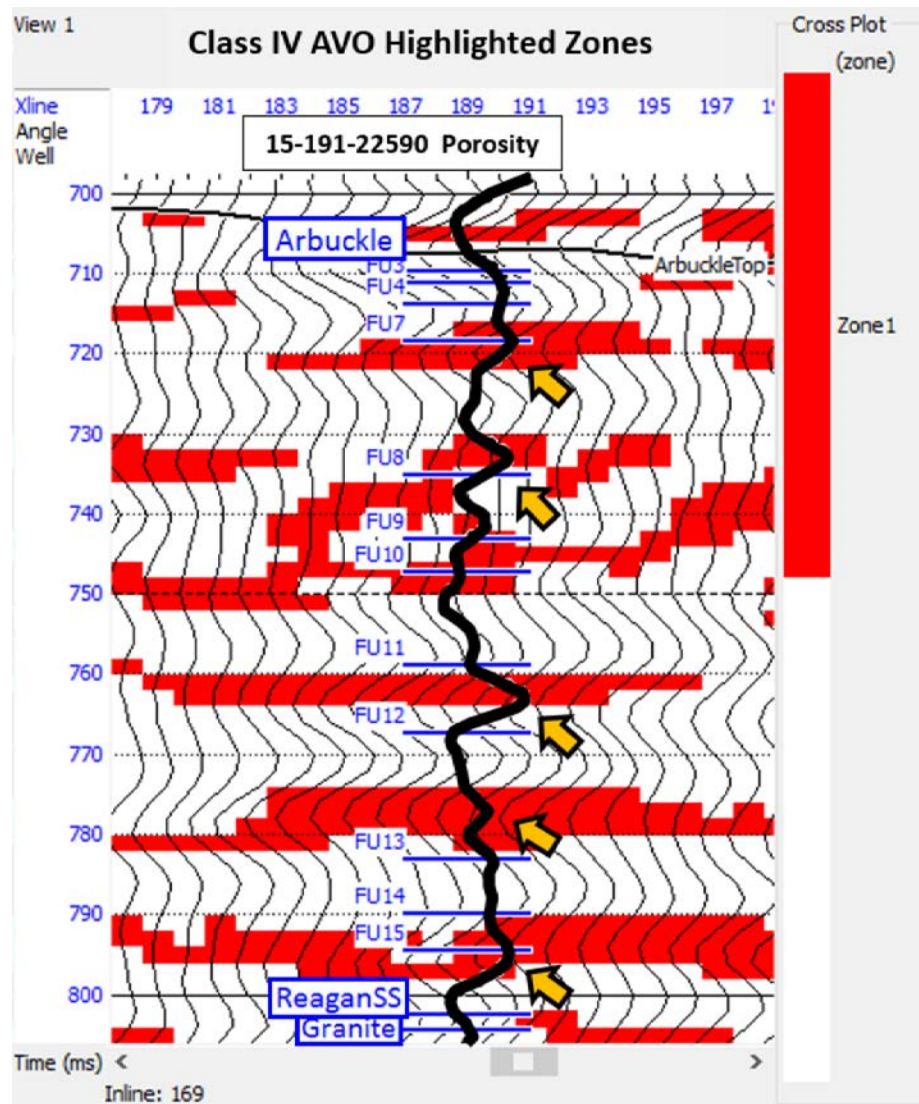


Figure S-6: Arbuckle AVO analysis. a) Amplitude extracted from seismic angle gathers at wells #15-121-22591, #15-121-22590, and #15-121-20789 with trend lines indicating Class IV AVO response. b) A-B crossplots with the red polygon highlighting Class IV AVO response.



c)

Figure S-6 (continued from previous page): Arbuckle AVO analysis. c) Class IV AVO highlighted zones on Inline #152 that correspond to the A-B cross plots highlighted by the red polygon in figure S-6b.

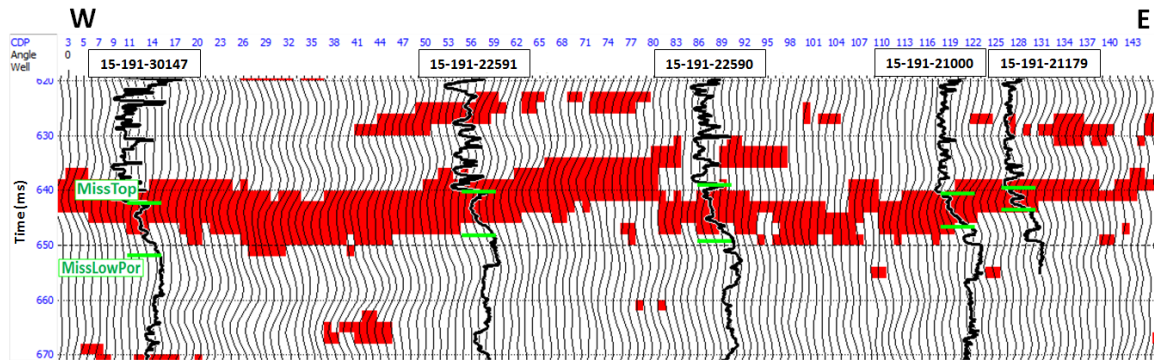


Figure S-7: Mississippian AVO analysis. Class IV AVO highlighted zones (red) on seismic data displayed along with porosity logs at the Mississippian reservoir. AVO highlighted zones are in good agreement with reservoir porous zones.

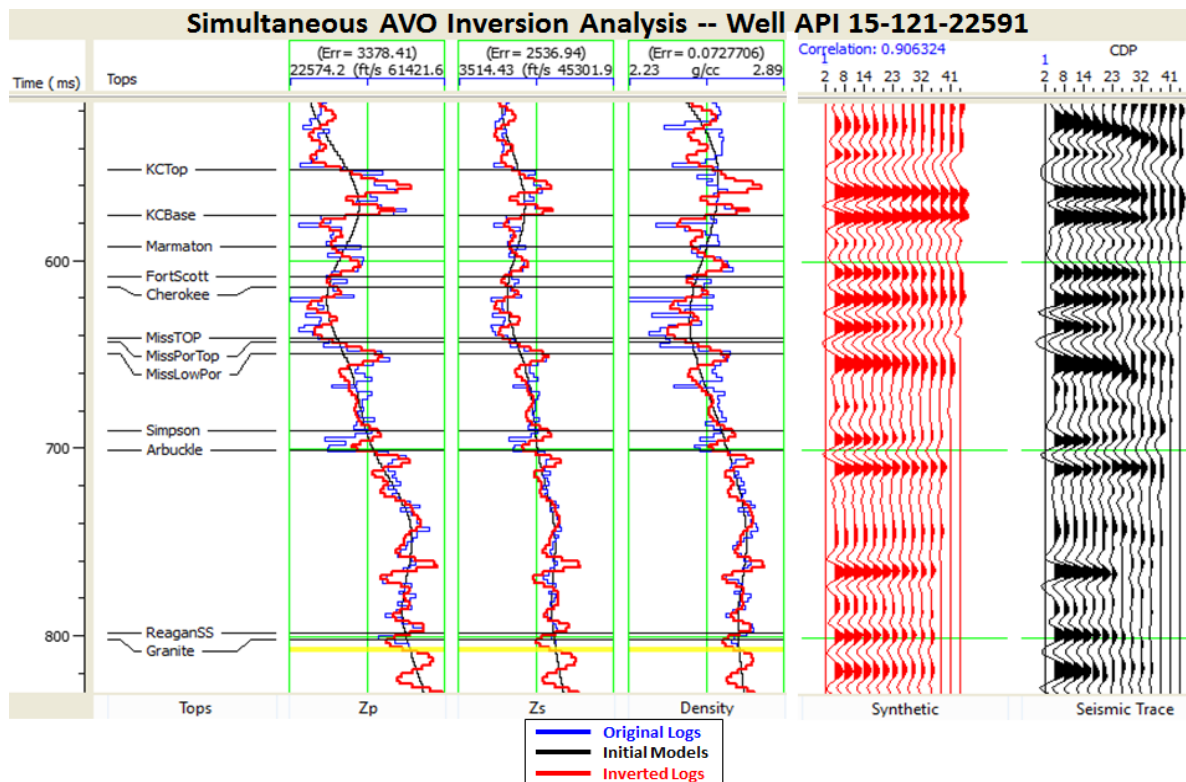


Figure S-8: Analysis of simultaneous AVO inversion at well location #15-191-22591. From left to right: 1) Well tops. 2) Inverted traces (red), original well logs (blue), and initial models (black) of Z_p , Z_s , and density. 3) Synthetic seismic gather (red). 4) Real seismic gather (black). The inverted traces (red) show a good match with the original logs (blue). The synthetic seismic gather shows a high correlation of 0.91 with the real seismic gather (black) at the well location.

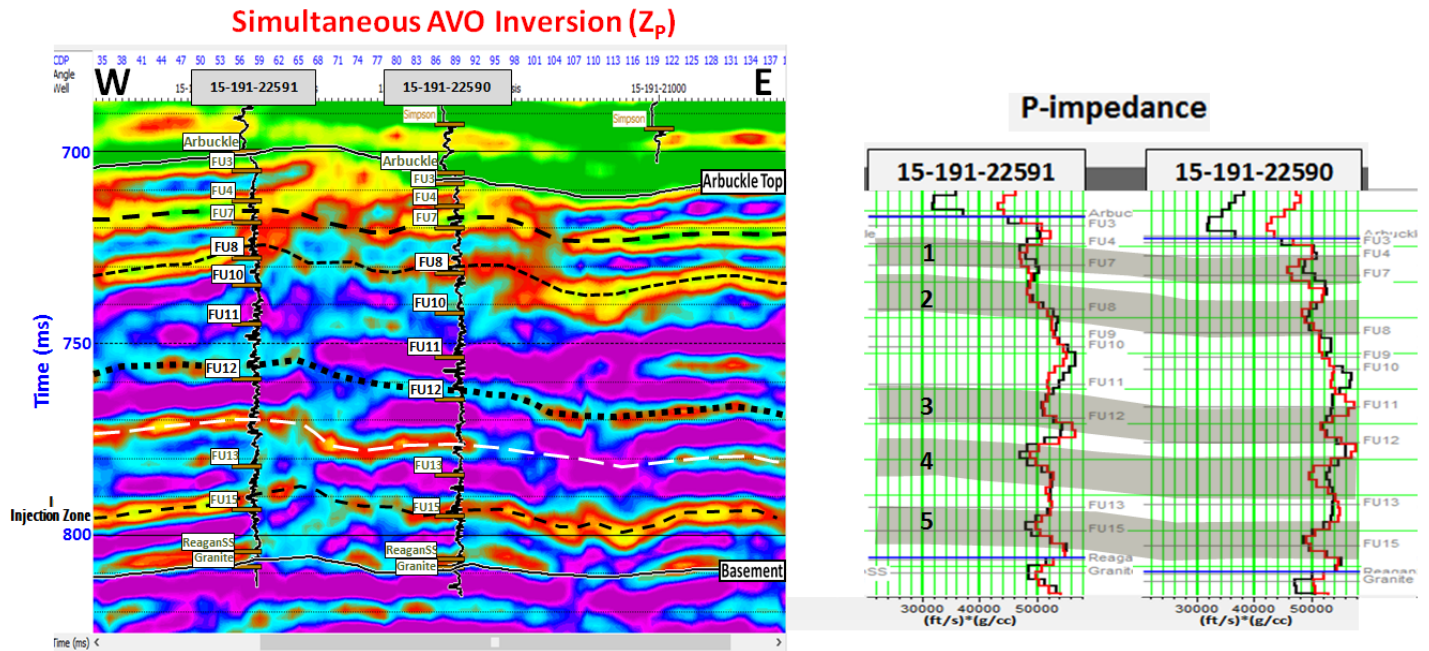


Figure S-9: Arbuckle flow unit identification. (left) Simultaneous AVO inverted Z_p cross section. Five low impedance zones are picked by the dashed lines. (right) Measured P-impedance logs (Black) from wells #15-121-22590 and #15-121-22591, and the inverted P-impedance traces (Red) at the two well locations. Five distinct low impedance zones shaded in grey correspond to Arbuckle flow units.

iii) *Mississippian Reservoir Porosity Prediction* (multi-attribute linear-regression analysis)

Porosity prediction within the Mississippian reservoir is achieved when the multi-attribute transform is derived only within the Mississippian reservoir. The multi-attribute transform in this case does not provide meaningful porosity values outside the Mississippian reservoir but it shows great contrast between the Mississippian reservoir and the surrounding formation, which helps in delineating the Mississippian reservoir around the seismic volume. Figure S-10 shows good agreement between predicted porosity logs (red curves) and original porosity logs (black curves) within the Mississippian reservoir with an overall cross correlation of 0.90. Figure S-11 displays predicted porosity profiles from seismic data along with porosity logs exhibiting good agreement. A map of Mississippian reservoir porosity is shown in Figure S-12.

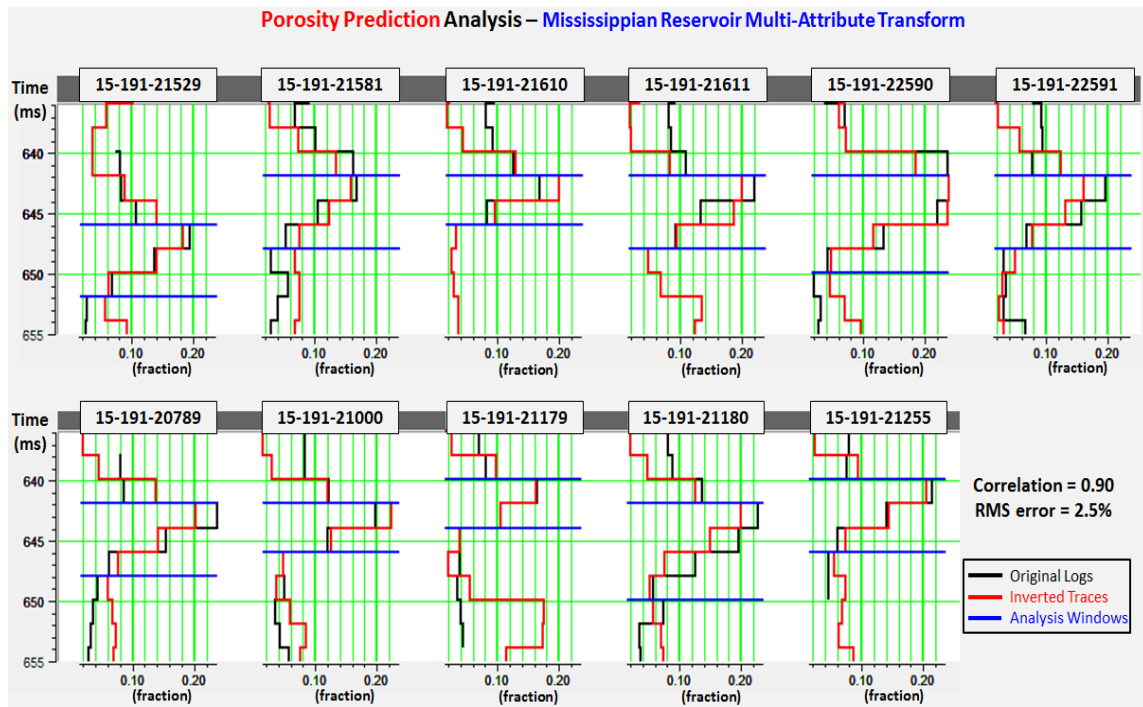


Figure S-10: Analysis of the predicted porosity by the multi-attribute transform within the Mississippian reservoir (blue horizontal lines define the analysis window) at 11 well locations. The predicted porosity traces (red) show a good agreement with the original formation porosity logs (black) with an overall correlation of 0.90 for all wells.

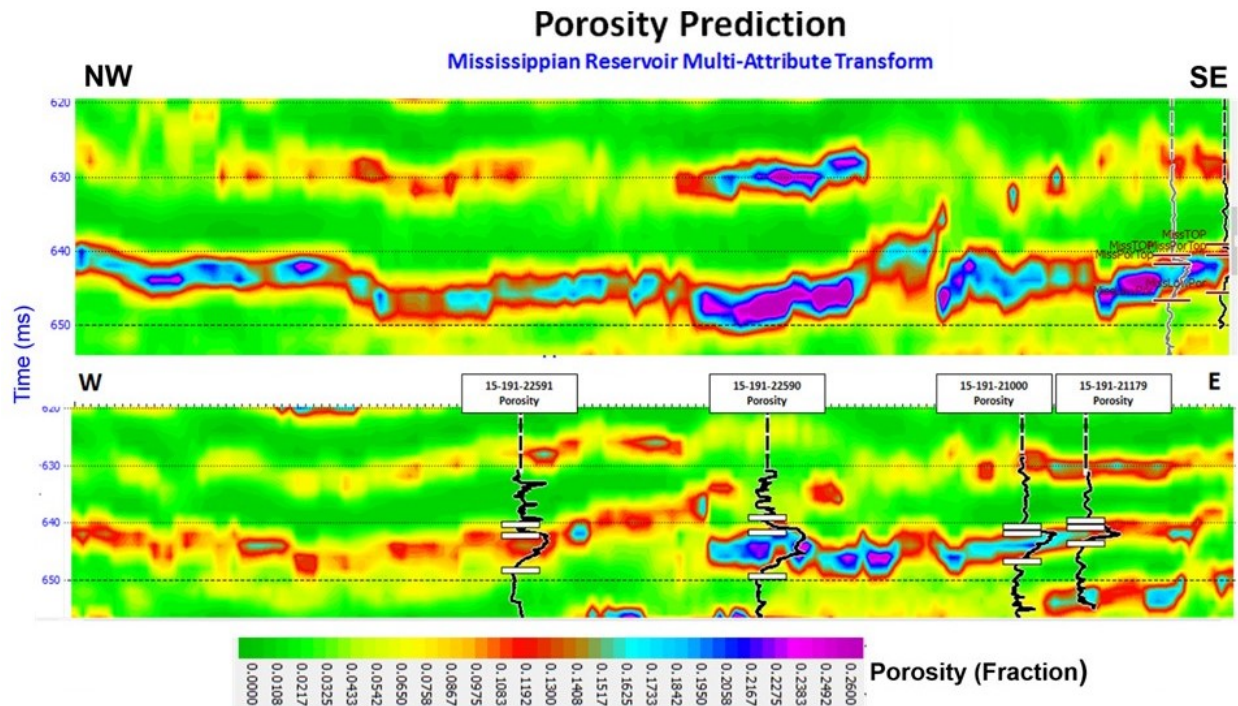


Figure S-11: (upper) NW-SE cross section of predicted porosity at the Mississippian reservoir showing thinning to the NW. (lower) E-W cross section of predicted porosity. Porosity well curves are displayed over the predicted porosity profiles showing good agreement.

iv) Arbuckle Reservoir Porosity Prediction

At the Arbuckle Group, a multi-attribute transform derived within the Arbuckle interval only provided good porosity prediction at the two well locations that penetrated the Arbuckle, but it did not provide reasonable porosity values away from the two wells. This may be due to limited well control within the Arbuckle. Unlike the Mississippian reservoir, the optimum porosity prediction quality within the Arbuckle was achieved when the multi-attribute transform was derived between the Cherokee Group top (above Arbuckle) and the Reagan Sandstone top (Arbuckle base) using the 11 wells that have formation porosity logs including the wells that did not penetrate the Arbuckle Group. The Arbuckle Group has five main low impedance and high porosity zones that are deeper in the eastern and southeastern parts of the Wellington Field (Figure S-13). The depth change of the five zones is attributed to the post-Mississippian SW-NE trending normal fault. The resultant porosity prediction volume shows good agreement with the results of A-B cross plotting technique for both the Mississippian and the Arbuckle. Class IV AVO zones highlighted by the A-B cross plotting technique correlate with high porosity values in the porosity prediction volume. (Figure S-13).

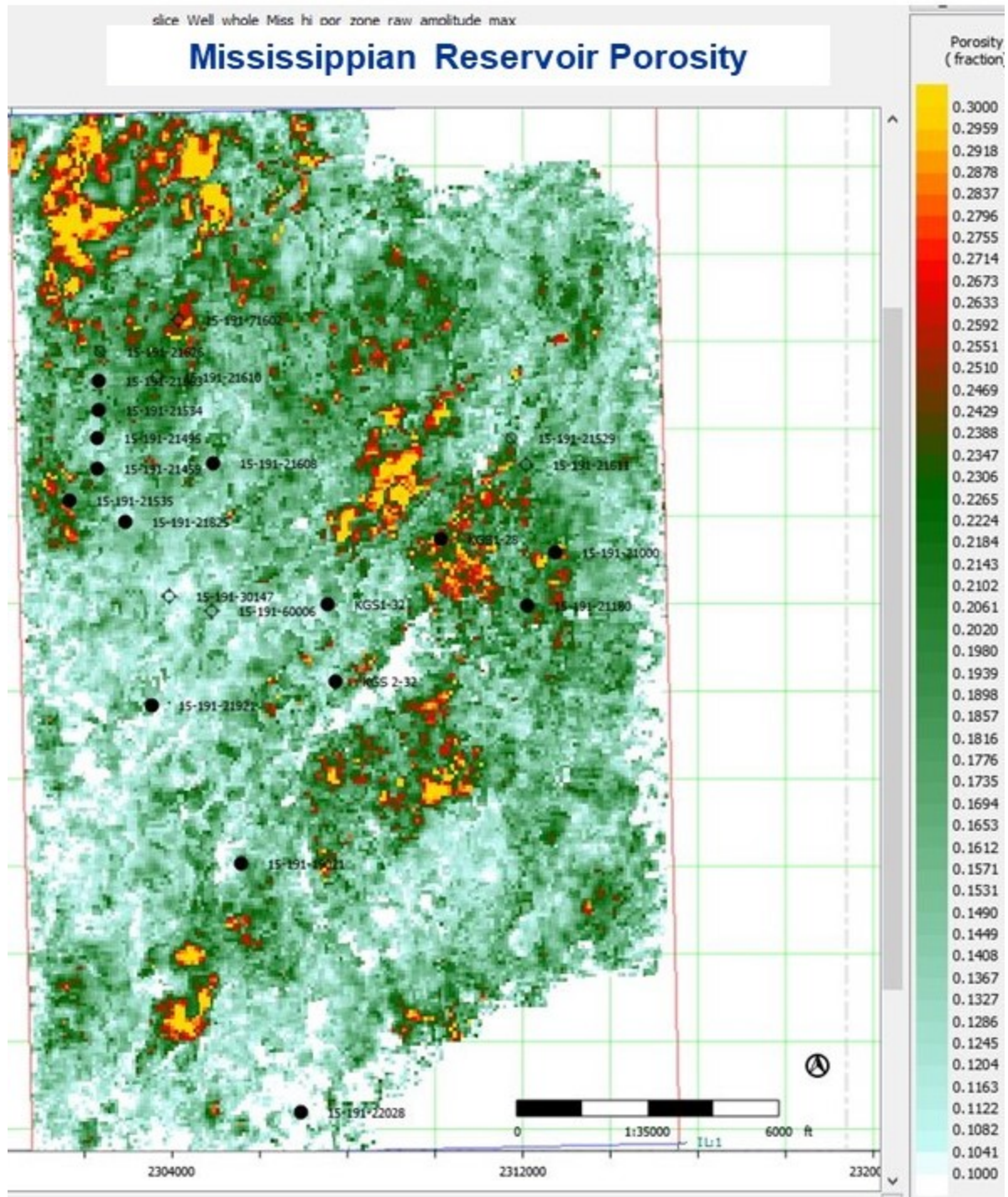


Figure S-12: Map of maximum Mississippian reservoir porosity predicted from the seismic data.

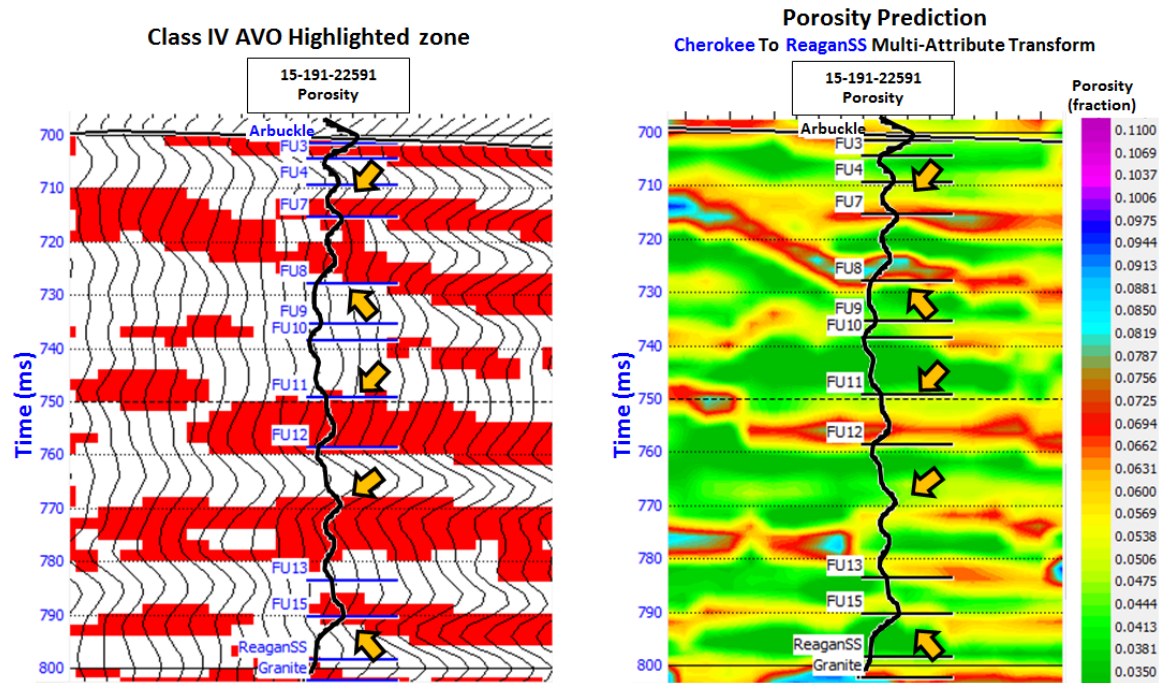


Figure S-13. (left) Cross section of Class IV AVO highlighted zone by the A-B cross plotting technique along inline #152. (right) Cross section of predicted porosity by the second multi-attribute transform along inline #152. The same Class IV AVO highlighted zones show high porosity values in the porosity prediction cross section. Black curves are formation porosity logs of well #15-121-22591. Horizontal lines identify mapped flow units in the Arbuckle. A good agreement is observed between flow units and predicted porosity.

III Pre-stack seismic AVAZ (amplitude variation with azimuth) analysis for determination of Mississippian and Arbuckle fracture density and orientation

Key findings

- Azimuthal anisotropy is detected in 3-D P-P pre-stack gathers.
- Seismic anisotropy analysis results support known large scale features (faults) in the field.
- Seismic anisotropy results are consistent with well log observations and geomechanical models at Wellington Field.
- Fracture patterns mapped in the Mississippian are in agreement with observed CO₂ migration paths.

Background

Previous investigations by Sirazhiev (2012) and Fadolkarem (2015) mapped reservoir thickness and porosity distribution at Wellington Field. This work examines whether the 3-D P-wave reflection seismic can quantify azimuthal anisotropy in the Mississippian cherty dolomite and Lower Ordovician Arbuckle Group dolomite. Carbonates exhibit anisotropy due to varied crystalline structure, porosity geometry, and fractures. The results obtained can provide insight into the in situ stress, relative fracture density, and orientation in the two reservoirs as well as preferential fluid migration paths.

Methods

Seismic anisotropy is observed as the variation in seismic velocity and amplitude with orientation of wave propagation. Accounting for seismic anisotropy can quickly become computationally complex and difficult to constrain. If a simplifying model can be applied to the geology, however, accounting for the anisotropy is facilitated. Defining a plane of isotropy can decrease the complexity. In horizontal planes of isotropy, observed in shales and thin bed sequences, the simplifying model is referred to as Vertically Transverse Isotropy (VTI) or Radial Anisotropy and is interpreted as AVO. Vertical planes of isotropy due to stress and vertical fractures is considered Horizontally Transverse Isotropy (HTI) or Azimuthal Anisotropy (Ruger, 1998; Thomsen, 2002; Lynn, 2016). This study focuses on azimuthal anisotropy to visualize the stress and fractures.

Accounting for anisotropy in data has several important implications for subsurface imaging. Anisotropy correction in a horizon can provide improved depth constraint. Not accounting for anisotropy can lead to over migration of dipping features as well as under estimation of depth in horizontal features in a Pre-Stack Depth Migrated (PSDM) survey that otherwise appears to be well focused (Hawkins et al., 2001). Anisotropy analysis can also provide understanding of reservoir characteristics and planning. With high quality wide azimuth-wide offset surveys, improved pre-stack coverage can improve on AVO, as well as allow for stress and reservoir mechanics calculations through Amplitude Variation with Azimuth (AVAZ) (Gray et al., 2012). The orientation of the plane of isotropy is analogous to the direction of maximum horizontal stress (σ_H) and fracture orientation.

Results

i) Fracture mapping

Azimuthal analysis of the 3-D P-P wave data collected in Wellington provides a sense of the anisotropy in the top of the Mississippian and Arbuckle. A defining feature observed in both is a fault (black line) that trends northeast through the three green wells in figures S-14 and S-15. The fault is associated with discrete facies changes across the field (Sirazhiev, 2012; Fadolkarem, 2015). The perceived fracture pattern surrounding the fault in the Arbuckle is also within the range of σ_H and fracture orientations determined from Schwab (2016).

Azimuthal anisotropy of the Mississippian and Arbuckle is shown in figures S-14 and S-15 respectively. Results are consistent with observed rock properties known to cause detectable variations in seismic data: fracture and maximum horizontal stress direction. Large-scale features such as faults are indirectly observed by its effect on the surrounding material. Fractures observed in FMI logs are consistent with patterns observed in the Wellington Field seismic azimuthal analysis (Figure S-15).

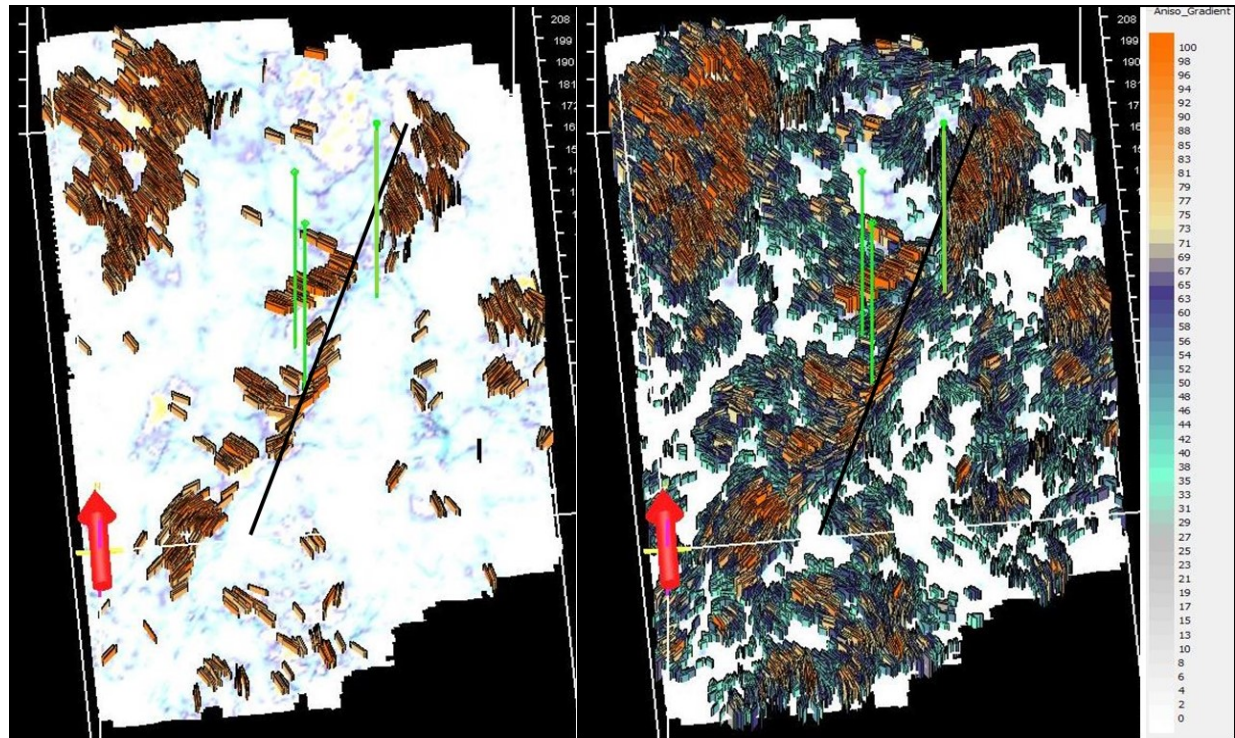


Figure S-14: Mississippian anisotropy. Tilted perspective of the azimuthal planes of isotropy at the high porosity top of the Mississippian chert. The left panel illustrates a higher degree of anisotropy (66%–100%) to the isotropic plane. The right panel illustrates smaller degrees of anisotropy (33%–100%). The orientation can be interpreted as fractures and stress direction, and the size and color is the degree of anisotropy. The black line is the fault as also mapped by Sirazhiev (2012) and Fadolkarem (2015). Green lines show wells KGS 1-32, KGS 1-28, and KGS 2-32.

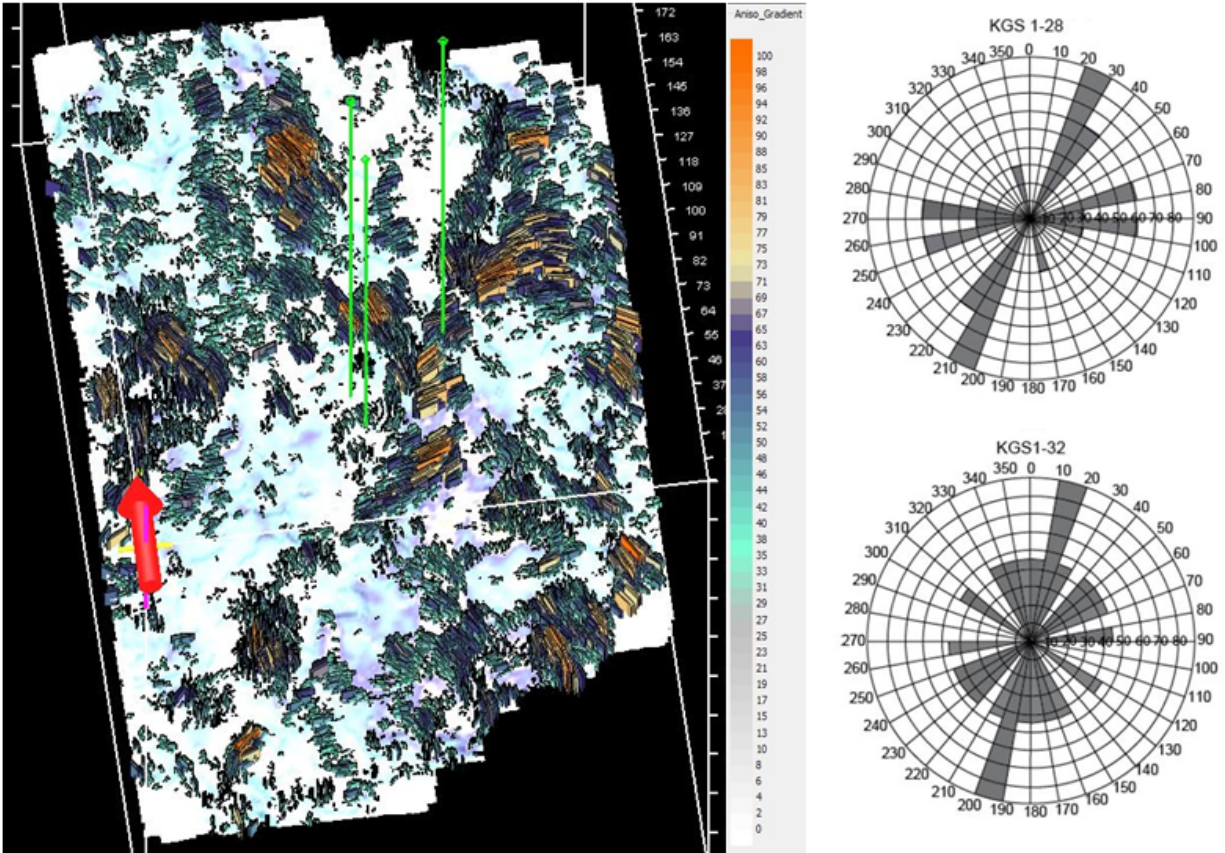


Figure S-15: Arbuckle anisotropy. (left) Tilted perspective of the azimuthal planes of isotropy average throughout the Arbuckle. The panel illustrates a higher degree of anisotropy (25%–100%) to the isotropic plane. The orientation can be interpreted as fractures and stress direction, and the size and color is the degree of anisotropy. The black line is the fault as also mapped by Sirazhiev (2012) and Fadolkarem (2015). Green lines show wells KGS 1-32, KGS 1-28, and KGS 2-32. (right) Natural open fractures observed in FMI logs in wells KGS 1-28 and 1-32 (from Schwab 2016).

ii) CO₂ monitoring

The Mississippian reservoir fracture and porosity predictions from 3-D seismic are compared to the monitored mobility of the CO₂ injected in well KGS 2-32 in spring 2016. Early time monitoring of the CO₂ injection is shown to follow preferential paths along fractures delineated by the seismic data (Figure S-16). CO₂ breakthrough is observed along boreholes aligned with the mapped dominant fractures. At the completion of the injection, CO₂ appears to be distributed more evenly in the Mississippian reservoir, although the influence of porosity and fracture distribution on CO₂ mobility is still evident in figure S-17.

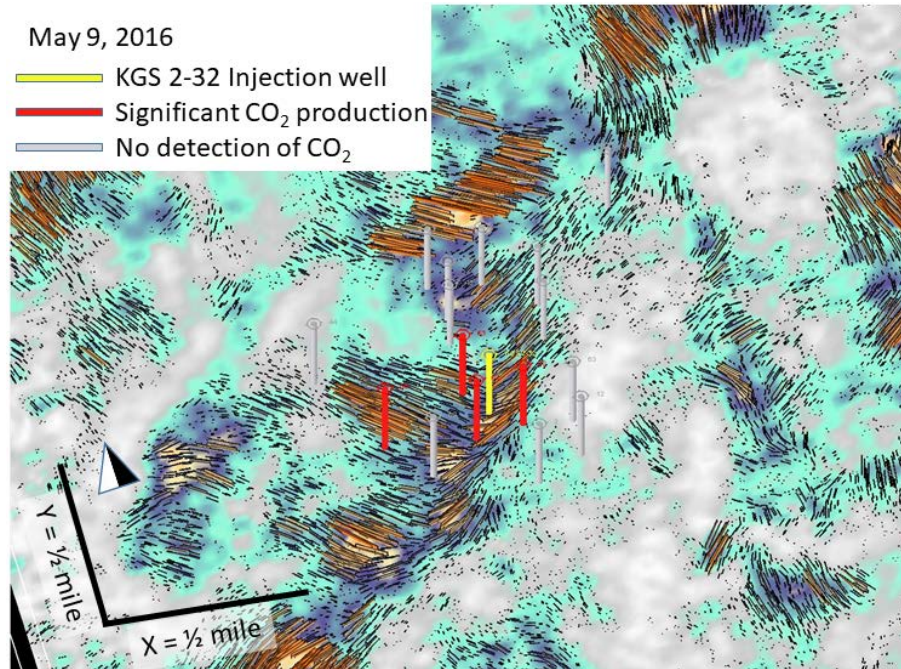


Figure S-16: Mississippian anisotropy map shown along with the injection well KGS 2-32 (yellow), wells with significant CO₂ production (red), and neighboring wells with no detection of CO₂ (gray).

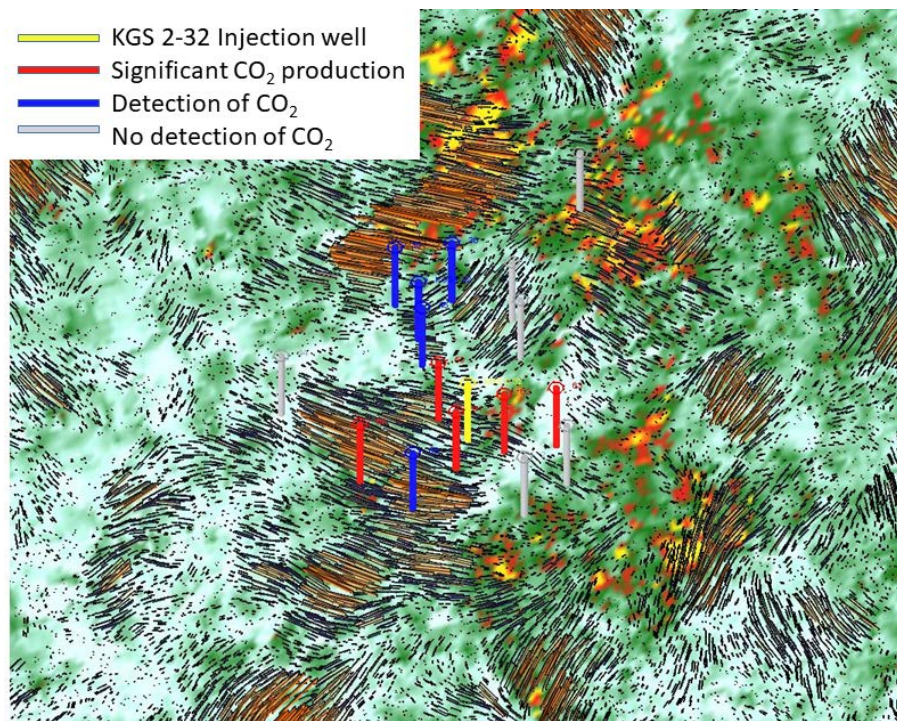


Figure S-17: Mississippian anisotropy map with porosity overlay in color (yellow/red = high porosity; white = low porosity), shown along with the injection well KGS 2-32 (yellow), wells with significant CO₂ production (red), wells with detection of CO₂ (blue), and wells with no detection of CO₂ (gray).

IV Time-lapse seismic assessment of CO₂ injection in the Mississippian reservoir

Key Findings

- Fluid substitution modeling evaluates the effect of CO₂ injection in the acoustic impedance of the Mississippian reservoir.
- Synthetic seismograms at three well locations are used to interpret pre- and post-CO₂ injection seismic response.
- Time-lapse 2-D post-stack seismic data analysis does not show evidence of the injected CO₂, likely due to low saturation.
- Ongoing analysis is examining the response of pre-stack seismic, AVO analysis and impedance inversion for CO₂ detection in the Mississippian reservoir

Background

The purpose of this study is to assess time-lapse seismic monitoring of CO₂ migration within the Mississippian reservoir and its effectiveness for enhanced oil recovery (EOR). In spring 2016, a CO₂ injection pilot study of the Mississippian cherty dolomite reservoir in Wellington Field was conducted to determine the feasibility of CO₂ for EOR in this area. A 3-D P-P seismic survey and two 2-D seismic lines (lines 01 and 02) were acquired in 2010, prior to the injection, and a final 2-D seismic line (line 03) was acquired post-injection (Figure S-1). Comparison of pre- and post-CO₂ injection seismic along with fluid substitution reservoir modeling and synthetic seismogram generation are used to evaluate seismic monitoring of CO₂ in the Mississippian.

Methods

A classical fluid substitution method for predicting seismic response is the Biot-Gassmann, commonly known as Gassman model. However, heterogeneous pore properties of carbonates can prevent accurate estimation of pore fluid effects (Adam et al., 2006; Misaghi et al., 2010). Another method for estimating the effect of fluid substitution in carbonates is the patchy saturation model, which assumes a homogeneous medium with patchy fluid saturation (Vega et al., 2007). The Gassmann and Patchy models were tested with Hampson Russell Suite (HRS) to evaluate amplitude effects of CO₂ substitution in the Mississippian reservoir. Estimated CO₂ parameters at the reservoir conditions were used to calculate the seismic effects. Well log data for density, porosity, lithologic constituents, V_p , and V_s were included in the model. Initial conditions were set to 100% water with a systematic 2% increase in CO₂ up to 100% CO₂ saturation. CO₂ saturation at the injection well can be as high as 80%–90%. Diffusion away from the well and compressibility effects of CO₂ mixed in water exhibit different elastic effects depending on the substitution model used. Synthetic seismic traces at the injection wells were computed for each scenario.

A 2-D seismic line (03) acquired immediately after completion of the CO₂ injection in June 2016 is compared with pre-injection data. The initial comparison evaluates post-stack data. Pre-stack seismic analyses are continuing.

Results

Comparison of the post-stack, post-injection 2-D seismic line and an arbitrary seismic line extracted from the 3-D P-P seismic survey do not reveal any significant amplitude changes in the post-stack seismic data (Figures S-18 and S-19). This can be the result of the high matrix incompressibility of carbonate rocks and the relatively small amount of CO₂ injected in this experiment. Further analysis will include AVO and pre-stack analysis of the seismic data, which is expected to exhibit greater sensitivity to changes in reservoir fluid content with reflectivity changes up to 10% (Figure S-20).

Synthetic seismograms were created for each 2-D seismic line and their respective wells. Pre-injection seismic lines 01 and 02 were tied with wells KGS 1-32 and KGS 1-28, respectively, while the post-injection 2-D seismic line was tied with the original KGS 2-32, the injection well (Figures S-21, S-22, and S-23). The synthetic traces show good agreement with the observed field seismic data.

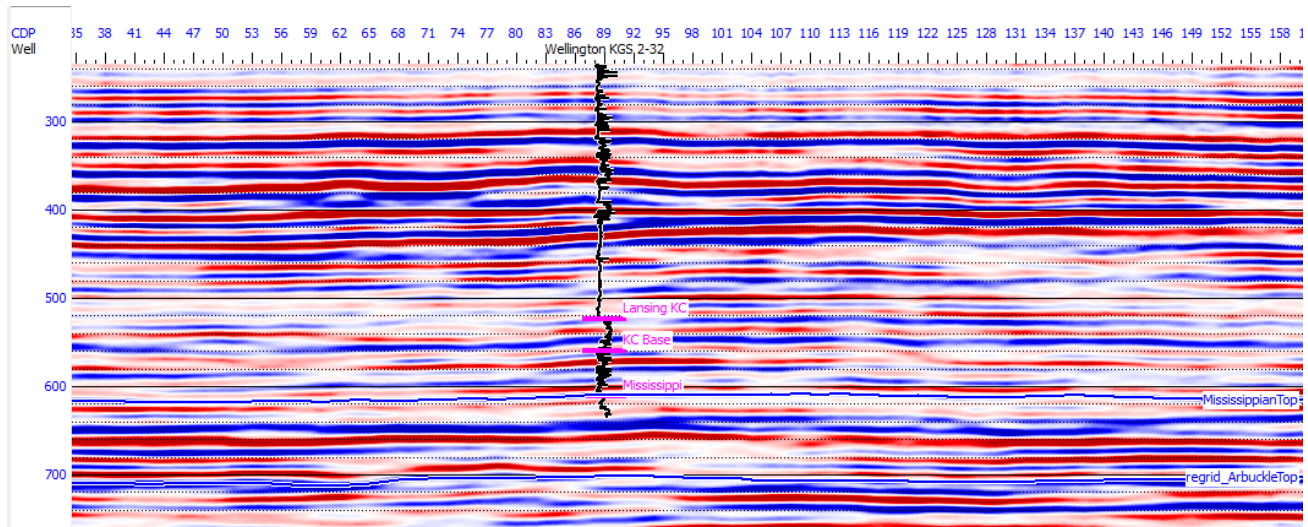


Figure S-18. Arbitrary line extracted from the 3-D P-P seismic survey, displaying the location of the CO₂ injection well KGS 2-32.

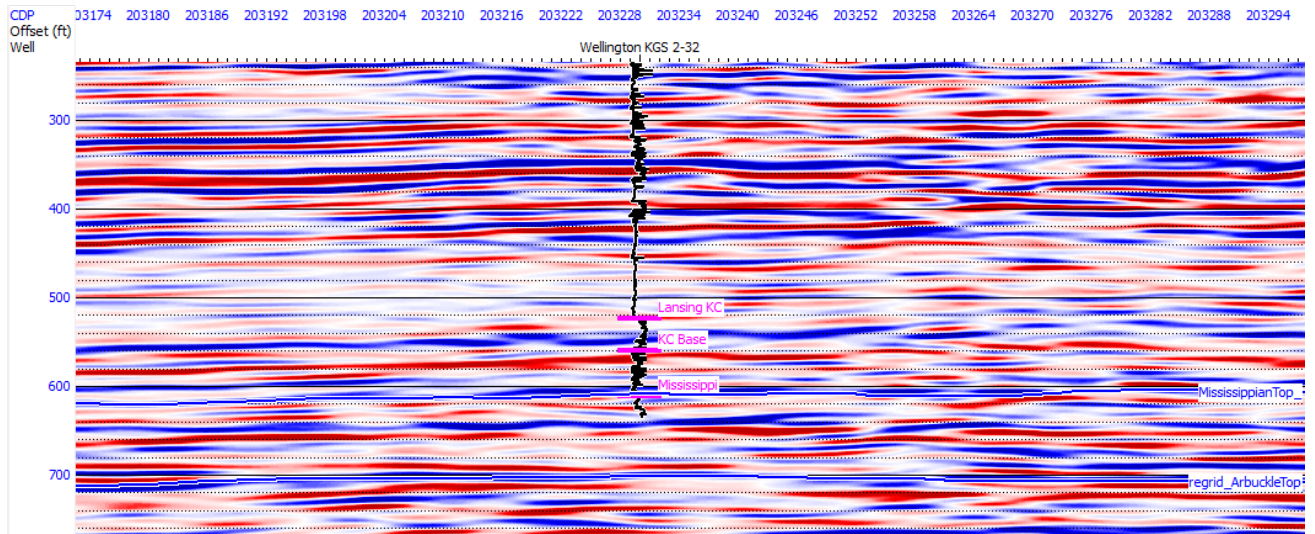


Figure S-19. 2-D seismic line 03 acquired post-injection, displaying the location of well KGS 2-32.

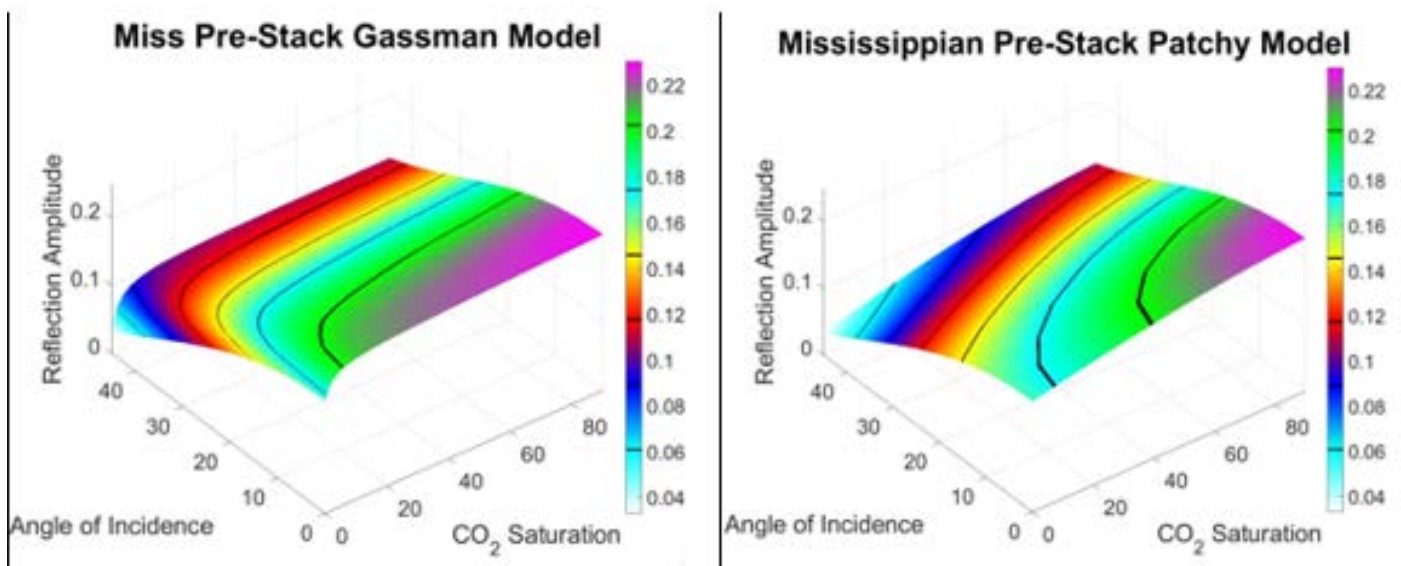


Figure S-20. Gassmann (left) and Patchy (right) models for the Mississippian reservoir exhibit reflectivity changes up to 10% suggesting the potential for measurable amplitude changes in pre-stack seismic data analysis.

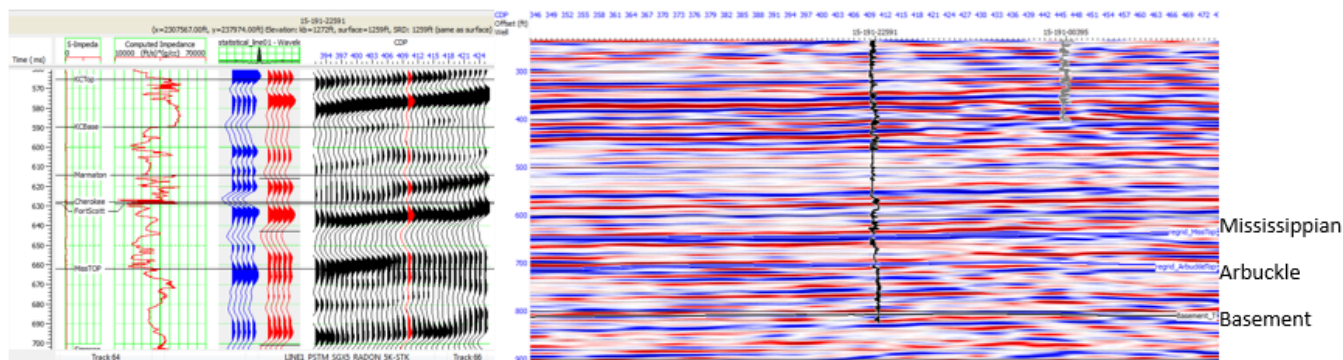


Figure S-21. Synthetic seismogram "tying" well KGS 1-32 and 2-D seismic line 01.

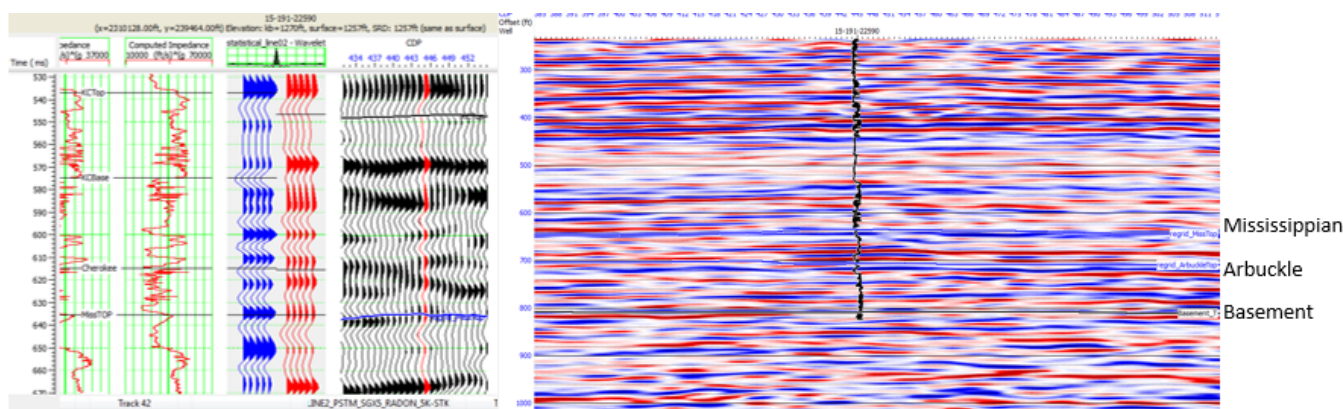


Figure S-22. Synthetic seismogram "tying" well KGS 1-28 to 2-D seismic line 02.

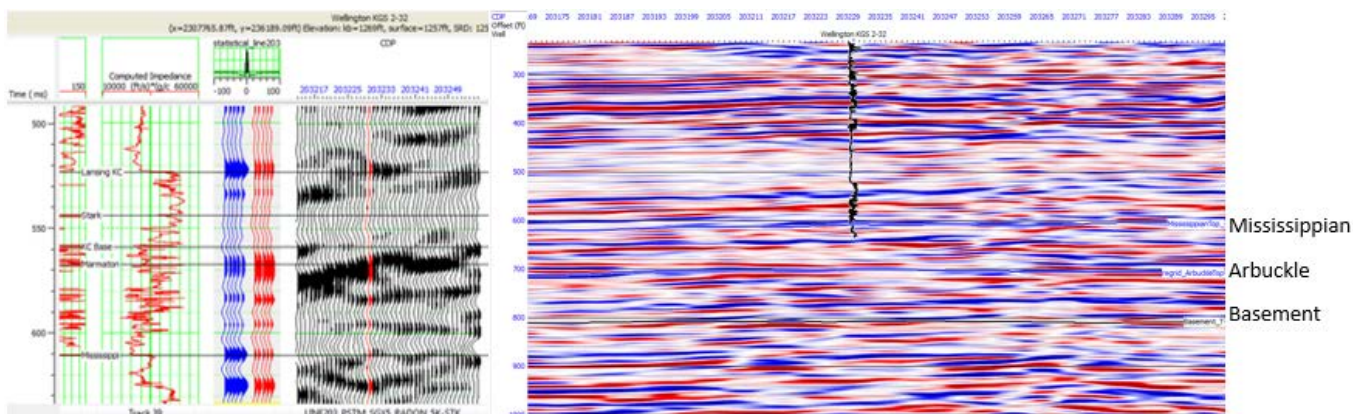


Figure S-23. Synthetic seismogram "tying" well KGS 2-32 and 2-D seismic line 03 (post-injection).

Passive seismic monitoring of earthquake activity near the CO₂ injection site at Wellington Field, south-central, Kansas

Seismicity in the United States midcontinent has increased by orders of magnitude over the past decade. Spatiotemporal correlations of seismicity to wastewater injection operations have suggested that injection-related pore fluid pressure increases are inducing the earthquakes. In this investigation, we examine earthquake occurrence in southern Kansas and northern Oklahoma and its relation to the change in pore pressure. The main source of data comes from the Wellington Array in the Wellington oil field, in Sumner County, Kansas, which has monitored for earthquakes in central Sumner County, Kansas, since early 2015. The seismometer array was established to monitor CO₂ injection operations at Wellington Field. Although no seismicity was detected in association with the spring 2016 Mississippian CO₂ injection, the array has recorded more than 2,500 earthquakes in the region and is providing valuable understanding of induced seismicity. A catalog of earthquakes was built from this data and was analyzed for spatial and temporal changes, stress information, and anisotropy information. The region of seismic concern has been shown to be expanding through use of the Wellington earthquake catalog, which has revealed a northward progression of earthquake activity reaching the metropolitan area of Wichita. The stress orientation was also calculated from this earthquake catalog through focal mechanism inversion. The calculated stress orientation was confirmed through comparison to other stress measurements from well data and previous earthquake studies in the region. With this knowledge of the stress orientation, the anisotropy in the basement could be understood. This allowed for the anisotropy measurements to be correlated to pore pressure increases. The increase in pore pressure was monitored through time-lapse shear-wave anisotropy analysis. Since the onset of the observation period in 2010, the orientation of the fast shear-wave has rotated 90°, indicating a change associated with critical pore pressure build up. The time delay between fast and slow shear wave arrivals has increased, indicating a corresponding increase in anisotropy induced by pore pressure rise. In-situ near-basement fluid pressure measurements corroborate the continuous pore pressure increase revealed by the shear-wave anisotropy analysis over the earthquake monitoring period.

This research is the first to identify a change in pore fluid pressure in the basement using seismological data and it was recently published in the AAAS journal *Science Advances* (Nolte et al., 2017). The shear-wave splitting analysis is a novel application of the technique, which can be used in other regions to identify an increase in pore pressure. This increasing pore fluid pressure has become more regionally extensive as earthquakes are occurring in southern Kansas, where they previously were absent. These monitoring techniques and analyses provide new insight into mitigating induced seismicity's impact to society.

INTRODUCTION

Passive seismic monitoring was established in 2015 at Wellington oil field in order to monitor planned CO₂ injections for EOR in the Mississippian reservoir and sequestration in the Arbuckle saline aquifer. Local seismicity is recorded by an array of 18 seismometers at and near Wellington Field. Although no earthquakes were recorded in association with the spring 2016 CO₂ injection in the Mississippian reservoir, data from more than 2,500 local induced seismicity events have been recorded (Figure S-24). The seismic network, earthquake catalog, and data analyses are described in the MS thesis by Nolte (2017) (Appendix S-D).

Passive seismic data investigations at Wellington Field are summarized as follows:

- I. Monitoring the northward advance on injection-induced seismicity in southern Kansas.
- II. Understanding injection induced seismicity in the midcontinent through shear-wave anisotropy ananalysis.

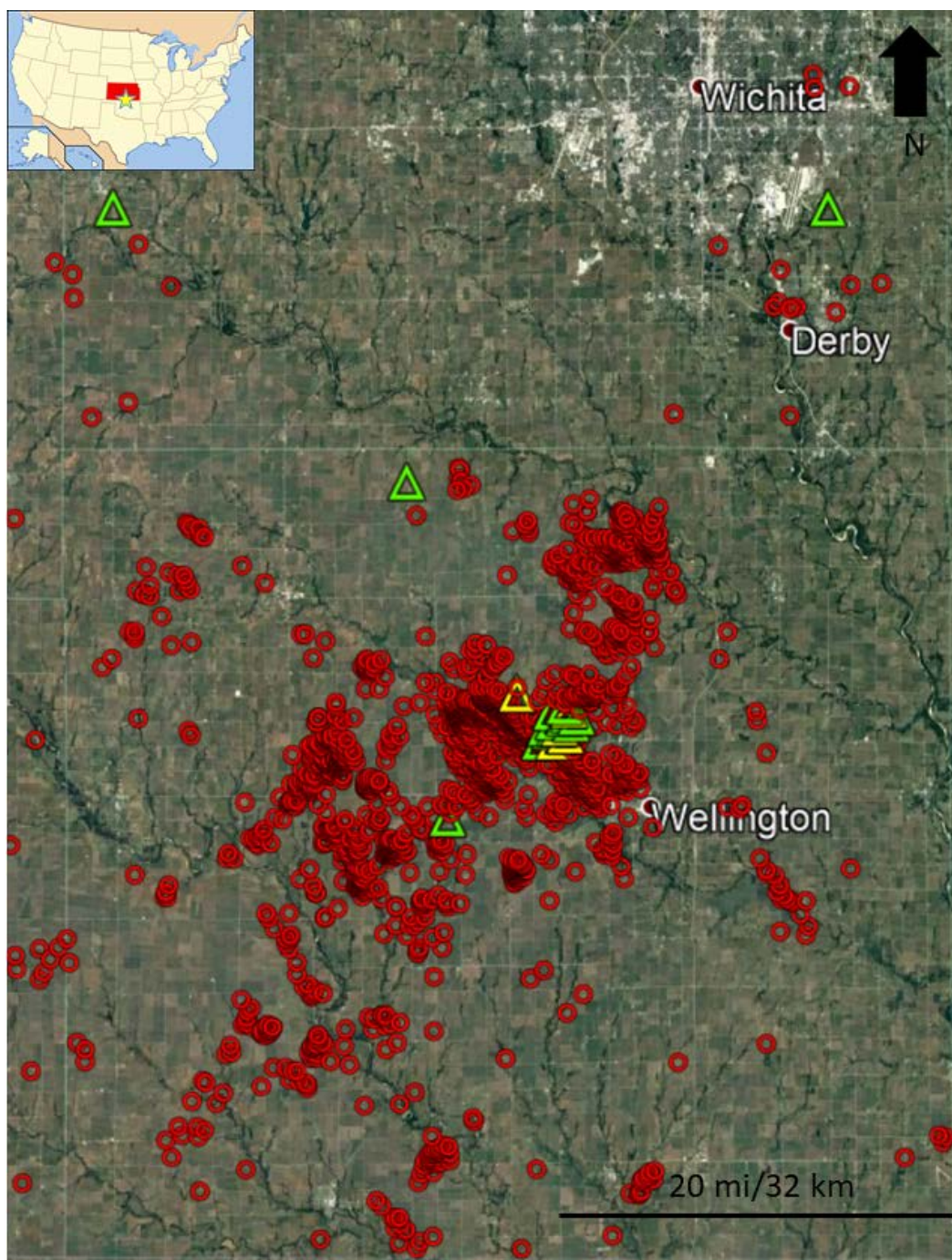


Figure S-24: This map shows 2,522 southern Kansas earthquakes that occurred from May 2015 to July 2017. Earthquake magnitudes range from 0.4 to 3.6 magnitude. A 3.0 magnitude earthquake is usually felt by humans. Red circles indicate earthquakes. Triangles indicate seismometers of the Wellington array.

I Monitoring the northward advance on injection-induced seismicity in southern Kansas

For detailed description refer to the MS thesis by Nolte (2017) (Appendix S-D)

Key Findings

- The number of earthquakes in southern Kansas continues to increase.
- Over the last two years earthquakes have been advancing northward, from northern Oklahoma to southern Kansas.
- The regions affected by induced seismicity are growing.

Background

Kansas and Oklahoma have seen a drastic increase in seismicity in recent years with magnitude 3 and larger events increasing ~30 fold in 2014 compared to the historical average. Seismicity in the region seems to have peaked in 2016. Reduction of injection rates imposed by the states of Kansas and Oklahoma have been followed by a reduction in seismicity, although earthquakes continue to occur at greater frequency and magnitudes than historical averages. Recent evidence has indicated an increase in basement pore pressure as the cause of the increased seismic activity. This increased pore pressure has been predicted through modeling to be caused by high volume injection wells disposing of brine water in the Arbuckle Formation (Ellsworth, 2013). The high pore fluid pressures are causing ancient fault systems to reactivate and slip. The region of seismic concern has grown over the past seven years and the growth in the affected area is believed to be associated with the movement of a higher pore fluid pressure zone in the basement, which is expanding outwards from high-rate injection wells.

Methods

The KGS has installed a seismometer array in the Wellington oil field with the objective of monitoring for potentially induced seismicity from CO₂ injections in the Arbuckle and Mississippian carbonate reservoirs. However, during this period of monitoring, the issue of induced seismicity from fluid injection in the Arbuckle has grown, and data from the array have been used to monitor for regional earthquakes. Data from the Wellington array have been used to clearly demonstrate a northward trend of earthquakes in Kansas

Results

Earthquakes near the Wellington oil field have been recorded and cataloged since April of 2015. A total of nearly 2,400 earthquakes occurred in the study area over this time period. The moment magnitude (M_w) scale has been used because it is the standard for very local/induced seismicity (Stork, 2014). The magnitudes have ranged from M_w 0.4 to 3.8 in Kansas. Magnitudes are calculated from the spectral energy of the earthquake (Stork, 2014) in the open-source software

SeisAn (Havskov and Ottemoller, 1999). All earthquake locations from the Wellington array can be seen in figure S-25.

The first earthquakes in Kansas occurred very near the Oklahoma border, in Sumner and Harper counties. Earthquakes are now occurring in many more counties in southern Kansas, including Sedgwick County, home to the largest city in Kansas, Wichita. Earthquakes have occurred within the Wichita metro but have been relatively small and unfelt ($M_w < 2.5$). The Wellington array is in an optimal location to continue to monitor the movement and potential risk of induced seismicity in Kansas. As larger, felt earthquakes are occurring along the Kansas-Oklahoma border, the array will be able to assess areas of potentially higher seismic concern, in an effort to help mitigate risk.

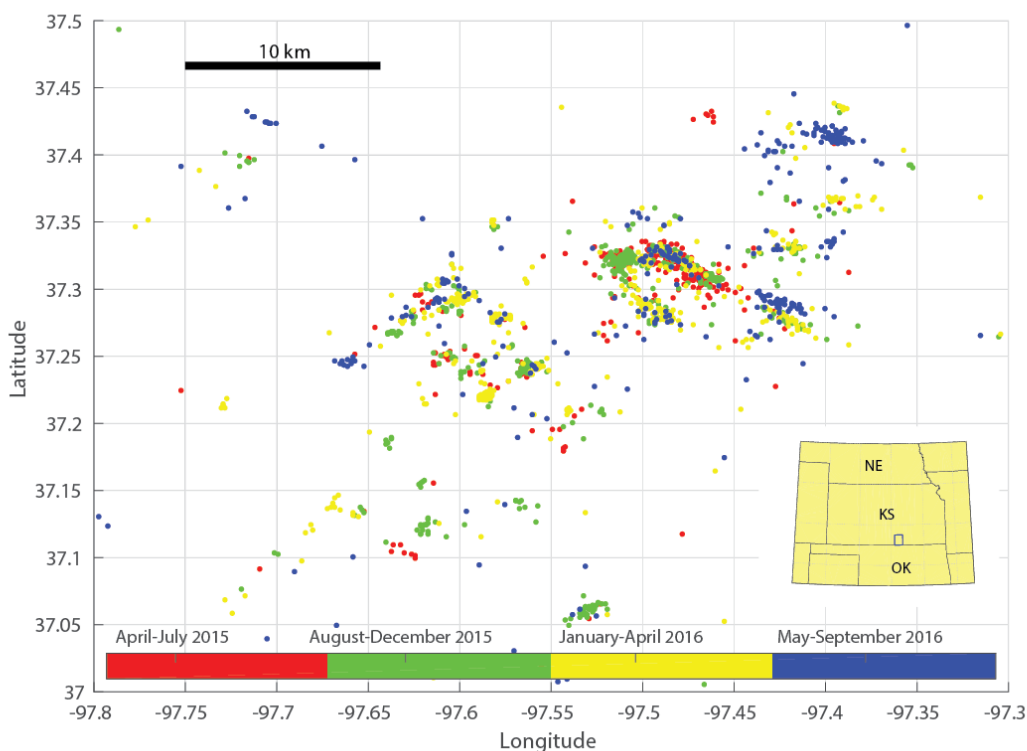


Figure S-25: Map of 1,898 events observed between April 2015 and December 2016 in western Sumner County. Earthquakes are colored by time of occurrence. Red corresponds to oldest earthquakes, and blue indicates the most recent earthquakes. Blue is more common to the northeast of the map, indicating northward progression.

The advancement of induced seismicity in Kansas demonstrates that large-volume injection-induced pore-pressure increases can have effects on regional seismicity. Shallow basement pore pressure increase appears to affect seismicity several tens of miles away from individual injection wells. Far reaching pore pressure changes can be of concern to populated

regions from Texas to Ohio that are currently facing injection-induced seismicity. Additional monitoring of induced seismicity is needed to understand the underlying processes and effectively mitigate the risk associated with induced earthquakes

II Understanding injection induced seismicity in the midcontinent through shear-wave anisotropy analysis

For a detailed description, refer to the MS thesis by Nolte (2017) (Appendix S-D)

Journal publication: “Shear-Wave Anisotropy Reveals Pore Fluid Pressure-Induced Seismicity in the US Midcontinent” by Nolte et al. (2017), Science Advances (Appendix S-E)

Key Findings

- Previous models suggest increasing pore pressure from high-volume wastewater injection is inducing seismicity in Oklahoma and Kansas.
- Shear-wave anisotropy analysis presented in this investigation is the first direct evidence provided by seismological observations to detect the increase in pore fluid pressure.
- Pressure monitoring in well KGS 1-28 confirms the pressure increase in the study area.

Background

Seismicity in the midcontinent of the United States has seen a dramatic increase from the historical average of 21 magnitude (M) ≥ 3 earthquakes per year to 188 $M > 3$ earthquakes in 2011 (Ellsworth, 2013). High levels of seismicity persist to date, with 688 $M > 3$ earthquakes in 2014 (Rubinstein and Mahani, 2015). Spatiotemporal analysis of earthquakes and wastewater injection in the Arbuckle point to pore fluid pressure increases as the cause of increased seismicity across the central U.S. (Ellsworth, 2013; Keranen et al., 2014), but direct evidence from seismological data has not been documented (Keranen et al., 2014). Time-lapse earthquake shear-wave (S-wave) split analysis, presented in this investigation, demonstrates that pore fluid pressure in the shallow basement has increased over time to a critical pressure and is the cause of the increased seismicity.

Methods

This study examines whether the recent seismicity in northern Oklahoma and southern Kansas exhibits changes in shear wave anisotropy (i.e., fast S-wave Φ flips and increased dt scatter), which would constitute direct evidence of critical pore pressure build-up along the ray paths traveled. The time-lapse earthquake data analyzed spans the period from 2010 to 2016. A total of 120 earthquakes of magnitude (M_w) 2 or greater were used for this study. Most events were

in the range of M_w 2 – M_w 3, the largest event was a M_w 4.3, and all earthquakes occurred in the shallow basement (1–11 km depth). Earlier events in 2010–2012 came from northern Oklahoma, given the scarcity of earthquakes in southern Kansas at that time. Since 2013, there has been increased seismicity in south-central Kansas. In-situ downhole pressure measurements in the Arbuckle Group saline aquifer, approximately 30 m above basement, were obtained from the KGS 1-28 well in the Wellington oil field.

Results

There is a 90° flip in the Φ of events that occurred in 2015–2016 (Figure S-26, A3) compared to events from an earlier time window (2010–2015) (Figure S-26, A1, A2). The early solution of Φ is in the direction of the maximum horizontal stress in the region ($\sim 75^\circ$) as calculated from earthquake focal mechanisms and from well-bore sonic log data analysis (Alt, 2016). In the histogram corresponding to the 2015–2016 earthquakes (Figure S-26, A3), the fast shear wave orientation Φ is offset by approximately 90° from the maximum horizontal stress, causing it to align with the minimum horizontal stress. This rotation in Φ and the narrow timeframe of its occurrence provide evidence of a change that may be anthropogenic. Such changes in Φ have previously been identified as an effect of pore fluid pressure increases, where the ray path travels through rock that is critically stressed by pore fluid for a longer distance than rock that is not critically stressed by pore fluid (Zinke and Zoback, 2000; Crampin et al., 2004). These studies have also identified large deviation in dt shown to be associated with pore fluid pressure changes.

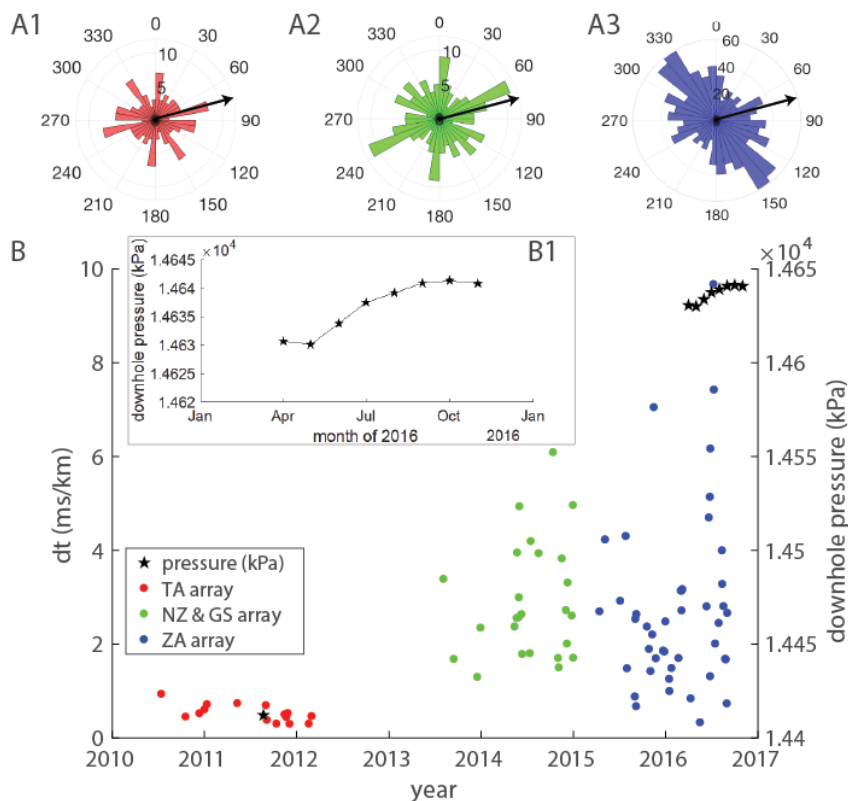


Figure S-26: (A1) Polar histogram of Φ from TA events 2010–2012 (red). The most common Φ value is near the maximum horizontal stress of $\sim 75^\circ$ along with flipped values at $\sim 330^\circ$. Zero degree values are most often null solutions. (A2) Polar histogram of Φ from NZ & GS events 2013–2015 (green) showing common solutions in line with maximum horizontal stress as well as solutions 90° off of maximum horizontal stress. (A3) Polar histogram of Φ from ZA events 2015–2016 (blue) showing the most common solution to be 90° off of the maximum horizontal stress, a direct indicator of critical pore fluid pressure. Arrows indicate the orientation of maximum horizontal stress at 75° . (B) Average dt/km of earthquakes from 2011 through 2016, showing a steady increase over time, as well as an increase in variance of data. Black stars showing average pressure per month from downhole pressure monitoring in KGS 1-28, in Wellington oil field. The initial pressure measurement was obtained when the well was drilled in August 2011. Inset B1 is an expanded view of monthly pressure observations from April to November 2016.

The analysis shows increasing values, range, and scatter in dt estimates (Figure S-26B). The increase in dt suggests increasing anisotropy of the rock, often associated with the fracture density and aperture width (Crampin, 1999). It is likely that the basement has become critically stressed by increasing pore fluid pressure. The pore fluid pressure increase reduces the effective stress on the rock, which previously kept fractures that were not parallel to the maximum horizontal stress closed (Crampin et al., 2004). Increasing pore fluid pressure can cause fractures to shear or dilate, increasing the anisotropy and the magnitude of dt.

The observed flip in Φ as well as the increase in average dt and the increase in dt scatter are interpreted as direct evidence of an increase in pore fluid pressure over time. These changes correlate with downhole pressure data acquired at the KGS 1-28 well in the lower Arbuckle saline aquifer, near the basement. Bottomhole pressure has increased more than 200 kPa since 2011, when the well was drilled (Figure S-26B). The borehole remained idle until April of 2016, when a pressure sensor was installed for continuous monitoring of the lower Arbuckle. The high resolution pressure measurements since April show that downhole pressures are increasing at a rate of 3–4 kPa per month (Figure S-26B1).

The shear-wave splitting analysis presented here, correlated with downhole pressure monitoring data, is the first direct evidence of increasing pore pressure in the region detected by seismic observations. These results show that analyzing the change in anisotropy of the basement is an effective means of identifying critical changes in pore fluid pressure that are the likely cause of fault reactivation and earthquakes in the region (Ellsworth, 2013; Walsh and Zoback, 2015). This methodology could be applied to other regions of potentially induced seismicity to verify that increasing pore fluid pressure related to deep well injection is the underlying cause of seismicity increases.

Pressure Monitoring in the Arbuckle Formation in the Wellington KGS 1-28

The continuous pressure monitoring in the lower Arbuckle was set up because a large rate and high volume brine disposal in the area is believed to be responsible for induced seismicity. The

assumption in the case of the testing in the Arbuckle is that the observed pressure is being transmitted at depth in the basement where faults are critically stressed, requiring a small force to move. To date the vast majority of earthquakes have occurred in the shallow basement. Trilobite Testing of Hays Kansas installed the pressure gauge in Wellington KGS 1-28 at about 5,020 ft depth from surface. The instrument is programmed to sample every second with an accuracy of 0.1 psi. About a week of pressure data is sent to the KGS as a comma separated values (CSV) file. A Java computer program was developed to analyze the pressure data from KGS 1-28 to understand the pressure changes and to remove solar and lunar tidal pressures along with barometric pressure changes. The idea is that it is possible remove, account for, or explain natural every day influences and investigate only the geological influences and identify fluid movement due to brine injection, micro quake swarms, etc. Figure 52 is an illustration of the raw pressure measurement in psig units over a four-day period, 30 July to 2 August 2016.

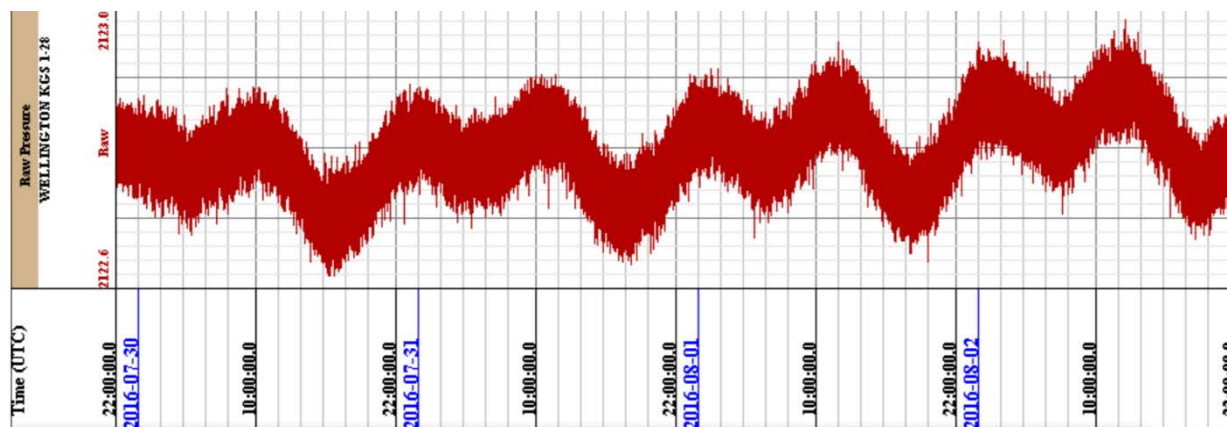


Figure 52. Raw pressure data measurements in Wellington KGS 1-28 from 30 July to 2 August 2016.

The computer program filtered the noise from the raw pressure data, computed the lunar and solar tidal pressures along with the barometric pressures influence, and then subtracted that from the raw pressure data. In an ideal situation, if these are the only pressures influencing the pressure measurements then the pressure data should result in a straight line (Fig. 53).

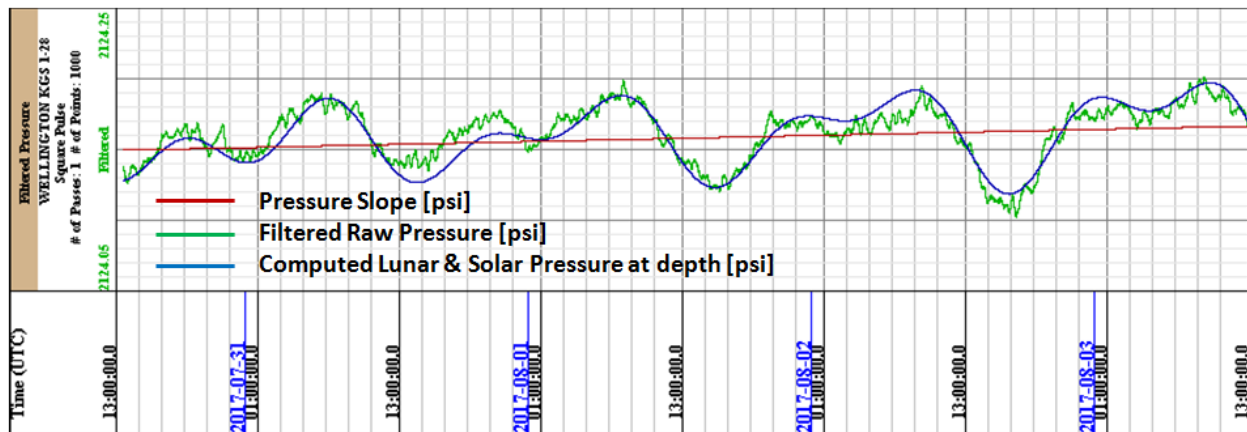


Figure 53. Filtered raw pressure vs. computed lunar and solar pressure at depth.

The computed lunar and solar pressure at depth (blue curve) coincides well with the measured filtered raw pressure (green curve). The deviations are attributed to the barometric pressure influence, which will be explained next. If both the lunar and solar pressure and the barometric pressure were removed from the filtered raw pressure data, the resultant pressure curve would line up on the pressure slope (red curve), accounting for all the known outside influences.

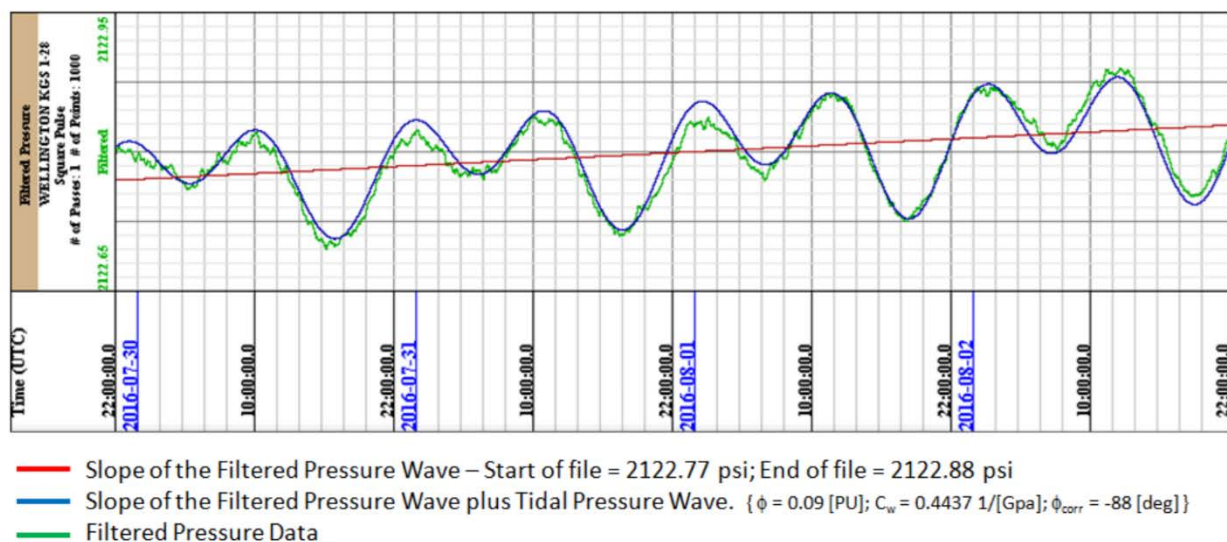


Figure 54. Filtered pressure data with the computed lunar and solar pressure wave.

We do not have the exact height of the water column above the pressure sensor, so the only way to incorporate the barometric pressure influence at the pressure sensor is to estimate what the measured pressure data should be at the sensor. The atmospheric pressure at KGS 1-28 is about 14.11 psi from the calculation of ideal altitude versus pressure curve. Ideally, if the lunar and solar pressure curve is subtracted from the measured data then the measured data should be a straight line. It is basically a straight line in Fig. 55, but there are deviations.

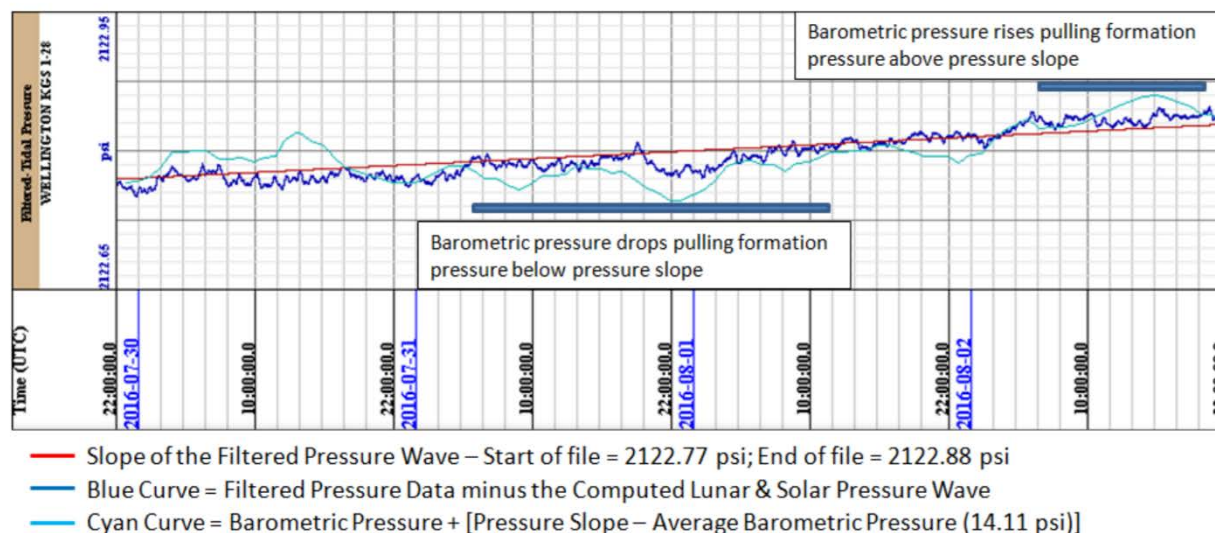


Figure 55. Lunar and solar pressure wave removed from measured pressure data.

A pressure curve is constructed by adding the barometric pressure measured at nearby Strother Field Airport with the difference of the pressure slope and 14.11 psi the average ideal barometric pressure at this elevation and overlaying that on the measured data. It can be seen that there is some comparison with the measured data. Ideally, if the barometric pressure is measured at KGS 1-28 then the computed barometric pressure should line up exactly with the linear pressure curve and any deviations from that would be other geological effects, i.e. fluid movement, etc.

Conclusions

As a result of CO₂ injection, observed incremental average oil production increase is ~68% with only ~18% of injected CO₂ produced back. Decline curve analysis forecast of additional cumulative oil production by only CO₂ flood was 32.44M STB for the end of 2027. Using 32M STB oil production and \$1,964,063 cost of CO₂, CO₂ EOR cost per barrel of oil production is ~\$60. Wellington Mississippian pilot efficiency by the end of forecast calculations is 11 MCF per barrel of produced oil. Calculated efficiencies are understandably low with the project operating under pilot conditions. Efficiencies similar to the Permian basin and other commercial operations are achievable if provided with the appropriate infrastructure in Kansas.

Simple but robust monitoring technologies along with sophisticated active and passive seismic monitoring methods proved to be very efficient in detection and locating of CO₂. High CO₂ reservoir retentions with low yields within actively producing field could help to estimate real-world risks of CO₂ geological storage. Wellington Field CO₂ EOR was executed in a controlled environment with high efficiency.

The KGS collected, compiled, and analyzed available data, including well logs, core data, SRTs, DSTs, 2-D and 3-D seismic data, water-level measurements, and other types of data. Several

exploratory wells were drilled and core was collected and modern suites of logs were analyzed. Reservoir properties were populated into several site-specific geological models. The geological models illustrate the highly heterogeneous nature of the Arbuckle Group.

The Arbuckle Group carbonate saline aquifer in Oklahoma and Kansas has been used extensively for waste disposal purposes since 1935. UIC Class I and Class II wells target the Arbuckle Group as the primary disposal zone in the region. However, recent developments of Mississippian Lime Play and other industrial activities are exerting unprecedented pressure on the Arbuckle saline aquifer use as an industrial waste disposal reservoir. There is an evidence gathered during the course of this project, independent pressure monitoring gages, UIC Class I well monitoring records, and other sources of regional fluid level and pore pressure increases in Arbuckle reservoir in Kansas and Oklahoma. Competing interests of various industrial groups that include oil and gas, chemical complex, and potentially CO₂ geological storage could collide in the future if a regulatory framework is not outlined and expanded.

Key accomplishments for this project include:

- Approximately 20,000 metric tons of CO₂ were injected in the upper part of the Mississippian reservoir. A total of 1,101 truckloads delivered 19,803 metric tons—an average of 120 tonnes per day—over the course of injection from January 9 to June 21, 2016.
- Well logs, core data, SRTs, DSTs, 2-D and 3-D seismic data, water-level measurements, and others types of data were collected, compiled, and analyzed. Several exploratory wells were also drilled and core was collected and modern suites of logs were analyzed. Reservoir properties were populated into several site-specific geological models.
- Earthquakes near the Wellington oil field have been recorded and cataloged since April 2015. A total of nearly 2,400 earthquakes occurred in the study area during this period.
- The shear-wave splitting analysis presented here, correlated with downhole pressure monitoring data, is the first direct evidence of increasing pore pressure in the region detected by seismic observations.
- Azimuthal analysis of the 3-D P-P wave data collected in Wellington provides a sense of the anisotropy in the top of the Mississippian and Arbuckle and reveals a fracture map for the field. Results are consistent with observed rock properties known to cause detectable variations in seismic data: fracture and maximum horizontal stress direction. Large-scale features such as faults are indirectly observed by their effect on the surrounding material. Fractures observed in FMI logs are consistent with patterns observed in the Wellington Field seismic azimuthal

analysis. The Mississippian reservoir fracture and porosity predictions from 3-D seismic are compared to the monitored mobility of the CO₂ injected in well KGS 2-32 in spring 2016.

- The analysis of well log and seismic data revealed that the reservoir exhibits different characteristics across a fault that divides the Wellington Field diagonally from the southwestern corner to the northeastern corner.
- Mississippian and Arbuckle reservoir AVO classification and pre-stack Seismic Inversion (Simultaneous AVO Inversion) were completed.

Lesson learned during this project include:

- This case study provides an insight that CO₂ EOR and geological storage could be successfully applied for Kansas carbonate reservoirs if CO₂ sources and associated infrastructure are ready and available.
- The geological models illustrate the highly heterogeneous nature of the Arbuckle and Mississippian Groups. Vertical and horizontal variability results in several distinct hydro-stratigraphic units. It is essential to account for this heterogeneity when constructing models, forecasting outcomes of operations, and estimating risks.
- Permitting pilot scale non-commercial project for geological storage is a major challenge. The detailed outline of lessons learned during the permit application process is outlined in a separate attached document.
- More detailed resource capacity studies are essential for shared use of a pore space for both CO₂ geological storage and other waste management.

Data gaps identified during this project include:

- Information about the interface between sedimentary formations (Arbuckle Group, Reagan, etc.) and the granite basement is virtually nonexistent. It is essential to conduct more drilling, coring, and hydrological testing in the Mid-Continent region.
- A far-field/regional injection test in Arbuckle Group would permit determination of hydrogeologic properties of faults and other heterogeneities to better address pressure propagation and its role in induced seismicity.

- Continued pore pressure and seismic monitoring in near granite basement intervals is also essential for understanding induced seismicity and other problems associated with shared use of pore space in the Mid-Continent.

References

- Adam, L., Batzle, M., and Brevik, I., 2006, Gassmann's fluid substitution and shear modulus variability in carbonates at laboratory seismic and ultrasonic frequencies: *Geophysics*, v. 71, no. 6, F173-F183.
- Bennion, B., and Bachu, S., 2007, Relative permeability characteristics for supercritical CO₂ displacing water in a variety of potential sequestration zones: Society of Petroleum Engineers, SPE-95547-MS.
- Bennion, B., and Bachu, S., 2010, Drainage and imbibition CO₂/brine relative permeability curves at reservoir conditions for high-permeability carbonate rocks: Society of Petroleum Engineers, SPE 134028-MS.
- Benson, S., 2005, Overview of geologic storage of CO₂, in carbon dioxide capture for storage in deep geologic formations, Volume 2—Results from the CO₂ capture project: Elsevier Publishing, UK.
- Bidgoli et al, 2017
- Burnside, N. M., and Naylor, M., 2014, Review and implications of relative permeability of CO₂/brine systems and residual trapping of CO₂: *Int. J. Greenh. Gas Control*, 23, p. 1–11
- Bui, L. H., Tsau, J. S., and Willhite, G. P., 2010, Laboratory investigations of CO₂ near-miscible application in Arbuckle Reservoir: SPE Improved Oil Recovery Symposium, Tulsa, Oklahoma, 24–28 April 2010, SPE Publication 129710.
- Bradley, J. S. (1975). Abnormal formation pressure. *AAPG Bulletin*, 59(6), 957-973.
- Crabtree, B., Christensen, J., (2012). CO₂-EOR Potential in the MGA Region, Great Plains Institute for Sustainable Development Report
- Carter, R. D., and Tracy, G. W., 1960, An improved method for calculating water influx: *Petroleum Transactions, AIME*, v. 219, p. 415–417.
- Chang, K. W., Minkoff, S. E., and Bryant, S. L., 2009, Simplified model for CO₂ leakage and its attenuation due to geological structures: *Energy Procedia*, v. 1, p. 3,453–3460.
- Crampin, S., 1999, Calculable fluid-rock interactions. *Geological Society, London*. **156**. 501-514.
- Crampin, S., S. Peacock, Y. Gao, S. Chastin, 2004, The Scatter of time-delays in shear-wave splitting above small earthquakes. *Geophysics Journal International*. **156**. 39-44.
- Dake, L. P., 1978, *Fundamentals of Reservoir Engineering*, Chapter 9, Elsevier Scientific Publishing Co., 1978.
- Ellsworth, W.L., 2013, Injection-Induced Earthquakes. *Science*. **341**. 1225942
- Fadolalkarem, Y., 2015, Pre-Stack Seismic Attribute Analysis of the Mississippian Chert and the Arbuckle Group at the Wellington Field, south-central Kansas. University of Kansas master's thesis.

FazelAlavi, M., FazelAlavi, M., and FazelAlavi, M., 2013, Wellington Field, Mississippian Formation.

Franseen, E.K., Byrnes, A.P., Cansler, J. R., Steinhaff, D.M., Carr, T.R., and Dubois, M.K., 2003, Geologic Controls on Variable Character of Arbuckle Reservoirs in Kansas: An Emerging Picture: Kansas Geological Survey Open-file Report 2003-59, 30 p.

Franseen et al 2004

FutureGen Industrial Alliance, 2013, Underground injection control permit applications for FutureGen 2.0 Morgan County Class VI UIC Wells 1, 2, 3, and 4, Jacksonville, Illinois.

Goebel, E. D. (1968). Mississippian rocks of western Kansas. AAPG Bulletin, 52(9), 1732-1778.

Gray, D., Anderson, P., Logel, J., Delbecq, F., Schmidt, D., Schmid, R., 2012, Estimation of stress and geomechanical properties using 3D seismic data: First Break, v. 30, p. 59-68.

Graham, B. L., Haga, L. N., Nolte, K. A., Tsoflias, G. P., and W. L. Watney (2017), Fracture Mapping and Feasibility of Monitoring CO₂ in situ From Seismic Data at the Mississippian Carbonate Reservoir, Wellington Oil Field, South-Central Kansas, in DOE NETL Mastering the Subsurface Through Technology Innovation, Partnerships and Collaboration: Carbon Storage and Oil and Natural Gas Technologies Review Meeting, Pittsburgh, PA, August 1-3, 2017.

Hampson, D., Russell, B., and Bankhead, B., 2005, Simultaneous inversion of pre-stack seismic data: Ann. Mtg. Abstracts, Society of Exploration Geophysicists.

Hawkins, K., Leggott, R., Williams, G., Kat, H., 2001, Addressing Anisotropy in 3-D prestack depth migration: A case study from the Southern North Sea: The Leading Edge, May, p528-535.

J. Havskov, L. Ottemoller, 1999, SeisAn Earthquake analysis software, *Seismological Research Letters*, **70**.

Holubnyak, Y., Watney, L., Rush, J., Bidgoli, T., Williams, E., and Gerlach, P., 2016, Calculation of CO₂ storage capacity for Arbuckle Group in southern Kansas: Implications for a seismically active region: 13th International Conference on Greenhouse Gas Control Technologies, Lausanne, Switzerland

Holubnyak Y., Watney W., Rush J., Fazelalavi M., 2016, Reservoir evaluation and modeling of pilot scale CO₂ EOR project in Mississippian Lime at Wellington Field in Southern Kansas, Energy Procedia 63, 7732-7739

Holubnyak, Y., Watney, W., Birdie, T., Rush, J., Fazelalavi, M., Wreath, D., (2017). Pilot Scale CO₂ EOR in Mississippian Carbonate Reservoir at Wellington Field in South-Central Kansas, Energy Procedia, EGYPRO30710.

Jorgensen et al 1993

KGS oil and gas wells database, Kansas Geological Survey, <http://www.kgs.ku.edu/Magellan/Qualified/>, (accessed 12/1/2017).

Keranen, M. Weingarten, G.A. Abers, B.A. Bekins, S. Ge, 2014, Sharp increase in central Oklahoma seismicity since 2008 induced by massive wastewater injection. *Science*. **345**. 448-451

Kestin, J., Khalifa, H. E., and Correia, R. J., 1981, Tables of the dynamic and kinematic viscosity of aqueous NaCl solutions in the temperature range 20–150 °C and the pressure range 0.1–35 MPa: Journal of Physical and Chemical Reference Data, NIST, v. 10, p. 71–88.

Krevor, P., and Benson, S. M., 2012, Capillary pressure and heterogeneity for the CO₂/water system in sandstone rocks at reservoir conditions: *Advances in Water Resources*, v. 38, p. 48–59, ISSN: 0309-1708

Krevor, P., and Benson, S. M., 2015, Accurate determination of characteristic relative permeability curves: *Advances in Water Resources*, v. 83, p. 376–388

Li, Y. K., and Nghiem, L. X., 1986, Phase equilibrium of oil, gas and water/brine mixtures from a cubic equation of state and Henry's Law: *Canadian Journal of Chemical Engineering*, June, p. 486–496.

Lugn, A. L. (1935). The Pleistocene Geology of Nebraska: Nebraska Geol. Survey, Bull. 10, pp. 1-223.

Lee, W., and Merriam, D. F. (1954). Preliminary Study of the Structure of Western Kansas. State Geological Survey of Kansas, University of Kansas.

Loucks, R. G., 1999, Paleocave carbonate reservoirs: Origins, burial-depth modifications, spatial complexity, and reservoir implications: *The American Association of Petroleum Geologists, Bulletin*, v. 83, no. 11.

Lucia, F. J., 1999, Carbonate reservoir characterization: New York, Springer-Verlag, 226 p.

Lynn, H., 2016, Applied Azimuthal Anisotropy: Geophysical Society of Houston Webinar series. Reservoir: implications for assessing candidates for CO₂ sequestration, *in* M. Grobe, J. C. Pashin, and R. L. Dodge, eds., Carbon dioxide sequestration in geological media—State of the science: AAPG Studies in Geology 59, p. 297–319.

Mazzullo, S. J., B. W. Wilhite, and I. W. Woolsey, 2009, Petroleum reservoirs within a spiculite-dominated depositional sequence: Cowley Formation (Mississippian: Lower Carboniferous), south-central Kansas: *AAPG Bulletin*, v. 93, no.12, p.1649-1689.

McIntosh 2004

Misaghi, A., S. Landro, and A. Javaherian, 2010, A comparison of rock physics models for fluid substitution in carbonate rocks: *Exploration Geophysics*, v. 41, p. 146-154.

Montgomery, S. L., 1998, Thirtyone formation, Permian Basin, Texas: structural and lithologic heterogeneity in a lower Devonian chert reservoir: *AAPG Bulletin*, v. 82, no. 1, p. 1-24.

Nelson, P. H., and Gianoutsos, N. J. (2011). Evolution of overpressured and underpressured oil and gas reservoirs, Anadarko Basin of Oklahoma, Texas, and Kansas (No. 2011-1245). US Geological Survey.

Newell, K. D., Watney, W. L., Cheng, W. L., and Brownrigg, R. L. (1987). Stratigraphic and spatial distribution of oil and gas production in Kansas.

Nissen, S. E., T. R. Carr, K. J. Marfurt, and E. C. Sullivan, 2009, Using 3-D seismic volumetric curvature attributes to identify fracture trends in a depleted Mississippian carbonate reservoir: implications for assessing candidates for CO₂ sequestration, *in* M. Grobe, J. C. Pashin, and R. L. Dodge, eds., Carbon dioxide sequestration in geological media—State of the science: AAPG Studies in Geology 59, p. 297–319.

Nolte et al 2017

Pau, G. S. H., Bell, J. B., Pruess, K., Almgren, A. S., Lijewski, M. J., and Zhang, K., 2010, High resolution simulation and characterization of density-driven flow in CO₂ storage in saline aquifers: Advances in Water Resources, v. 33, no. 4, p. 443–455.

Rogers, J. P., and M. W. Longman, 2001, An introduction to chert reservoirs of North America, 2001, AAPG Bulletin, v. 85, no.1, p. 1-5.

Ruger, A., 1998, Variation of P-wave reflectivity with offset and azimuth in anisotropic media: Geophysics, v. 63, no. 3, p 935-947.

Rubinstein, A.B. Mahani, 2015, Myths and Facts on Wastewater Injection, Hydraulic Fracturing, Enhanced Oil Recovery, and Induced Seismicity. *Seismological Research Letters*. **86**. 1060-1067.

Scheffer, A. (2012). Geochemical and Microbiological Characterization of the Arbuckle Saline Aquifer, a Potential CO₂ Storage Reservoir; Implications for Hydraulic Separation and Caprock Integrity (Doctoral dissertation, University of Kansas).

Schwab, D.R., Bidgoli, T.S., Taylor, M. H., (2017) Characterizing the potential for injection-induced fault reactivation through subsurface structural mapping and stress field analysis, Wellington Field, Sumner County, Journal of Geophysical Research: Solid Earth

Schwab, A., 2016, Characterizing the potential for fault reactivation related to fluid injection through subsurface structural mapping and stress field analysis, Wellington Field, Sumner County, KS: M.S. thesis, University of Kansas.

Sirazhiev, A., 2012, Seismic Attribute Analysis of the Mississippian Chert at the Wellington Field, south-central Kansas. University of Kansas master's thesis.

Sørenseide, I., and Whitson, C. H., 1992, Peng-Robinson predictions for hydrocarbons, CO₂, N₂, and H₂S with pure water and NaCl brine: Fluid Phase Equilibria, v. 77, p. 217–240.

Sorenson, R. P. (2005). A dynamic model for the Permian Panhandle and Hugoton fields, western Anadarko basin. AAPG bulletin, 89(7), 921-938.

Thomsen, L., 2002, Understanding seismic anisotropy in exploration and exploitation: SEG/EAGE Distinguished instructor short course and text

Kansas Corporation Commission (KCC), KGS #2-32 Class II Well Design Approval, July, 2014

Vega, S., K. Berteussen, Y. F. Sun, and A. A. Sultan, 2007, Is Gassmann the best model for fluid substitution in heterogeneous carbonates: 77th Annual International Meeting, SEG, Expanded Abstract, p.1575-1578

Walsh, M.D. Zoback, 2015 Oklahoma's recent earthquakes and saltwater disposal. *Science Advances*. **1**. e1500195

Watney et al. Preliminary Reservoir Description (Permeability, Capillary Pressure, and Relative Permeability), Kansas Geological Survey Open File Report, 2015-26

Watney et al. Reservoir Modeling of CO₂ Injection in Arbuckle Saline Aquifer at Wellington Field, Sumner County, Kansas, Kansas Geological Survey Open File Report 2016-29

Watney, W. L., W. J. Guy, and A. P. Byrnes, 2001, Characterization of the Mississippian chat in south-central Kansas: AAPG Bulletin, v. 85, no.1, p. 85-113.

Watney, W. L., Guy, W. J., and Byrnes, A. P. (2002). Characterization of the Mississippian Osage chat in south-central Kansas: Kansas Geological Survey, Open-File Report 2002-50.

Whittemore 1995

Yeck, M. Weingarten, H.M. Benz, D.E. McNamara, E.A. Bergman, R.B. Herrman, J.L. Rubinstein, P.S. Earle, 2016, Far-field pressurization likely caused one of the largest injection induced earthquakes by reactivating a large preexisting basement fault structure. *Geophysical Research Letters*. **43**.

Zeller, D. E. (1968). Stratigraphic succession in Kansas. Kansas Geological Survey Bulletin, 189. <http://www.kgs.ku.edu/Publications/Bulletins/189/> (accessed 12/12/2017)

Zinke, M.D. Zoback, 2000, Structure-related and stress-induced shear-wave velocity anisotropy: observations from microearthquakes near the Calaveras fault in central California. *Bulletin of the Seismological Society of America*. **90**. 1305-1312